Laboratory Investigations of Magnetic Field Generation and Interactions Driven by High Power Lasers

by

Paul T. Campbell

A dissertation submitted in partial fulfillment
of the requirements for the degree of
Doctor of Philosophy
(Applied Physics)
at the University of Michigan
2019

Doctoral Committee:

Professor Karl Krushelnick, Co-Chair
Assistant Professor Louise Willingale, Co-Chair
Dr. Gennady Fiksel
Associate Professor Carolyn Kuranz
Dr. Anatoly Maksimchuk
Associate Professor Alexander G. R. Thomas

Paul T. Campbell

campbpt@umich.edu

ORCID iD: 0000-0002-7192-0221

Dedicated to Maude, John, Charles, and Henria

ACKNOWLEDGMENTS

This thesis work would not have been possible without the strong support from my committee and from the faculty, staff and fellow students in the High Field Sciences group. I especially thank my advisors Prof. Louise Willingale and Prof. Karl Krushelnick for guiding my growth as a scientist, giving me the opportunity to lead experiments at the OMEGA EP facility, and encouraging me to share my work at conferences around the world. Thank you Anatoly Maksimchuk for training me in the lab and showing me how to think critically about experiments, Gennady Fiksel for many helpful discussions of magnetic reconnection and proton radiography, Prof. Alec Thomas for help with simulations and physics discussions. I am grateful to my fellow graduate students, especially Peter Kordell for introducing me to the group and for being a great friend throughout, Anthony Raymond, Thomas Batson and Amina Hussein for support during OMEGA EP experiments and fun trips to Rochester, Jinpu Lin for being a genial officemate, and Brandon Russell for good discussions of magnetic fields and reconnection.

Many other colleagues and collaborators helped me throughout my thesis work. I want to thank the OMEGA EP staff at the Laboratory for Laser Energetics, Sarah Mueller of General Atomics for assembling the targets, David Carroll of the Rutherford Appleton Laboratory for helpful communication regarding radiochromic film, Michael Pillainayagam and Dr. Dale Litzenberg of the Radiation Oncology department of Michigan Medicine for their assistance calibrating radiochromic film, and Chris Ridgers for useful discussions of magnetic field generation. I especially thank Charlotte Palmer for her guidance and helpful advice at many stages during the experimental analysis. I would also like to acknowledge the OSIRIS Consortium, consisting of UCLA and IST (Lisbon, Portugal) for providing access to the

OSIRIS 4.0 framework. Work supported by NSF ACI-1339893. The material presented in this thesis is based upon work supported by the Department of Energy/NNSA under Award Numbers DE-NA0002372 and DE-NA0002727.

Finally, I am very fortunate to have an incredibly supportive network of family and friends. My family, Charles, Mary, Grace, Jackson and Sorie, as well as my wife's family, Mark, Caroline, and Ginny, have been a constant source of encouragement. Most especially, thank you Sarah for being an amazing partner and for your constant support, wisdom and love. Words truly cannot express the depth of my gratitude.

TABLE OF CONTENTS

LIST OF FIGURES

LIST OF TABLES

LIST OF APPENDICES

ABSTRACT

This thesis describes experimental and computational efforts to develop diagnostic tools, investigate magnetic field generation, and probe the dynamics of magnetic fields driven by high power lasers.

Proton beams accelerated via the target normal sheath acceleration (TNSA) mechanism can be used to diagnose electric and magnetic fields present in high power laser-produced plasmas. In experiments using the OMEGA EP laser system, measurements were made of proton beams generated by up to 100 ps, kilojoule-class laser pulses having relativistic intensities. By systematically varying the laser pulse duration, degradation of the accelerated proton beam quality was measured as the pulse length increased. Two dimensional particle-in-cell (PIC) simulations and simple scaling arguments suggest that ion motion during the rise time of the longer pulses leads to extended preformed plasma expansion from the rear target surface and strong filamentary field structures which can deflect ions away from uniform trajectories, leading to large emittance growth. Optimal laser pulse conditions for proton radiography applications were identified.

Proton radiography was used to explore both moderate ($I_L = 2 \times 10^{14}$ Wcm^{-2}) and high ($I_L > 10^{19}$ Wcm^{-2}) intensity lasers interacting with foil targets. The strength, spatial profile, and dynamics of self-generated magnetic fields were measured as the target material was varied between plastic (CH), aluminum and copper. In the case of moderate intensity pulses, radiation-driven double ablation fronts in higher Z targets initiate multiple regions of Biermann battery ($\nabla T_e \times \nabla n_e$) magnetic field generation. Results were compared to

extended magnetohydrodynamics (MHD) simulations with radiation transport which reproduced key aspects of the experiment. At high intensities, rapid expansion of the magnetic fields was observed, as well as enhanced filamentation in lower Z, insulator targets. 2D PIC simulations were used to probe the underlying physics of high intensity laser-driven magnetic field generation, including the impact of preformed plasma scale length.

Finally, each of these elements were brought together to study a highly asymmetric laser-driven reconnection geometry established by focusing a high intensity pulse alongside a moderate intensity long pulse. After the long pulse plasma and associated magnetic field has evolved, the high intensity pulse arrives on target producing a relativistic, highly magnetized plasma. Proton radiography captures the dynamic interaction of the strong, impulsive magnetic field generated by the high intensity pulse and the relatively slowly evolving Biermann battery fields. Quantitative measurements of the magnetic field dynamics and 3D particle-in-cell simulation results show signatures of a magnetized interaction potentially indicative of shock formation and asymmetric magnetic reconnection.

CHAPTER 1

Introduction

Modern laser technology can create high energy density (HED) conditions in the laboratory [5]. At these extreme temperatures and pressures, electrons can be stripped from the atoms, producing a plasma. Much of the known universe is in the plasma state, and the HED conditions accessed by laser-produced plasmas enable laboratory-based experiments to probe fundamental astrophysical processes [6].

Strong magnetic fields of order 1 to 100 Mega-Gauss (MG) (100 to 10,000 Tesla) can be spontaneously generated within laser-produced plasmas [7–10]. Despite the strong fields, these HED plasmas are typically thermally dominated (i.e., the ratio of thermal pressure to magnetic pressure exceeds unity, $\beta = n_e k_B T_e/(B^2/2\mu_0) \gg 1$). As a result, magnetic fields were largely neglected during the initial development of HED theory and modeling [11]. However, improved experimental measurements and computational tools have demonstrated that generation and evolution of such magnetic fields can have important consequences for energy transport in HED systems [12–16]. Because charged plasma particles gyrate around field lines, magnetic fields can act to guide or confine the plasma.

One of the principal applications of laser-driven HED plasmas is inertial confinement fusion (ICF) [17]. High power lasers are used drive the implosion and compression of fuel to fusion conditions either through direct illumination [18] or indirectly by producing a thermal x-ray bath within a hohlraum (typically a high-Z metal cylinder) [19]. Application of an external magnetic field may improve fusion performance by suppressing electron heat

conduction during the implosion [20]. Self-generated magnetic fields have been shown to impact energy flow in the hohlraum [21, 22] and strong fields generated during the implosion can influence hydrodynamic instabilities [23] and the heat flow within the fusion fuel [24].

In addition to impacting the dynamics and energy transport of ICF-relevant plasmas, strong laser-driven magnetic fields facilitate exploration of magnetized astrophysical phenomena, such as magnetic reconnection [25], in an HED setting. Across the broad scope of HED research, there is a need to improve the characterization and understanding of magnetic field generation and dynamics. With this motivation, experimental and computational efforts presented in this thesis are dedicated to developing diagnostic capabilities, examining the physics of laser-driven magnetic field generation, and probing dynamic magnetized interactions.

Magnetic Reconnection

Magnetic reconnection is a plasma process by which magnetic field energy is converted to plasma energy through changes in the field topology (see reviews by Zwiebel *et al.* [26] and Yamada *et al.* [27], and references therein). As opposing magnetic fields are driven together by flowing plasmas, the field lines will break and reconfigure into a lower energy state. Excess energy is converted to plasma thermal or kinetic energy. While reconnection is expected to power a number of astrophysical phenomena - such as solar flares, coronal mass ejections, or gamma ray bursts - the underlying mechanisms governing changes to the magnetic field topology and energy transfer are poorly understood.

The nearest example of reconnection in a natural setting is observed in the interaction of Earth's magnetosphere with the solar wind. An illustration of this interaction is shown in Figure 1.1. As the solar wind moves toward Earth, it carries along magnetic fields from the Sun. A bow shock forms as the wind slows and is diverted around the magnetosphere. The magnetopause marks the boundary between solar and terrestrial fields. While forbidden under idealized assumptions, magnetic reconnection at the day-side allows the solar wind to

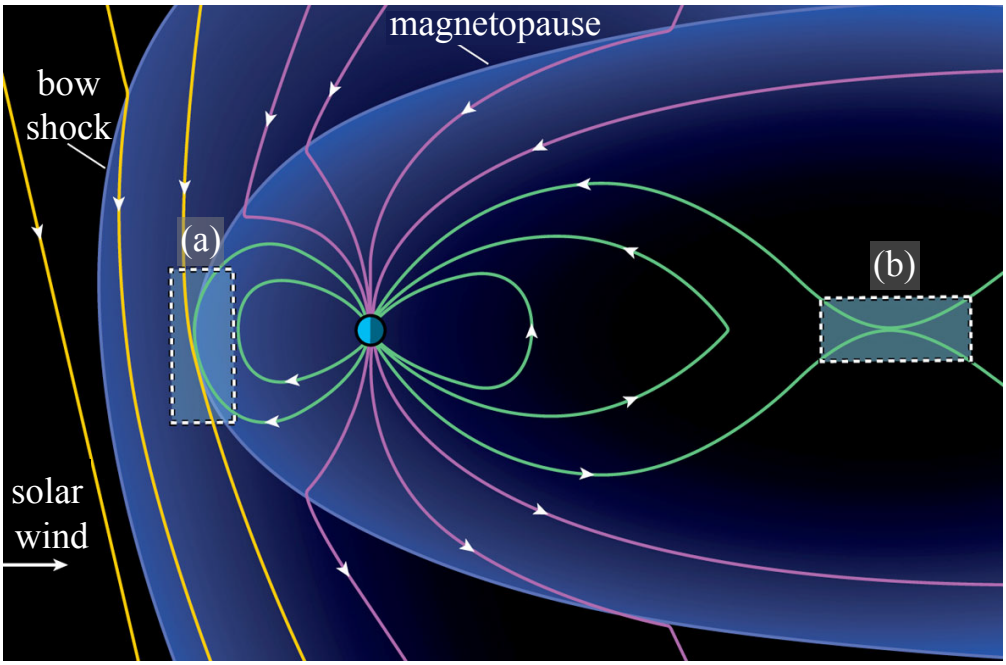

Figure 1.1: An illustration of the solar wind and the Earth's magnetosphere adapted from [1] in accordance with the Creative Commons license [2]. The solar wind carries solar magnetic field lines (yellow). A bow shock forms as the wind encounters Earth's magnetosphere. Rectangular regions indicate where reconnection is often observed at the day-side magnetopause (a), and in the magnetotail (b). Closed field lines of the magnetophsere are shown in green, while reconnected "open" field lines are shown in pink.

penetrate the magnetosphere. In addition, the Earth's magnetic field lines are swept back to the night-side, where reconnection can also occur in the elongated magnetotail. Particles energized by reconnection can drive geomagnetic storms and potentially damage satellites and other Earth-based technology, or cause a large scale power blackout.

Magnetic reconnection is also thought to play an important role in extremely energetic astrophysical phenomena such as gamma ray bursts (GRBs), relativistic pulsar wind emissions and jets from active galactic nuclei [28–30]. In such systems, the magnetic fields can be so strong that the energy density of the field exceeds the relativistic mass-energy density of the plasma (i.e., $\sigma = B^2/\mu_0 n_e m_e c^2 > 1$). As a result, reconnection can drive relativistic outflows and extreme particle acceleration, potentially explaining the origin of high energy cosmic rays observed throughout the universe [31].

Laser-driven magnetic reconnection

Laboratory-based experiments can help illuminate the fundamental physics of reconnection [27]. Laser-driven, HED reconnection complements the work of more traditional experiments based on magnetic discharges, such as the magnetic reconnection experiment (MRX) at Princeton Plasma Physics Laboratory [32], by facilitating exploration two-fluid effects, magnetic island formation, and particle acceleration in strongly driven reconnection [33]. A schematic of the typical laser-driven reconnection geometry is shown in Figure 1.2. Two high power laser pulses are focused side-by-side on solid targets. Opposing self-generated magnetic fields are forced together by the expanding plasmas, driving reconnection.

Numerous experiments and simulations have examined magnetic reconnection driven by high power laser pulses with nanosecond durations [25, 33–42]. When focused to moderate intensities ($I_L \approx 10^{14}$ Wcm^{-2}), nanosecond laser pulses ablate the surface of solid targets. Misaligned temperature and density gradients in the plasma plume generate a strong azimuthal magnetic fields (∼1 MG) due to the Biermann battery effect ($\frac{dB}{dt} \propto \nabla T_e \times \nabla n_e$). Compared to traditional experiments, the high temperature of laser-driven plasmas enables exploration of strongly driven reconnection with super-Alfvénic inflows [33]. Due to relatively high densities, the laser-driven system sizes can be much larger than critical length scales, such as the ion skin depth ($d_i = c/\omega_{pi}$). In addition, the experimental geometry permits instantaneous measurements of the global magnetic field topology through proton imaging, as well as characterization of energized particles far from the reconnection region [43].

Recent experiments have extended laser-driven magnetic reconnection to high intensities ($I_L \sim 10^{18}$ to 10^{19} Wcm^{-2}) [44,45]. At these intensities, the electric field of the laser pulse can accelerate electrons to relativistic velocities. Rapid expansion of relativistic electrons along the target surface establishes a strong target-normal sheath electric field and generates an azimuthal magnetic field surrounding the focal spot. In contrast to the nanosecond pulse experiments described above, the magnetic fields generated by high intensity pulses are orders of magnitude stronger ($\mathcal{O}100MG$) and driven together at velocities near the speed

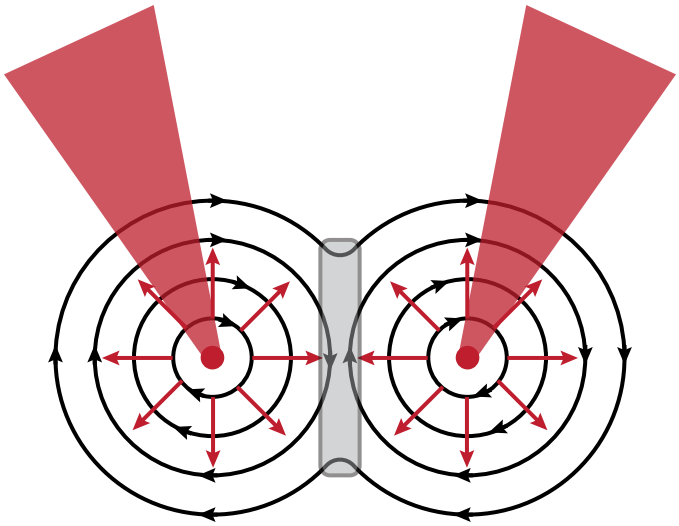

Figure 1.2: Sketch of the laser-driven magnetic reconnection geometry. Two laser pulses are focused side-by-side. Self-generated magnetic fields (black) are driven together by expanding plasmas (red arrows). A reconnection region is established in the midplane (gray).

of light [9, 44]. The magnetic fields are so strong that these high intensity experiments approached the relativistic magnetic reconnection regime relevant to extremely energetic astrophysical phenomena. Additionally, the mean-free-path between particle collisions is expected to be larger than the system size, so reconnection driven by high intensity laser pulses can potentially test reconnection theory in the collisionless regime.

Laser-driven HED reconnection can make important contributions to the broad suite of laboratory experiments, simulations and satellite missions dedicated to deepening our understanding of this fundamental plasma process. However, the mirco-physics of the reconnection region is strongly linked to initial conditions of the global system. Despite first measurements of self-generated fields dating back decades [7,46], improved experimental and computational tools continue to shed new light on the rich physics governing field generation and transport across both intensity regimes [8, 9, 47]. To advance HED reconnection, it is important to develop a more complete understanding of magnetic field generation and evolution driven by high power lasers.

Proton imaging

Experiments described in this thesis are devoted to time-resolved measurements of the generation, evolution and interactions of magnetic fields driven by high power lasers. These large amplitude, self-generated magnetic fields typically form in a relatively thin layer near the surface of the foil targets, and the peak field strengths are located in regions of relatively high plasma density. This makes optical techniques for magnetic field measurement challenging. Instead, charged particle imaging (also known as deflectometry or radiography) is often the preferred technique for diagnosis of electric and magnetic fields in the HED plasmas.

The fundamental approach for charged particle imaging in HED experiments is to use a secondary laser pulse to accelerate a beam of particles, typically protons or electrons [9,48,49]. As the beam passes through the principal interaction, the particle trajectories will be altered by the electric and magnetic fields present in the plasma. These deflections are recorded by stacks of film or scintillating screens.

When focused to high intensities ($I_L > 10^{18}$ Wcm^{-2}) on solid foil targets, high power lasers can drive a burst of high energy ions [50–52] accelerated via the target normal sheath acceleration (TNSA) mechanism [53]. To date, TNSA is most studied, robust, and best characterized laser-driven ion acceleration mechanism. With modern laser technology, ions are too massive to be directly accelerated by the laser field. Instead, the laser pulse excites fast electrons which establish strong, quasi-static accelerating field structures along the target surface. As a result, the TNSA mechanism can accelerate protons and other ions to energies approaching 100 MeV per nucleon [54].

These laser-driven ion beams exhibit a number of properties that make them an excellent source for charged particle imaging. The acceleration time is short (typically ranging from 100s of fs to 10s of ps), enabling high temporal resolution measurements. Nearly laminar propagation [55,56] and a small, virtual source size [57] lead to very high spatial resolutions, especially compared to D^{3}He fusion [58,59], an alternate HED proton imaging source.

Another feature of protons beams accelerated via the TNSA mechanism is a broad,

quasi-Maxwellian energy spectrum. During transit between the proton source and the main interaction, the initially short burst of protons will be stretched in time, with faster protons arriving earlier than slower protons. Each proton energy will effectively sample a different time in the main interaction evolution. As a result, the broad spectrum makes possible single shot, time-resolved measurements of ultrafast electromagnetic field dynamics with picosecond temporal resolution (as shown in references [10] and [60]).

In addition to measurements presented in this thesis, TNSA protons beams have been instrumental in measuring a number of HED electromagnetic phenomena including magnetic field generation [8, 10], magnetic self-organization [61, 62], high power laser channeling [60], and laboratory magnetic reconnection [25, 36, 63].

Thesis Outline

The work presented in this thesis investigates the physics of laser-driven proton acceleration, magnetic field generation, and magnetized interactions. As described above, proton beams accelerated via the TNSA mechanism are an important tool for diagnosing electromagnetic fields in HED plasmas. Recent simulations and experiments have revisited the physics of TNSA in the context of kilojoule-class laser systems and have observed enhanced proton energies using high intensity laser pulses with multipicosecond durations [64–68]. However, the work presented here in Chapter 4 demonstrates significant degradation of proton beam quality as the pulse duration is increased. For imaging applications, any potential gains in maximum proton energy afforded by using multipicosecond laser pulses could be outweighed by degraded beam quality. In addition to discussion of the physical mechanisms impacting beam quality, the results are used to identify optimal conditions for proton imaging experiments.

Next, the optimized proton source is used to measure the influence of target material on magnetic field generation driven by both moderate and high intensity lasers. For moderate intensities, previous high resolution imaging of the magnetic fields has generally been limited

to low-Z, plastic targets [8]. However, experiments and simulations presented in Chapter 5 demonstrate that radiation effects in higher-Z plasmas can impact the magnetic field evolution. The influence of radiation on field generation can have important consequences for a number of HED experiments, especially within high-Z hohlraums used for indirect drive ICF research.

For high intensity pulses, the proton imaging captures enhanced filamentary field formation for lower-Z, insulating targets. While previous experiments have used shorter, lower energy pulses [9,10,69], the results presented here are some of the first direct observations of magnetic field generation driven by multipicosecond, kilojoule-class laser pulses. In addition to guiding design and interpretation of high intensity laser-driven magnetic reconnection experiments, these measurements illuminate the temporal evolution of magnetic and electric fields relevant to ion acceleration.

Finally, the TNSA proton source is used to image the dynamics of a highly asymmetric laser-driven reconnection geometry. As seen with the interaction of the solar wind with Earth's magnetosphere (Figure 1.1), magnetic reconnection is typically asymmetric in astrophysical systems. A highly asymmetric magnetic interaction can be produced in the laboratory by focusing a high intensity pulse in close proximity to an evolving moderate intensity laser-produced plasma. The proton imaging captures the evolution of the global system, as well as the details of the magnetic field interaction dynamics.

Each chapter in this thesis is centered around developing and interpreting experiments performed at the OMEGA EP laser system at the Laboratory for Laser Energetics of the University of Rochester. After introducing relevant theoretical background and experimental methods, subsequent chapters will progressively build up understanding of laser-driven proton acceleration for imaging applications, magnetic field generation and dynamic field interactions. The thesis is structured as follows:

- **Chapter 2**: Relevant theoretical background is reviewed, with an emphasis on high power laser-solid interactions, magnetic field generation, and reconnection.

- **Chapter 3**: Key methods used throughout the thesis work are detailed, including a description of the OMEGA EP laser system, proton detection, spectrum reconstruction and image analysis methods.

- **Chapter 4**: Experiments to develop and characterize a laser-driven proton source on OMEGA EP are presented, and optimal laser conditions are identified. Particle-in-cell simulations help illustrate beam quality degradation for longer laser pulse durations. Work presented in this chapter has been accepted for publication in *New Journal of Physics* [70].

- **Chapter 5**: The high energy proton source developed in Chapter 4 is used to diagnose magnetic field generation driven by either high or moderate intensity laser pulses. Double ablation front formation is observed in the proton images and extended-magnetohydrodynamics simulations of moderate intensity interactions as the target Z is increased. At high intensity, enhanced filamentation is observed in low-Z, insulator targets and particle-in-cell simulations illuminate the physics of magnetic field generation and the effect of target pre-expansion.

- **Chapter 6**: Elements from Chapters 4 and 5 are brought together. The proton source is used to image a highly asymmetric magnetic interaction driven by high and moderate intensity pulses focused side-by-side in a reconnection geometry. A dynamic magnetic interaction is observed in both the proton images and simplified 3D particle-in-cell modeling.

- **Chapter 7**: The thesis conclusions are summarized and potential future work is discussed.

The majority of the experimental design and analysis presented here was carried out by the author, in addition to all of the particle-in-cell simulations. A number of collaborators made invaluable contributions to the work. The initial conception and development of the

2D proton image inversion code presented in Chapter 3 was led by Professor Alexander G. R. Thomas. Further implementation and testing was performed by the author. The 1D polar coordinates inversion approach developed by the author was inspired by a 1D Cartesian method created by Dr. Gennady Fiksel. Calibration of radiochromic film described in Chapter 3 was performed in collaboration with Michael Pillainayagam and Dr. Dale Litzenberg in the department of Radiation Oncology at Michigan Medicine. The author was aided in film scanning by Krishen Ratnayaka. Extended magneto-hydrodynamics simulations presented in Chapter 5 were performed by Dr. Christopher Walsh of Imperial College London. Proton scattering analysis used in Chapter 6 and shown in Appendix D was carried out by Dr. Charlotte Palmer of the University of Oxford.

CHAPTER 2

Theoretical Background

In this chapter, the fundamental theory of laser-plasma interactions will be reviewed, with a particular emphasis on laser-solid interactions. Unless otherwise stated, the primary references for this chapter are the excellent textbooks by William Kruer [71], Paul Gibbon [72], and R. Paul Drake [5], as well as the PhD thesis by Louise Willingale [73]. In addition, the physics of laser-driven magnetic field generation and magnetic reconnection are introduced. More complete discussions can be found in Chapters 5 and 6, and recent reviews on reconnection by Yamada *et al.* [27] and Zweibel *et al.* [26].

2.1 Laser plasma interactions

2.1.1 Interaction with a single electron

To gain insight into the underlying physics of laser-plasma interactions, it is instructive to begin with the interaction of a plane wave with a single electron. The laser wave propagates in the $\hat{z}$ and is described by the vector potential,

$$\vec{A}(z,t) = A_0 \sin(k_L z - \omega_L t)\hat{x} \tag{2.1}$$

where $k_L = 2\pi/\lambda_L$ is the wave vector and $\omega_L = 2\pi c/\lambda_L$ is the frequency for a laser with wavelength λ_L. The electric and magnetic fields can be derived from the vector potential in

the as

$$\vec{E} = -\frac{\partial \vec{A}}{\partial t} = \omega_L A_0 \cos(k_L z - \omega_L t)\hat{x} \tag{2.2}$$

$$\vec{B} = \nabla \times \vec{A} = k_L A_0 \cos(k_L z - \omega_L t)\hat{y}. \tag{2.3}$$

The force experienced by an electron is described by the Lorentz force,

$$\frac{\mathrm{d}\vec{p}}{\mathrm{d}t} = -e(\vec{E} + \vec{v} \times \vec{B}) \tag{2.4}$$

where $p = \gamma m_e v$ with $\gamma = (1 - (v/c)^2)^{-1/2} = \sqrt{1 + (p/m_e c)^2}$. Substituting equations (2.2) and (2.3) into (2.4), and using the vector identity $\vec{v} \times (\nabla \times \vec{A}) = \nabla(\vec{v} \cdot \vec{A}) - (\vec{v} \cdot \nabla)\vec{A}$, an equation of motion for the electron can be expressed in terms of the laser vector potential,

$$\frac{\mathrm{d}\vec{p}}{\mathrm{d}t} = -e\bigg(- \frac{\mathrm{d}\vec{A}}{\mathrm{d}t} + \nabla(\vec{v} \cdot \vec{A})\bigg), \tag{2.5}$$

where the total derivative is defined $\frac{\mathrm{d}}{\mathrm{d}t} = \frac{\partial}{\partial t} + (\vec{v} \cdot \nabla)$.

First, considering the $\hat{x}$ direction and noting that $\partial A/\partial x = 0$, the equation of motion can be integrated to solve for p_x. Normalizing by $m_e c$,

$$\frac{p_x}{m_e c} = \frac{eA}{m_e c} = a \tag{2.6}$$

where $a = \frac{eE}{\omega_L m_e c}$ is the normalized vector potential.

In the $\hat{z}$ direction, the energy-momentum relation

$$\gamma^2 = \big(\frac{p_x}{m_e c}\big)^2 + \big(\frac{p_z}{m_e c}\big)^2 + 1 \tag{2.7}$$

and work equation,

$$m_e c^2 \frac{\mathrm{d}\gamma}{\mathrm{d}t} = -e\vec{v} \cdot \vec{E} \tag{2.8}$$

can be combined with the equation of motion to give

$$\frac{p_z}{m_e c} = \frac{1}{2}(\frac{p_x}{m_e c})^2 = \frac{1}{2}a^2. \tag{2.9}$$

From equations (2.6) and (2.9), the electron motion is governed by the normalized vector potential, a. When $a > 1$, the quiver motion of the electron becomes relativistic. Using $I_L = \frac{\epsilon_0 c}{2}E^2$, the peak intensity threshold for relativistic interactions can be derived,

$$a_0 = \sqrt{\frac{I_0 \lambda_{\mu\mathrm{m}}^2}{1.387 \times 10^{18}\ (\mathrm{Wcm}^{-2}\mu\mathrm{m}^2)}} > 1 \tag{2.10}$$

where I_0 is the peak intensity in units of Wcm^{-2} and $\lambda_{\mu\mathrm{m}}$ is the laser wavelength in microns.

2.1.2 Ponderomotive force

While an infinite plane wave was used in section 2.1.1, experiments typically use short pulses focused to small spots, resulting in strong transverse and longitudinal gradients in the field strength. During the interaction, electrons can move into a weaker field region where the restoring force will be insufficient to complete the quiver motion. On average, over subsequent laser cycles, electrons will drift toward weaker fields and will eventually be completely expelled from the high field region. This push due to spatial gradients in the field strength is known as the ponderomotive force.

Combing equations (2.5) and (2.6) and taking the time average over the fast oscillation cycle yields an expression for the ponderomotive force of the laser,

$$F_P = \frac{-e^2}{2\langle\gamma\rangle m_e}\nabla(\langle A^2\rangle) = \frac{-m_e c^2}{2\langle\gamma\rangle}\nabla(\langle a^2\rangle) \tag{2.11}$$

where $\langle\rangle$ denotes a time averaged values. For linear polarization, $\langle a^2\rangle = \frac{1}{2}a^2$, while for circular polarization $\langle a^2\rangle = a^2$. Recalling $a^2 \propto I_L$, equation (2.11) demonstrates that electrons will be expelled from regions of high intensity. Noting $\langle\gamma\rangle = \sqrt{1 + \langle a^2\rangle}$, equation (2.11) can be

rewritten

$$F_P = \frac{-m_e c^2}{2\langle\gamma\rangle}\nabla(\langle\gamma^2\rangle - 1). \tag{2.12}$$

From this expression and $F = -\nabla U$, the ponderomotive potential can be derived

$$U_P = m_e c^2(\langle\gamma\rangle - 1). \tag{2.13}$$

If $a \ll 1$ (i.e., non-relativistic limit), the ponderomotive potential for linearly polarized light reduces to

$$U_P = \frac{e^2 E^2}{4 m_e \omega_L}. \tag{2.14}$$

2.1.3 Ionization by intense lasers

To produce a plasma, the laser must ionize the target material by stripping electrons from the ions. At high frequencies, the laser light can directly ionize target electrons if the photon energy is matched to the ionization potential energy (photoelectric effect). However, the frequency of intense lasers is typically below the ionization threshold and the ionization mechanism depends on the laser intensity. At lower intensities, electrons can be ionized by absorbing multiple photons. As the intensity increases, the laser potential can substantially modify the Coulomb potential allowing the electron to tunnel through the potential barrier.

This intensity dependence is captured by the Keldysh parameter which is the ratio of the "tunneling time" to the laser period,

$$\gamma_K = \frac{(2U_i m_e)^{1/2}\omega_L}{eE} \simeq \sqrt{\frac{U_i}{U_P}} \tag{2.15}$$

where U_i is the ionization potential, ω_L is the laser frequency, E is the laser electric field strength, and U_P is the ponderomotive potential. As described in section 2.1.2, the ponderomotive potential is related to the laser intensity. Therefore, the Keldysh parameter can be

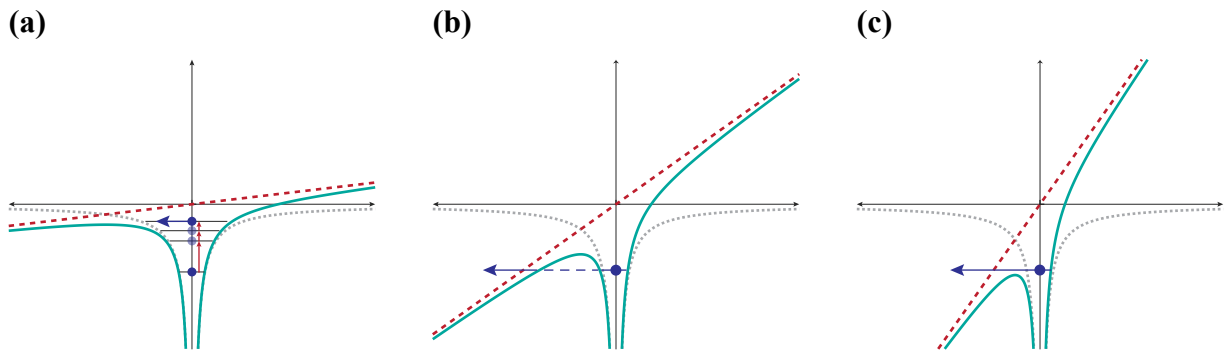

Figure 2.1: Schematics of mechanisms for ionization by intense lasers: (a) multi-photon, (b) tunneling, (c) barrier-suppression. The original Coulomb potential is represented by the gray dashed line, while the laser potential is the red dashed line. The modified potential experienced by the electron is shown in green.

expressed as a function of intensity

$$\gamma_K \approx \frac{2.3 \times 10^6}{\lambda_{\mu m}} \sqrt{\frac{U_i(\text{eV})}{I_L}}, \tag{2.16}$$

where $\lambda_{\mu m}$ is the laser wavelength in microns, I_L is the laser intensity in units of Wcm^{-2}, and the ionization potential is in units of eV. When $\gamma_K > 1$, multiple photons must be absorbed to ionize the atom (multi-photon ionization (MPI)). For $\gamma_K < 1$, tunneling ionization dominates. As the laser field becomes even stronger (i.e., $\gamma_K \ll 1$), the Coulomb barrier can be suppressed such that the electron can escape directly without tunneling (so-called barrier-suppression or field ionization).

These ionization mechanism are compared schematically in Figure 2.1. The intensity at which the ionization mechanism transition from MPI to tunneling is

$$I_L(\text{Wcm}^{-2}) > 5.4 \times 10^{12} \frac{U_i(\text{eV})}{\lambda_{\mu m}^2}. \tag{2.17}$$

For the experiments described in this thesis, the peak intensity often exceeds 10^{19} Wcm^{-2} and each of these mechanisms likely plays a role at different stages as the intensity increases at the front edge of the pulse. Unlike the other mechanisms, field ionization will dominate

because it is not a statistical process.

2.1.4 Laser absorption

This section will describe key mechanisms mediating transfer of laser energy to the plasma. In addition to the textbooks mentioned above, the review on laser absorption by Wilks and Kruer [74] was used for reference. Due to the broad laser intensity and pulse duration range investigated in this thesis, mechanisms for both moderate intensity, long pulses ($I_L \sim 10^{14}$ Wcm^{-2}) and high intensity pulses (relativistic, $I_L > 10^{18}$ Wcm^{-2}) are introduced here.

Resonance absorption

Consider the interaction of a laser wave with a plasma density gradient characterized by the scale length $L_n = |\nabla n_e/n_e|^{-1}$. If the laser is p-polarized and propagates with an incidence angle θ_i, a component of the laser electric field can oscillate electrons across the density gradient and drive plasma waves with frequency $\omega_{pe} = \sqrt{e^2 n_e/\epsilon_0 m_e}$. When $\omega_L = \omega_{pe}$, the plasma waves are resonantly excited. The density at which this occurs is called the critical density,

$$n_c = \frac{\epsilon_0 m_e^* \omega_L^2}{e^2} \tag{2.18}$$

where $m_e^* = \langle\gamma\rangle m_e$ for relativistic laser intensities. At densities greater than n_c, the wave is effectively screened by the plasma response, so the laser reflects from the critical density surface.

The fraction of energy transfered from the laser to resonantly excited waves is given by

$$f_{RA} \approx \frac{\phi^2(\tau)}{2} \tag{2.19}$$

where $\phi(\tau) = 2.3\,\tau \exp(-2\tau^3/3)$ and τ relates the gradient scale length to the angle of incidence $\tau = (\omega_L L_n/c)^{1/3} \sin\theta_i$. The excited waves transfer energy to hot electrons through Landau damping or wave-breaking. Based on numerical simulations, the hot electron tem-

perature in keV was found to scale as

$$T_{hot}[\mathrm{keV}] \approx 10\big[T_{\mathrm{keV}} I_{15} \lambda_{\mu\mathrm{m}}^2\big]^{1/2}, \tag{2.20}$$

where T_{keV} is the background electron temperature in keV, I_{15} is the incident laser intensity in units of 10^{15} Wcm^{-2}, and $\lambda_{\mu\mathrm{m}}$ is the laser wavelength in microns.

Inverse Bremsstrahlung

Also known as collisional absorption, Inverse Bremsstrahlung occurs when electrons oscillating in the laser field collide with an ion, damping the oscillation and heating the plasma. The damping rate, which depends on density, Z and temperature is given by

$$\kappa_{IB} \propto \frac{Z n_e^2}{T_e^{3/2}(1 - n_e/n_c)^{1/2}}. \tag{2.21}$$

Damping is largest for low temperatures, high Z, and for densities approaching n_c.

For a linear density gradient, the absorbed fraction is given

$$f_{IB} = 1 - \exp\big(-\frac{32}{15}\frac{\nu_{ei}(n_c)}{c} L_n\big) \tag{2.22}$$

where $\nu_{ei}(n_c)$ is the electron-ion collision frequency evaluated at the critical density. The collision frequency preserves the dependence on plasma Z and temperature from equation (2.21),

$$\nu_{ei}(n_c) \propto \frac{Z n_c}{T_e^{3/2}}. \tag{2.23}$$

The absorption is maximized for long scale lengths, high Z and low electron temperatures. In addition, since $n_c \propto \omega_L^2$, absorption is enhanced for higher laser frequencies. Inverse bremsstrahlung is typically the dominant absorption mechanism for UV, nanosecond laser pulses, such as those produced by OMEGA EP or the National Ignition Facility (NIF).

Vacuum heating (Brunel effect)

Conceptually similar to resonance absorption, vacuum heating occurs when a laser pulse oscillates electrons across a density gradient. However unlike resonance absorption, the density gradient is very short ($L_n < \lambda_L$), and there is no region of resonant coupling to plasma waves. Instead, electrons are dragged out into vacuum by the laser field before being injected back into the overdense target.

At the target surface, the driving electric field is the summation of incident and reflected waves,

$$E_d = [1 + (1 - f_{vh})^{1/2}]E_L \sin\theta_i = \alpha E_L \sin\theta_i, \tag{2.24}$$

where $\alpha = [1+(1-f_{vh})^{1/2}]$, and f_{vh} is the absorbed fraction defined as the ratio of absorbed intensity to incident intensity, $f_{vh} = I_a/I_L$.

The absorbed intensity can be estimated as the number of electrons accelerated per unit area, divided by the oscillation period, and multiplied by the electron kinetic energy. Using the ponderomotive potential of E_d for the electron energy, (in CGS units)

$$I_a = \frac{N_e}{A}\frac{\omega_L}{2\pi}U_p = \frac{\alpha E_L \sin\theta_i}{4\pi e}\,\frac{\omega_L}{2\pi}\,m_e c^2(\gamma_d - 1) \tag{2.25}$$

where Gauss's law has been used to relate the surface charge density to the driving electric field and

$$\gamma_d = (1 + \frac{v_d^2}{c^2})^{1/2} = (1 + [\alpha\, a_0 \sin\theta_i]^2)^{1/2}. \tag{2.26}$$

Using $I_L = cE_L^2/8\pi$, the full, relativistic vacuum heating absorption fraction can be derived

$$f_{vh} = \frac{1}{\pi a_0}\alpha\big[(1 + \alpha^2 a_0^2 \sin^2\theta_i)^{1/2} - 1\big]\frac{\sin\theta_i}{\cos\theta_i}. \tag{2.27}$$

In the low intensity limit, $a_0 \ll 1$, this expression reduces to

$$f_{vh} \approx \frac{a_0}{2\pi}\,\alpha^3\,\frac{\sin^3\theta_i}{\cos\theta_i}. \tag{2.28}$$

and the absorption can be as high as 70%. However, at very high intensity, $a_0 \gg 1$, the absorption saturates at around $10-15\%$, and the expression for the absorbed fraction becomes

$$f_{vh} \approx \frac{\alpha^2}{\pi}\,\frac{\sin^2\theta_i}{\cos\theta_i}. \tag{2.29}$$

The electron temperature should scale with the ponderomotive potential of the laser.

$J \times B$ heating

At relativistic intensities, the electron oscillation velocity approaches the speed of light ($v_{os} \sim c$) and the $v \times B$ term in the Lorentz force becomes significant. The absorption is similar to vacuum heating, electrons are accelerated across the density interface into the dense target. A signature of $J \times B$ heating is that electrons are injected at a frequency $2\omega_L$. This can be understood by considering the ponderomotive force from equation (2.11),

$$F_p \propto \langle A_0^2 \sin^2(\omega_L t)\rangle \rightarrow \langle \frac{A_0^2}{2}(1+\cos(2\omega_L t)\rangle \tag{2.30}$$

Electrons will be kicked into the dense plasma by the ponderomotive force of the laser at a frequency of $2\omega_L$. The hot electron temperature for $J \times B$ heating is given by the ponderomotive potential, and scales with laser intensity as

$$T_{hot} = m_e c^2\left[\sqrt{1+\frac{I_L\lambda_{\mu\mathrm{m}}^2}{2.8\times10^{18}}}-1\right] \tag{2.31}$$

where the intensity is in units of Wcm^{-2} and the wavelength is in mircons.

2.2 Ion acceleration

With current laser technology, all laser-driven ion acceleration is indirect. The laser first accelerates plasma electrons, and the resulting electric fields accelerate the ions. The most well studied laser-driven ion acceleration mechanism is target normal sheath acceleration (TNSA) [50–53]. During a high intensity laser-solid interaction, the laser accelerates a population of hot electrons (as described in the previous sections). Hot electrons will stream through the target and expand into vacuum. The resulting charge imbalance produces a strong electric field along the target surface which accelerates ions in the target normal direction. Due to the high charge to mass ratio, protons from hydrocarbon contaminants on the target surface will be preferentially accelerated.

The strength of the sheath electric field can be estimated with a 1D model of plasma expansion into vacuum driven by hot electrons [75–78]. In the model presented by Mora [78], the electron density is given by

$$n_e(x) = n_{e0} \exp\big(e\phi(x)/k_B T_e\big) \tag{2.32}$$

where ϕ is the electrostatic potential and $k_B T_e$ is the hot electron temperature. The Poisson equation can be used to relate the potential to the electron density

$$\frac{\partial^2 \phi(x)}{\partial x^2} = -\rho/\epsilon_0 = e(n_e - Z n_i)/\epsilon_0 \tag{2.33}$$

where ϵ_0 is the vacuum permittivity and Z is the ion charge. More details of the model are discussed in Appendix A, but the key results are summarize here.

The electric field is given by $E = -\partial\phi(x)/\partial x$, and integration of the Poisson equation yields

$$E = \sqrt{2}\,\frac{k_B T_e}{e\lambda_D^*}, \tag{2.34}$$

where λ_D^* is the local Debye length ($\lambda_D^* = \lambda_{D0}(n_{e0}/n_e)^{1/2}$, with $\lambda_{D0} = \sqrt{\epsilon_0 k_B T_e/n_{e0}e^2}$).

The Mora model predicts an energy spectrum for ions per unit surface given by

$$\mathrm{d}N/\mathrm{d}\mathcal{E}_i = \frac{n_{i0}c_s t}{\sqrt{2\mathcal{E}_i\mathcal{E}_0}} \exp\big(-\sqrt{2\mathcal{E}_i/\mathcal{E}_0}\big) \tag{2.35}$$

where n_{i0} is the ion density, $c_s = \sqrt{Zk_BT_e/m_i}$ is the ion sound speed, $\mathcal{E}_i$ is the ion kinetic energy, and $\mathcal{E}_0 = Zk_BT_e$. The spectrum exhibits a well defined cutoff energy at

$$\mathcal{E}_{max} = 1/2m_iv_f^2 = 2\mathcal{E}_0[\ln(\tau + \sqrt{\tau^2+1})]^2. \tag{2.36}$$

where v_f is the velocity of the expansion and $\tau = \omega_{pi}t/\sqrt{2e_N}$ with $\omega_{pi} = \sqrt{n_{e0}Ze^2/m_i\epsilon_0}$. A reasonable estimate of the ion spectrum and maximum energy can be obtained by assuming the acceleration time is approximately the laser pulse duration, $t \approx t_p$ [79].

This 1D model certainly does not capture the complicated physics of the laser-plasma interaction, time dependence of the electron temperature, the effect of magnetic fields, or multidimensional effects. However, the Mora model provides key insight into the relationship between the hot electron temperature and the maximum electric field and subsequent maximum ion energy. In addition, the maximum energy diverges as the laser pulse duration (acceleration time) increases, making the model unsuitable for longer pulse durations.

An alternative approach for describing the TNSA mechanism was developed by Schreiber *et al.* [4]. Unlike the plasma expansion model used by Mora, this model is on based a disk of charge located on the target surface. The model assumes the laser pulse accelerates an electron bunch containing N_e particles with a length $L = ct_p$. At the rear target surface, the charge is uniformly distributed within a radius

$$B = r_L + d\tan\theta,$$

where r_L is the laser focal spot radius, d is the target thickness and θ is the divergence angle of the hot electrons. Using this charge distribution, solution of Poisson equation yields an

electric field given by

$$E(x) = \frac{k_B T_e}{e\lambda_{D0}}\left[1 - \frac{x/B}{\sqrt{1+(x/B)^2}}\right] \tag{2.37}$$

which agrees with the results from the Mora plasma expansion model at $x = 0$ but stays finite as $x \to \infty$. Again, λ_{D0} is the Debye length at the peak hot electron density (n_{e0}).

The maximum ion energy that could theoretically be achieved in such a field is found to be

$$\mathcal{E}_{i,\infty} = Z k_B T_e B/\lambda_{D0}. \tag{2.38}$$

Noting that laser energy $\mathcal{E}_L$, is absorbed into hot electrons with an efficiency η such that $N_e k_B T_e = \eta \mathcal{E}_L$, the maximum energy expression can be rewritten in terms of the absorbed laser power,

$$\mathcal{E}_{i,\infty} = 2Z m_e c^2 (\eta P_L/P_R)^{1/2}, \tag{2.39}$$

where $P_L = \mathcal{E}_L t_p$, $P_R = m_e c^3/r_e = 8.71$ GW is the "relativistic power", and r_e is the classical electron radius. Based on experimental results, the conversion efficiency for 1 μm light can be approximated by $\eta = 1.2 \times 10^{-15}\ I_L^{3/4}$, with $I_L = P_L/(\pi r_L^2)$ in Wcm^{-2}, up to a maximum value of $\eta = 0.5$. Finally, an expression relating the laser pulse duration and maximum experimentally observable ion energy ($\mathcal{E}_m$) can be found by integrating an equation of motion,

$$\frac{t_p}{t_0} = X\left(1 + \frac{1}{2}\frac{1}{1-X^2}\right) + \frac{1}{4}\ln\left(\frac{1+X}{1-X}\right), \tag{2.40}$$

where $X = (\mathcal{E}_m/\mathcal{E}_{i,\infty})^{1/2}$, and $t_0 = B/v_\infty$ is the ballistic time, with $v_\infty = (2\mathcal{E}_{i,\infty}/m_i)^{1/2}$. While this is a relatively opaque result, this expression can be used to make reasonable estimates of the maximum measured ion energy. Unlike the plasma expansion model used by Mora, this expression saturates as the acceleration time increases. For this reason, the Schreiber model was used to interpret ion acceleration results using very long pulse durations in Chapter 4. In addition, this model only depends on the laser parameters and other parameters which can, in principle, be experimentally measured (electron divergence angle,

conversion efficiency).

While TNSA is the only mechanism discussed in detail in this thesis, many other mechanisms for laser-driven ion acceleration have been identified. As with TNSA, laser energy is first absorbed into hot electrons which then establish accelerating field structures. A more complete discussion of ion acceleration mechanisms can be found in reviews by Macchi *et al.* [80] and Daido *et al.* [81], however a few mechanism are mentioned here primarily to draw contrasts with TNSA. In particular, alternative approaches can yield peaked spectra, with quasi-monoenergetic features which may be better suited to future applications of laser-driven ion sources.

For example, rather than using intact solid foils, collisionless shock acceleration (CSA) can be driven using near-critical density targets with specially tailored profiles [82–84]. The high intensity laser pulse heats electrons and the ponderomotive pressure steepens the electron density profile, driving a collisionless shock into the target. As the shock propagates, the accompanying electric field structure can reflect ions to twice the shock velocity. The result is a quasi-monoenergetic ion beam with energy $\mathcal{E}_i \approx 2m_i v_{shock}^2$.

2.3 Magnetic field generation

The experiments described in this thesis explored laser-driven magnetic field generation in two distinct intensity regimes. While the details will be described in more depth in Chapter 5, this section will introduce the basic concepts of magnetic field generation with either moderate or high intensity laser pulses.

Moderate intensity lasers: Biermann battery mechanism

Rapid heating during the interaction of a moderate intensity laser pulse with an overdense target ablates the surface. Within the ablated plasma plume, strong temperature and density gradients can spontaneously generate strong magnetic fields. The origin of such fields can

be understood by combining the pressure term in Ohm's law and Faraday's law.

The electric field is related to the electron plasma pressure by

$$\vec{E} = -\frac{\nabla P_e}{e n_e}. \tag{2.41}$$

Substituting into Faraday's law and taking $P_e = n_e k_B T_e$,

$$\frac{\partial \vec{B}}{\partial t} = -\nabla \times \vec{E} = \frac{1}{e}\nabla \times \left(\frac{\nabla P_e}{n_e}\right) = -\frac{k_B}{e n_e}\nabla n_e \times \nabla T_e \tag{2.42}$$

This result is known as Biermann battery (or $\nabla n_e \times \nabla T_e$) mechanism [85], and shows that misalignment of density and temperature gradients in the plasma can drive magnetic field generation.

In a laser-produced plasma, the density gradient is primarily oriented toward the target surface, while the temperature gradients are oriented radially, pointing inward toward the center of the ablated plasma. As a result, an azimuthal magnetic field is generated in the regions with strongest gradients [7, 86, 87]. Measurements made using Faraday rotation [86, 87] or proton imaging [8, 16, 47, 58, 88] have observed MegaGauss field strengths. The fields expand radially with the thermal plasma and are advected by fast electrons with speeds on the order of the sound speed, c_s [16]. A schematic representation of the field generation geometry is shown in Figure 2.2(a).

High intensity lasers

As described in previous sections, high intensity laser pulses with $a_0 > 1$ can accelerate a population of relativistic electrons. A strong sheath electric field is established as hot electrons expand into vacuum from the target surface. This sheath field is strong enough that many electrons are turned back toward the target and confined to expand radially. The result is a radial relativistic electron current which drives the sheath field across target surface with a velocity near the speed of light [89]. Accompanying the radially expanding

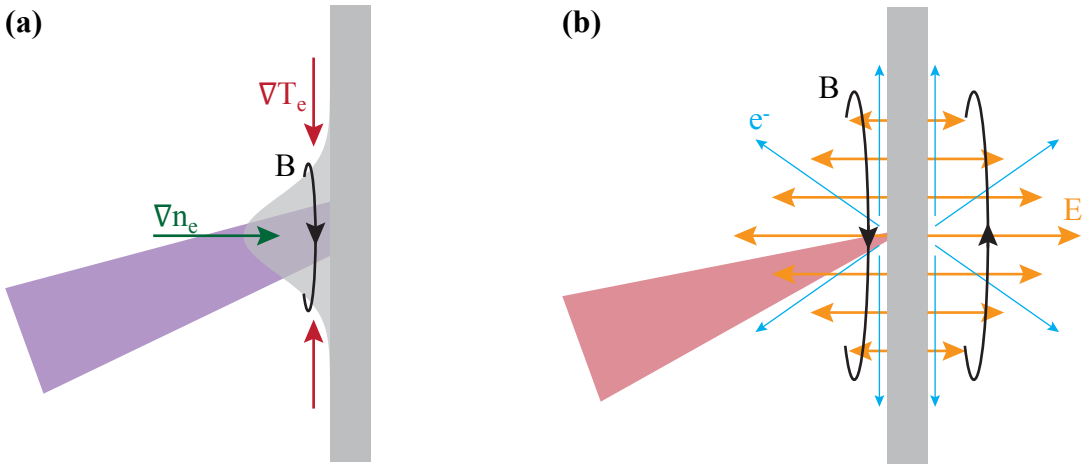

Figure 2.2: Schematic descriptions of magnetic field generation by the interaction of (a) moderate or (b) high intensity laser pulses with overdense targets.

sheath is an inductive magnetic field [9, 10].

Returning to Faraday's law, the inductive magnetic field is related to the sheath electric field by

$$\frac{\partial \vec{B}}{\partial t} = -\nabla \times \vec{E} \Rightarrow \frac{\partial B_\theta}{\partial t} = \frac{\partial E_z}{\partial r}. \tag{2.43}$$

Therefore, transverse gradients in the electric field generate an azimuthal magnetic field. A schematic of the field generation is shown in Figure 2.2(b).

Experimental measurements of such fields using relativistic electron [9] or proton imaging [10] have $\sim$ 100 MG peak field strengths, orders of magnitude stronger than those generated during moderate intensity interactions. In addition, speed of light magnetic field expansion velocities were observed. New measurements and simulations of the magnetic field generation, as well as more details about the generation mechanism can be found in Chapter 5.

2.4 Magnetic reconnection

Magnetic reconnection is a process by which magnetic energy is converted into plasma kinetic or thermal energy. Reconnection is traditionally considered in magnetohydrodynamics

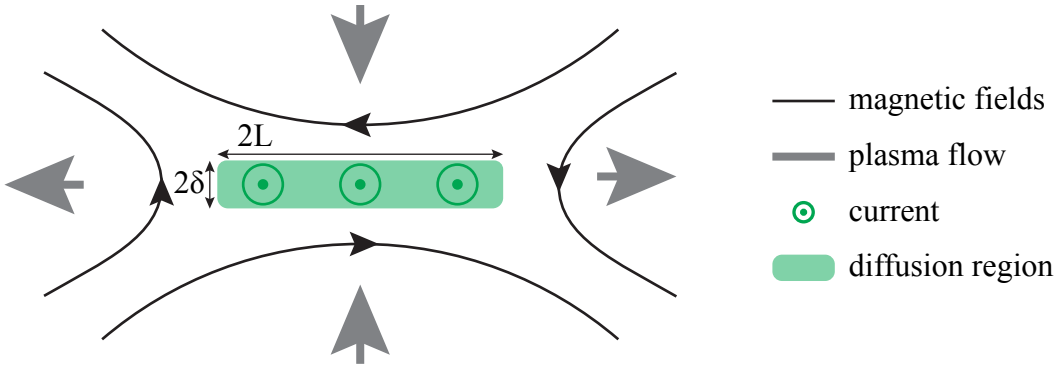

Figure 2.3: Diagram of Sweet-Parker magnetic reconnection. Magnetic field lines break and reconnect within the diffusion region, and an out-of-plane current sheet is established. The diffusion region is characterized by the length L and width δ.

(MHD) systems where the magnetic field is "frozen" into the plasma flow. When opposing fields are driven together, the fields will slip from the plasma in a small region with fields lines breaking and reconnecting at speeds faster than classical diffusion rates. The fields rearrange into a lower energy configuration, and the excess energy is transferred to the plasma particles.

Reconnection plays an important role in numerous astrophysical processes, such as solar flares [90], and is thought to be responsible for more exotic particle acceleration phenomena, including gamma ray bursts [28]. Reconnection is also found in laboratory plasmas, such as self-organization of fusion plasma [91, 92]. Numerous dedicated laboratory reconnection experiments have been developed to examine the underlying physics, including using laser-driven magnetic fields. While not the principal aim of the majority of the work in described in this thesis, reconnection motivated the exploration of laser-driven magnetic field generation. For this reason, the fundamental physics of reconnection is briefly described in this section. More complete discussions can be found recent reviews by Yamada *et al.* [27] or by Zweibel *et al.* [26].

2.4.1 Sweet-Parker reconnection

The typical starting point for reconnection theory is the model developed by Sweet [93] and Parker [94]. This model considers two plasmas with magnetic fields $\pm B$, electrical resistivity η, and mass density ρ, moving toward each other with a velocity v_{in}. In the midplane, the diffusion region is characterized by a length L and width δ. The reconnected field and plasma outflow moves away from the diffusion region with a velocity v_{out}. The basic geometry of the Sweet-Parker models is shown in Figure 2.3.

From Faraday's law, changes to the magnetic field must be accompanied by a perpendicular electric field component. To understand the out-of-plane electric fields, it is useful to refer to Ohm's law,

$$\vec{E} = -\vec{v} \times \vec{B} + \eta \vec{J}. \tag{2.44}$$

However, the Sweet-Parker model assumes the system is in steady-state (i.e., $\partial B/\partial t \sim 0$), therefore the out-of-plane current is approximately

$$J \sim -v_{in} B/\eta. \tag{2.45}$$

Using Ampere's law (neglecting the displacement current),

$$\nabla \times \vec{B} = \mu_0 \vec{J} \Rightarrow J \sim \frac{B}{\mu_0 \delta}. \tag{2.46}$$

Combining equations (2.45) and (2.46), an expression relating the width of the diffusion region and the inflow velocity can be found,

$$\delta = \frac{\eta}{\mu_0 v_{in}} = \frac{\eta_M}{v_{in}}, \tag{2.47}$$

where η_M is the magnetic diffusivity. This relation demonstrates that the width of the diffusion region is directly proportional to the resistivity, while inversely proportional to the

inflow velocity.

Assuming the plasmas are incompressible, mass continuity gives $v_{in}L = v_{out}\delta$. Taking $v_{out} = v_A$, where $v_A = \sqrt{B/\mu_0\rho}$ is the Alfvén velocity, and combining with equation 2.47, the Sweet-Parker reconnection rate can be derived,

$$\frac{v_{in}}{v_A} = \frac{\delta}{L} = S^{-1/2}. \tag{2.48}$$

The Lundquist number, $S = v_A L/\eta_M$, relates the diffusion time ($t_{diff} = L^2/\eta_M$) to the global Alfvén time ($t_A = L/v_A$).

Sweet-Parker reconnection is governed by the spatial scale of the diffusion region and the resistivity. Energy is transferred from the fields to the plasma through resistive heating. However, this model predicts slow reconnection rates, often orders of magnitude slower than observed rates. To reconcile the reconnection rate discrepancy, models for "fast" reconnection have been developed. For example, the Petschek model [95] uses a much smaller diffusion region (i.e., $L_P \ll L_{SP}$). Slow shocks are invoked to help convert magnetic energy in to particle kinetic energy. Rates predicted by the Petschek model are fast enough to agree with observations.

2.4.2 Collisionless reconnection

In collisionless systems, the plasma resistivity is very small. From equation (2.47), this will result in a very thin reconnection region. If δ is smaller than the ion skin depth ($d_i = c/\omega_{pi}$), then ions will decouple from the electrons as the plasmas approach the midplane. This decoupling which occurs on length scales near d_i establishes an in-plane current, $J = en_e(v_i - v_e)$, and Ohm's law must be updated to include the Hall term,

$$\vec{E} = -\vec{v} \times \vec{B} + \eta\vec{J} + \frac{\vec{J} \times \vec{B}}{en_e}. \tag{2.49}$$

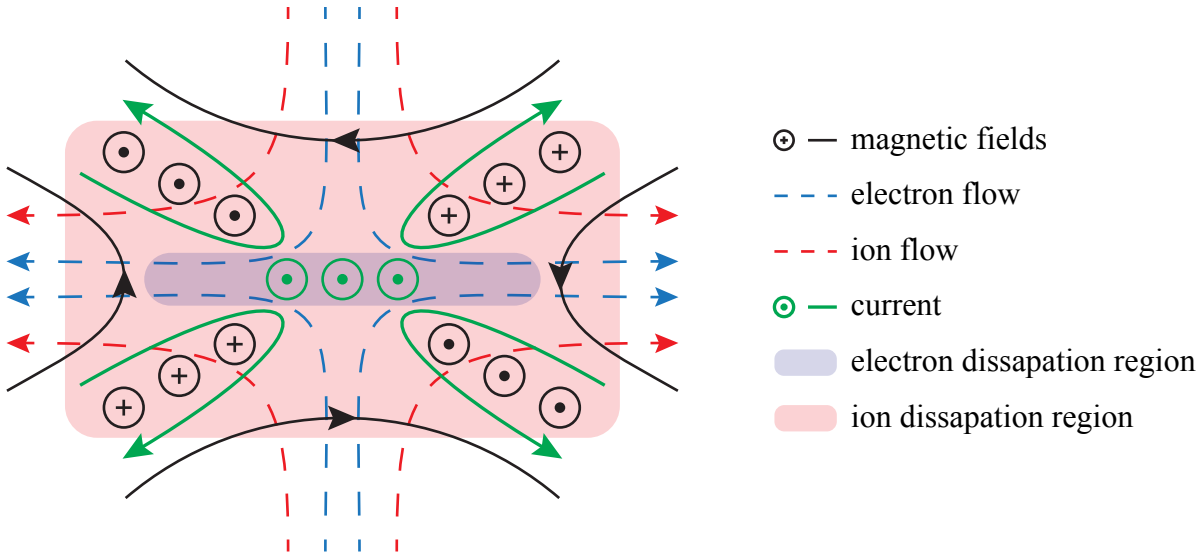

Figure 2.4: Diagram of collisionless magnetic reconnection. As the flows approach the mid-plane, ions decouple from the electrons. The resulting current produces an out-of-plane, quadrupole magnetic field structure. Reconnection occurs within the narrow electron dissipation region.

As stated previously, η is small, so the reconnection electric field is supported by the in-plane current from the third term on the right-hand side of Ohm's law.

The collisionless reconnection geometry (similar to "two-fluid" reconnection) is sketched in Figure 2.4. Field reconnection occurs in the narrow electron dissipation region, which has a characteristic width of $d_e = c/\omega_{pe}$. A key signature of collisionless reconnection is the formation of a quadrupole out-of-plane magnetic field structure as a consequence of the in-plane currents.

Collisionless reconnection can proceed at much faster rates than the Sweet-Parker model, However, it is not applicable to many astrophysical phenomena. Due to the high electron temperatures, laser-produced plasmas are often collisionless, especially from high intensity interactions. Indeed, quadrupole field structures were observed in recent simulations of high intensity laser-driven reconnection [44].

2.4.3 Relativistic reconnection

In more exotic astrophysical phenomena, such as gamma ray bursts, pulsar winds or jets from active galactic nuclei, the magnetic fields can be so strong that the energy density in the field exceeds the plasma energy density. This is often characterized by σ_{cold}, the magnetization parameter

$$\sigma_{cold} = \frac{B^2}{\mu_0 n_e m_e c^2} \tag{2.50}$$

which is the ratio of the magnetic energy density to the rest mass energy density of the plasma. When σ_{cold} exceeds unity, reconnection can accelerate or heat the plasma to relativistic energies. As such, relativistic reconnection is thought to play a role in high energy cosmic ray acceleration observed throughout the universe [96].

Relativistic reconnection is typically approached using a similar theoretical framework to that presented above, thought it is often considered in electron-positron pair plasmas [31]. Figure 2.5 shows a phase diagram of electron density and magnetic field strength. Contours of σ_{cold} are plotted along with a number of astrophysical phenomena (interpreted from [3]). In addition, a few laboratory based reconnection experiments are shown, including laser-driven cases. Due to the strong fields, high intensity lasers can access a trans-relativistic regime, where $\sigma_{cold} > 1$ for plasma electrons. Note: reconnection plasmas with very relativistic temperatures or inflows can also be characterized by σ_{hot}, which takes into account the full energy flux into the reconnection region

$$\sigma_{cold} \gg \sigma_{hot} = \frac{\sigma_{cold}}{\langle\gamma\rangle + P/m_e c^2} \sim \frac{B^2}{\mu_0 n_e (4 k_B T_e)} \tag{2.51}$$

where $\langle\gamma\rangle$ is the average Lorentz factor for the distribution and P is the plasma pressure [97].

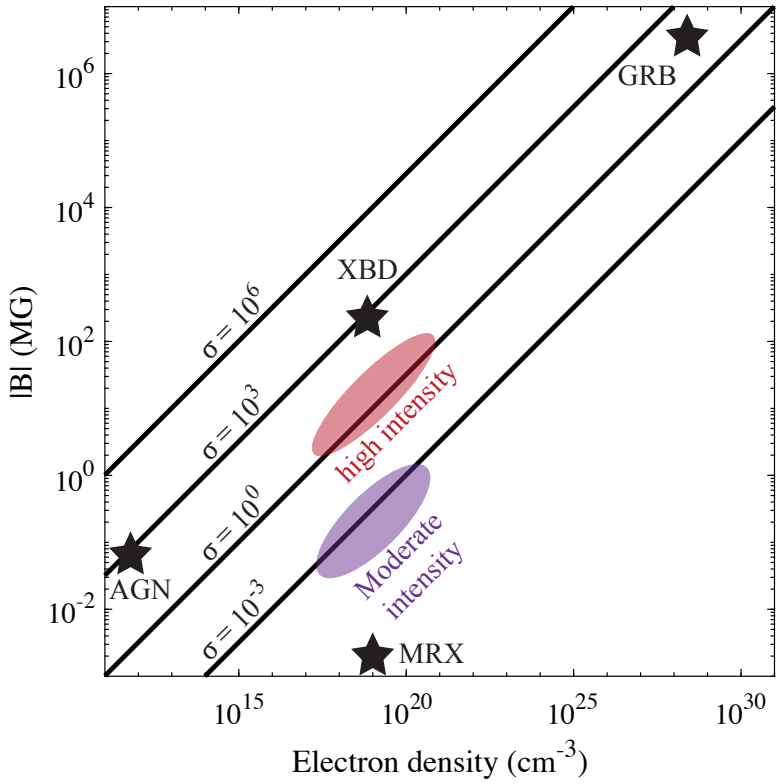

Figure 2.5: Contours of σ_{cold} are plotted in a B-n_e phase diagram. Relativistic reconnection can occur for $\sigma_{cold} > 1$. For context, astrophysical and experimental systems are also plotted, where AGN = active galactic nuclei coronae, XBD = X-ray binary disk coronae, GRB - gamma ray burst, MRX = the Magnetic reconnection experiment at Princeton Plasma Physics Laboratory [3]. The phase diagram locations of laser-driven magnetic fields are also shown.

CHAPTER 3

Methods and Capabilites

In this chapter, key experimental and computational methods will be discussed. After a brief review of high power laser technology and the OMEGA EP laser system, methods for proton detection, energy spectrum reconstruction and image inversion will be detailed. Finally, the particle-in-cell (PIC) simulation code OSIRIS will be introduced.

3.1 High Power Lasers

The basic elements of a laser are an optical cavity, a gain medium, a pump (energy source) and a seed. An optical cavity consists of two mirrors, one of which is either partially transparent or acts as an optical switch to allow light to escape. The gain medium is positioned within the cavity, and is a material which exhibits an electronic energy structure that lends itself to a population inversion. As a result, when an external energy source (the pump) is applied, large fraction of electrons in the gain medium are excited to a metastable state. When stimulated, often by spontaneous emission or a seed pulse, electrons will decay to the ground state, giving off the excess energy as light which is coherent with the stimulating light wave. A resonant wave in the cavity extracts energy from the gain medium and is amplified. Remove the cavity and the gain medium can act as an amplifier, used to boost the energy of a laser wave during a single pass.

Short pulses are commonly produced using techniques such as Q-switching or mode-locking (based on the constructive interference of laser cavity modes) [98]. The wavelength

of light depends on the electronic structure of the gain medium, and in mode-locked lasers the pulse duration is intrinsically transform limited by the spectral bandwidth of the emission (often represented by the time-bandwidth product, $\Delta\omega\tau \sim 1$). For example, titanium-doped sapphire has a broad bandwidth ranging from 700 nm to 1100 nm, and can therefore support ultrashort, fs-duration pulses. The OMEGA EP laser is primarily based on neodymium-doped glass (Nd-Glass) amplifiers which are pumped by flashlamps and lase with a central wavelength of 1.054 μm.

The basic components described above serve as the foundation for high power lasers. To reach high peak powers, a short, low energy pulse is passed through a series of amplification stages, gradually extracting energy from the pumped amplifiers at each stage. Before the invention of chirped pulse amplification (CPA, discussed in more detail below), the maximum peak power achievable through this staged amplification approach was limited by the damage threshold of optical components ($\sim$Jcm^{-2}) and the onset of nonlinear behavior in the gain medium at GWcm^{-2} intensities. Operating with nanosecond pulses, OMEGA EP can reach TW powers by using large aperture amplifiers. The potential for further improvement with this conventional laser technology is limited due to the financial costs and technological challenge of producing very large high quality amplifiers. However, the invention of chirped pulse amplification by Strickland and Mourou in 1985 [99] has enabled the production of extremely high peak power laser pulses.

3.1.1 Chirped pulse amplification (CPA)

Figure 3.1 shows a schematic representation of the CPA [99] approach for producing high peak power laser pulses. A grating pair, called the stretcher, is used to stretch a low energy short pulse in time. The first grating in the stretcher spatially disperses the different frequencies contained in the pulse. The second grating returns all of the frequencies to the same path, but the lower frequencies have traveled a shorter distance and are temporally spread out ahead of higher frequencies. The resulting frequency "chirped" pulse has a much longer

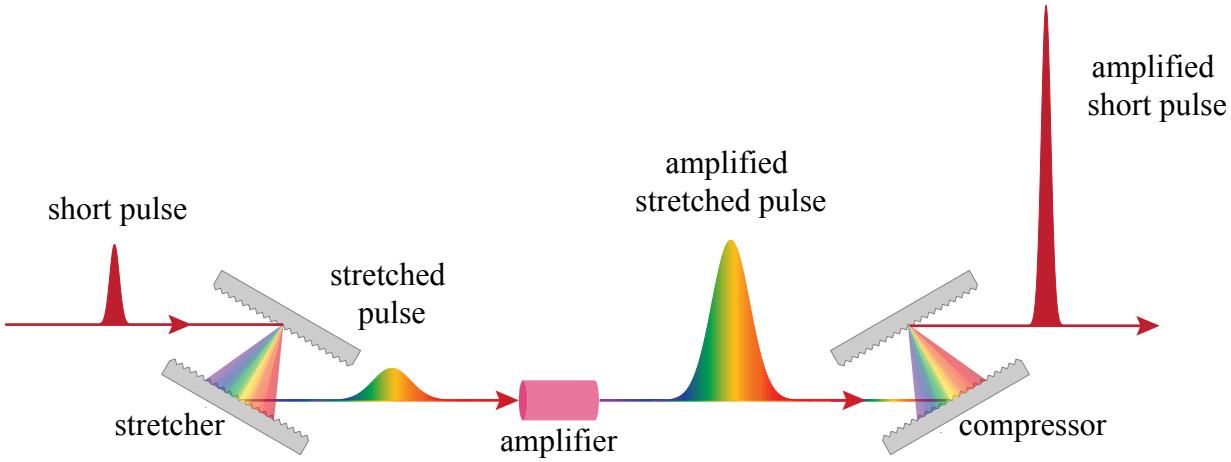

Figure 3.1: Schematic of chirped pulse amplification

duration, and therefore lower power. After passing through amplification stages, the pulse is re-compressed by a second grating pair called the compressor, which inverts the stretching process. The result is a short pulse with much higher energy than conventionally permitted by the nonlinear behavior in the gain medium. Using the CPA technique, PW peak powers and ultrahigh intensities up to 10^{23} Wcm^{-2} have been achieved.

3.1.1.1 Optical parametric chirped pulse amplification (OPCPA)

As the power is increased, CPA systems eventually reach the same nonlinear and damage limits. Further power improvements can be achieved by shortening the output pulse duration. Because the final pulse duration is related to the Fourier transform of the pulse frequency spectrum, shorter pulses can be produced by incorporating an optical parametric amplifier (OPA) to amplify a broader spectral bandwidth and avoid gain narrowing in multipass amplifiers [100, 101]. Conceptually, an OPA uses a nonlinear crystal with high bandwidth to convert energy from a higher frequency pump to a low energy seed. As a consequence of the conversion, an additional "idler" pulse is generated such that energy and momentum are conserved [102],

$$\omega_p = \omega_s + \omega_i$$

$$\vec{k}_p = \vec{k}_s + \vec{k}_i,$$

where ω is the frequency of light, $\vec{k}$ is the wave vector, and p, s and i designate the pump, seed and idler, respectively.

For an OPCPA system, the OPA is included after the seed pulse has been stretched. The nonlinear crystal is often lithium triborate (LBO) [103] or beta barium borate (BBO) [100, 101]. To optimize conversion efficiency, the pulse duration of the pump should be matched to the stretched seed. When amplifying chirped pulses, the pump should have a "top hat" temporal profile in order to take advantage of the broad bandwidth of the crystal and to minimize gain narrowing effects (amplifying all parts of the spectrum uniformly).

The addition of the OPA can also improve the laser contrast ratio. High power laser pulses typically exhibit amplified spontaneous emission (ASE) and prepulses which propagate picoseconds to nanoseconds ahead of the main pulse and can disrupt or destroy the target. A high contrast between the prepulse and main pulse is required for most high intensity laser-solid interactions experiments, such as laser-driven ion acceleration. In more conventional amplifiers, such as the flash lamp pumped Nd:glass mentioned above, the pump is much longer than the seed, so ASE and prepulses can be amplified to a similar degree as the main pulse. However, the duration of the pump in an OPA is closely matched to the seed duration, therefore only light within that temporal window is amplified and the contrast is improved.

3.1.2 OMEGA EP laser system

The experimental work described in this thesis was conducted with the OMEGA Extended Performance (EP) laser system located at the University of Rochester's Laboratory for Laser Energetics [104]. OMEGA EP was built as a high energy, petawatt-class extension to the OMEGA Laser, a 60 beam laser facility primarily dedicated to exploration of direct-drive inertial confinement fusion. The OMEGA EP system can be integrated into OMEGA experiments to drive x-ray or proton radiography sources or to facilitate fast ignition research [105].

In addition, the system can be operated independently for high intensity laser-plasma interactions experiments.

OMEGA EP consists of 4 beam lines, two of which can be compressed to short pulses. One of the key strengths of OMEGA EP is the flexibility of the laser system. When configured for short pulses, the laser can produce pulses with a 1.053 μm central wavelength and durations ranging from 0.7 to 100 ps. Due to the damage threshold of the optical components, the maximum pulse energy is scaled as a function of duration, currently limited to 0.5 kJ in a 0.7 ps pulse, 1.25 kJ in 10 ps, to 2.3 kJ in 100 ps [106]. The short pulses are focused with independent $f/1.8$ parabolic mirrors, and can reach on-target intensities exceeding 10^{20} Wcm^{-2}.

All four beams can be configured to generate ultraviolet (UV) long pulses, with durations ranging from 0.1 to 10 ns and up to 5 kJ of energy. The light is frequency tripled to 351 nm and focused using distributed phase plates (DPPs) to produce super-Gaussian spots with 400 to 2000 μm diameters. While square pulses are commonly used, the temporal pulse shape can be independently customized.

The key technologies that enable the high peak power operation are OPCPA, large or high damage threshold optics, and deformable mirrors [104]. Each short pulse beam line is equipped with two stages of optical parametric amplification pumped by a frequency doubled ND:YLF laser (526.5 nm). The low energy seed is amplified from $\sim$1 nJ to $\sim$100 mJ before further amplification to the kJ level by Nd:glass amplifiers. In addition to producing a high bandwidth pulse, the OPCPA system also results in a power contrast ratio of $\sim 10^9$ [103]. In order to maintain a fluence beneath the damage threshold, large aperture (40 cm) Nd:glass amplifiers, plasma-electrode Pockels cells and tiled grating are used to accommodate larger beam diameters. The tiled gratings are located in the compressor and consist of 3 independent gratings arranged side-by-side. The tiles are precisely aligned such that the full assembly behaves as one large grating with an area of 140×40 cm^2. Finally, to achieve high focused intensities on target, a deformable mirror is used to correct any distortions to the

laser wavefront accumulated during amplification or introduced by the final focusing optic.

3.2 Proton detection: Radiochromic film

Radiochromic films (RCF) are routinely used in high intensity laser-plasma interaction experiments to diagnose radiation emission, especially high energy proton beams. The active layer of the film consist of di-acetylene monomers suspended in gelatin. Polymerization is initiated upon exposure to ionizing radiation, resulting in a color change. In newer Gafchromic™ radiochromic films, the combination of the polymer absorption and yellow dye added by the manufacturer causes the film to change from a yellowish color to green after exposure. For a more complete review of the different film types available and the chemical composition of the constituent layers, see the helpful review by Devic *et al.* [107].

In typical laser-driven ion acceleration experiments, such as those conducted at the OMEGA EP laser facility located at the Laboratory for Laser Energetics of the University of Rochester, stacks of radiochromic film take advantage of the Bragg peak in proton stopping power to simultaneously record spectral and spatial information about the accelerated beam (for more discussion of laser-driven ion acceleration see Chapter 4). Due to the relatively short stopping range for higher Z ions, and the small dose contributions of electrons and x-rays, the stacks of film primarily measure protons. Laser-driven proton beams often exhibit an exponential spectrum, with far more lower energy protons than at higher energy. For this reason, the initial layers in the RCF stack are commonly the Gafchromic HD-V2 model film, which is designed for a dose range from 10 - 1000 Gy. Recent work has demonstrated that the HD-V2 dose range can be extended to ultra-high doses (up to 10 kGy) [108]. The higher sensitivity MD-V3 model with a dose range from 0-100 Gy is used for the deeper layers in the stack to measure the higher energy portion of the spectrum where the proton number is expected to be lower. These two film types are sketched in Figure 3.2. HD-V2 film is composed of a thin active layer, nominally 8 μm thick, on top of a 97 μm

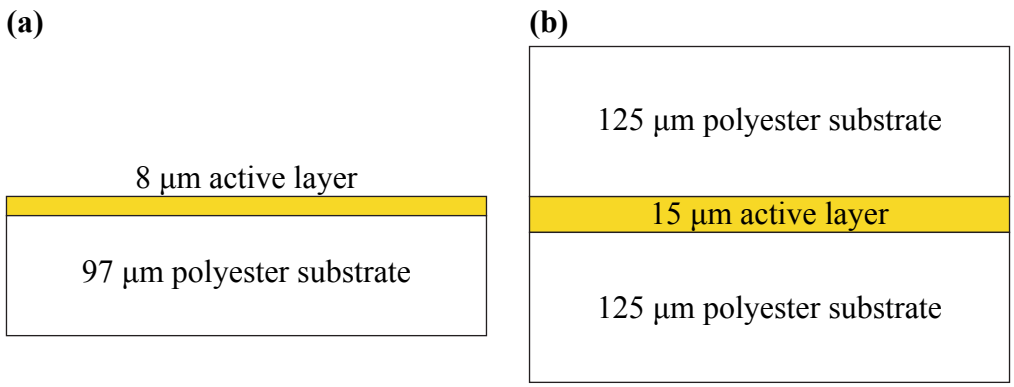

Figure 3.2: Commonly used Gafchromic^{TM} Radiochromic films: (a) HD-V2 and (b) MD-V3

thick polyester substrate. MD-V3 has a thicker active layer, nominally 15 μm, between two layers of polyester.

Once exposed to protons, the film is typically digitized using a flat bed scanner. In order to perform quantitative analysis, the film must be calibrated to relate the digital pixel values to the dose deposited by the protons. While the dose *rate* varies for different types of ionizing radiation, the response (i.e. film darkness as a function of dose) of RCF is similar whether it is exposed to photons, electrons, or protons [109]. Chen *et al.* used 10 MeV photons from a medical linear accelerator (LINAC) to demonstrate that the digital pixel values for a given dose were consistent in the green color channel or in grayscale across various models of EPSON flatbed scanners [110]. Therefore, no matter the radiation source or exact scanner model, published calibration curves may be used provided the measurements are made with the green channel or grayscale of an EPSON flatbed scanner.

An example of such a calibration curve is found in recent work by Bin *et al.* [108]. Using nanosecond ion bunches from the Neutralized Drift Compression Experiment II (NDCX-II) accelerator at Lawrence Berkeley National Laboratory (LBNL), the authors calibrated HD-V2 film up to 100 kGy with an EPSON V600 scanner. The results were fit with the following expression for dose (in Gy) as a function of film optical density (OD),

$$\text{Dose}(\text{OD}) = 374.6 \cdot \text{OD} + 2557 \cdot \text{OD}^{3.085}, \tag{3.1}$$

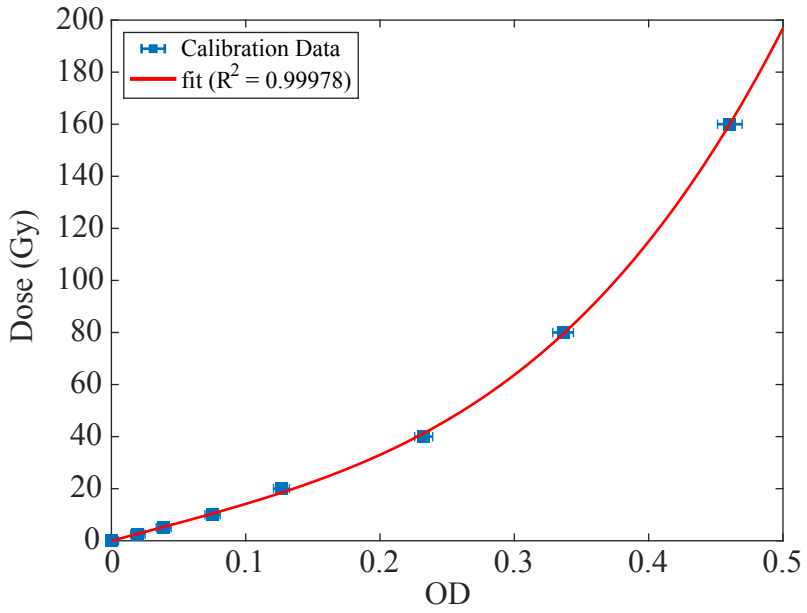

Figure 3.3: MD-V3 calibration results

where OD is calculated as $\text{OD} = -\log_{10}\left(\frac{\text{Exposed pixel value}}{\text{Unexplosed pixel value}}\right)$.

To date, no calibration of MD-V3 with EPSON scanners has been published. With the help of scientists from the department of Radiation Oncology at Michigan Medicine, we conducted an experiment to calibrate MD-V3 film. We followed procedures developed at the hospital to calibrate RCF for medical applications. The exposures were performed Varian Trilogy® LINAC using x-rays generated by a 6 MV electron beam. The dose rate was absolutely calibrated by an ionization chamber placed 100 cm from the source. The ionization chamber was placed beneath a 10 cm thick slab of water-equivalent plastic. Another 10 cm thick slab of water-equivalent plastic positioned beneath the ionization chamber to mitigate backscattered radiation. The x-rays illuminated a 10 cm × 10 cm square area.

The LINAC control software describes dose in terms of "monitor units" (Mu), and delivery rate was set to 600 Mu/min. A dose rate of 0.8081 ±0.0001 cGy/Mu was measured by the ionization chamber. We replaced the ionization chamber with strips (5 in × 1 in) of RCF, in successive exposures we scanned through doses of 2.5, 5, 10, 20, 40, 80, and 160 Gy. After waiting >48 hours for the film darkness to stabilize, the film was scanned with

an EPSON V850 Pro flatbed scanner in gray scale with 600 dpi resolution. A plastic frame was used to press the film flat against the scanner bed. For each strip of film, the signal from a 1000 $\times$ 250 pixel^2 region was analyzed. The exposure was spatially uniform over the analyze region, with an average deviation of 1.6%. Optical density was calculated as described above, and we fit the dose as a function of OD using the same functional form as Bin *et al.*,

$$\text{Dose}(\text{OD}) = 136.0 \cdot \text{OD} + 1344 \cdot \text{OD}^{3.383}. \tag{3.2}$$

The calibration results and the fit are plotted together in Figure 3.3.

Equations (3.1) and (3.2) can be used to extract quantitative dose information from RCF. However, these calibrations were made using film from a single batch. Batch-to-batch variations in the sensitivity and thickness of the active layer give rise to a 20-30% absolute error in determining proton number [111]. In addition, RCF is less sensitive than other ion detectors such as CR-39, a plastic nuclear track detector. While stacks of RCF can provide both spectral and spatial information about the accelerated proton beam, precise quantitative measurements should be cross-calibrated during the experiments. Thomson parabola ion spectrometers can provide higher spectral resolution and the ability to measure other ion species [112]. CR-39 is better suited for measurements of low ion fluxes, such as the highest energy part of a laser-driven ion beam.

3.3 Proton spectrum reconstruction

In laser-driven proton acceleration experiments, RCF stacks are used to make spectral and spatial measurements of the proton beam. This type of detection is possible because of the Bragg peak of ion stopping power. When passing through a material, ions will lose energy through electronic and nuclear interactions with the atoms in the material, typically dominated by electronic Coulomb interactions with electrons. As it penetrates, an ion will

gradually lose energy until a particular depth at which the majority of the remaining energy is deposited. This peak in the energy deposition is referred to as the Bragg peak, and the precise depth depends on the initial ion kinetic energy, ion atomic number and atomic mass, and the material composition. In a typical RCF stack, pieces of film are interleaved with filters (often aluminum foils) so that the active layers are located at the correct depths to evenly sample the full energy range of interest. A description of RCF stacks designs used for experiments presented in this thesis is found in Appendix C

In order to reconstruct the proton energy spectrum (i.e., dN/dE, proton number as a function of energy), response functions must calculated for each piece of RCF relating the deposited energy per proton in the active layer to the initial proton energy. The response functions were generated using 1D particle tracking, neglecting scattering or multidimensional effects, such as beam divergence. A flat proton spectrum, with 1 particle per energy bin, was propagated through a synthetic stack of RCF. The stopping power of materials in the stack ($SP = \mathrm{d}E/\mathrm{d}x$, typically in units of MeV/μm) was interpolated from SRIM-2013 tables [113, 114]. At each spatial step, the energy loss was calculated for each particle as $\mathrm{E}_{\mathrm{deposited}} = SP\Delta x$ and the particle energy was updated. In each active layer, the total energy deposited per particle was measured. Special care was taken to avoid "negative" kinetic energies. The chemical composition and density of the active layer were specified using values found in references [107] and [115].

While the SRIM tables can accurately predict the stopping power and proton ranges, Schollmeier *et al.* demonstrated that the active layer of RCF exhibits reduced response to protons near the Bragg peak, referred to as the Linear energy transfer (LET) effect [116]. Despite the lack of a complete model for the LET effect, Schollmeier *et al.* fit experimental measurements of the effect with the following function,

$$\eta = 1 - 0.4\, e^{-4\exp(-0.2\,SP)}.$$

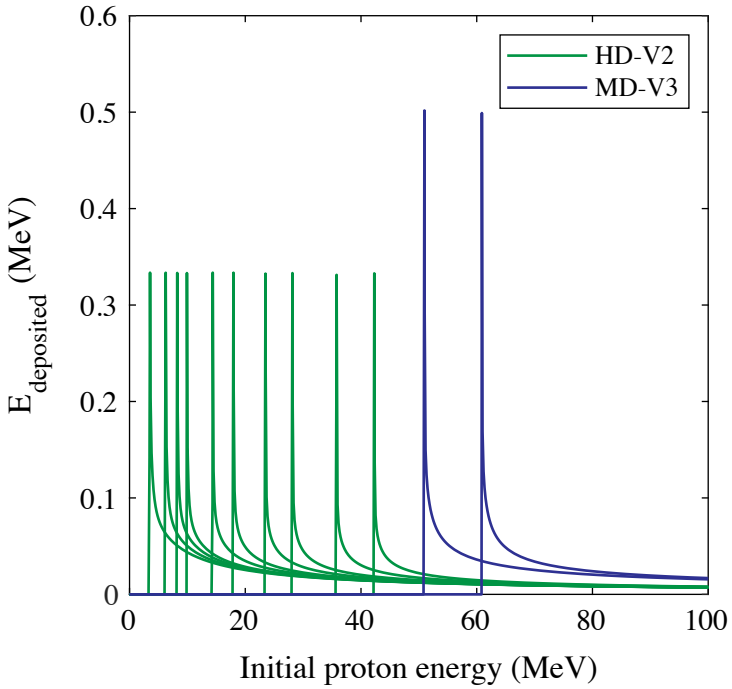

Figure 3.4: Example of the response functions for an RCF stack

To account for this effect, the response calculation was modified to $\mathrm{E}_{\mathrm{deposited}} = \eta SP\Delta x$ when determining the deposited energy in the active layer.

An example of response functions generated for the RCF stack used in Chapter 4 is shown in Figure 3.4. These functions were produced using a 10 nm spatial step, Δx, and a 1 keV energy bin width, ΔE. The front 10 pieces of RCF were HD-V2, while the final two were MD-V3. As discussed in 3.2, MD-V3 film is more sensitive than HD-V2 film. Each film is primarily sensitive to a narrow energy range, corresponding to protons with Bragg peaks located within the active layer.

Experimentally, the total energy deposited in a particular piece of film can be found by integrating signal. First, the dose must be calculated using equations (3.1) and (3.2). Then the dose must be converted from Gy (J/kg) to MeV using the pixel area, active layer depth and density. A simple approach to proton spectrum reconstruction would divide the total deposited energy by the peak of the response function at each layer. Due to the strongly peaked nature of the response and typically exponential laser-driven proton spectra, this

approach can provide reasonable estimates of the proton numbers as a function of energy. However, Schollmeier *et al.* recently demonstrated a more accurate technique for spectrum reconstruction which takes into account the full RCF response function and contributions from higher energy protons [116].

The deposited energy, D, on the i^{th} piece of film can be calculated

$$D_i = \int_{E_i}^{E_n} R_i(E') \frac{\mathrm{d}N(E')}{\mathrm{d}E} \mathrm{d}E' \tag{3.3}$$

where R_i is the response function of the RCF layer, E_i is the peak energy detected at that layer, and E_n is the maximum, or cutoff, energy of the spectrum. The energy spectrum is broken into linear segments between the RCF layers in the stacks,

$$\frac{\mathrm{d}N(E)}{\mathrm{d}E} = \sum_{i}^{n-1} m_{i,i+1}(E - E_i) + \Delta N_i \quad \in \quad E_i < E < E_{i+1} \tag{3.4}$$

where E_i the peak energy at the i^{th} layer, ΔN_i is the proton number at energy E_i, and $m_{i,i+1}$ is the slope of the linear section, described by

$$m_{i,i+1} = \frac{\Delta N_{i+1} - \Delta N_i}{E_{i+1} - E_i}. \tag{3.5}$$

Using equation (3.4), equation (3.3) can be rewritten

$$\begin{aligned} D_i = & \int_{E_i}^{E_{i+1}} R_i(E') \big[m_{i,i+1}(E' - E_i) + \Delta N_i \big] \mathrm{d}E' \\ & + \sum_{j=i+1}^{n-1} \int_{E_j}^{E_{j+1}} R_i(E') \big[m_{j,j+1}(E' - E_j) + \Delta N_j \big] \mathrm{d}E' \end{aligned} \tag{3.6}$$

The summation on the right hand side of equation (3.6) represents the energy deposited at the i^{th} layer by the higher energy portions of the spectrum. Following the notation from Schollmeier *et al.*, this will be referred to as D_{rest}. Using equation (3.5) and some algebra,

equation (3.6) goes to

$$\begin{aligned} D_i = & \int_{E_i}^{E_{i+1}} R_i(E')\Delta N_{i+1}\frac{E'-E_i}{E_{i+1}-E_i}\mathrm{d}E' \\ & + \int_{E_i}^{E_{i+1}} R_i(E')\Delta N_i\big[1-\frac{E'-E_i}{E_{i+1}-E_i}\big]\mathrm{d}E' \\ & + D_{rest} \end{aligned} \tag{3.7}$$

From the experimental results, D_i is a known quantity. Therefore, equation (3.7) can be solved for ΔN_i as a function of D_i, ΔN_{i+1}, and D_{rest},

$$\Delta N_i = \frac{D_i - D_{rest} - \Delta N_{i+1}\int_{E_i}^{E_{i+1}} R_i(E')\frac{E'-E_i}{E_{i+1}-E_i}\mathrm{d}E'}{\int_{E_i}^{E_{i+1}} R_i(E')\big[1-\frac{E'-E_i}{E_{i+1}-E_i}\big]\mathrm{d}E'} \tag{3.8}$$

Fundamentally, there are two integral forms present in these equations. To simplify the expression, the integrals will be represented

$$\Psi_{l,m} = \int_{E_m}^{E_{m+1}} R_l(E')\frac{E'-E_m}{E_{m+1}-E_m}\mathrm{d}E', \tag{3.9}$$

$$\Phi_{l,m} = \int_{E_m}^{E_{m+1}} R_l(E')\big[1-\frac{E'-E_m}{E_{m+1}-E_m}\big]\mathrm{d}E', \tag{3.10}$$

Finally, a general form of the equation (3.8) can be expressed which is easily implemented into an iterative algorithm,

$$\Delta N_i = \frac{1}{\Phi_{i,i}}\left(D_i - \Delta N_{i+1}\Psi_{i,i} - \sum_{j=i+1}^{n-1}\big[\Delta N_j\Phi_{i,j} + \Delta N_{j+1}\Psi_{i,j}\big]\right). \tag{3.11}$$

It is clear from equation (3.11) that the reconstruction of a particular layer depends on the amount of signal on the higher energy layers. Therefore, the iterative solution must work backward through the stack, beginning at the first layer with no signal. For example, assume that the highest energy protons do not reach the fourth layer of an RCF stack ($D_4 = 0$).

Then the calculation would be,

$$\Delta N_4 = 0$$
$$\Delta N_3 = \frac{1}{\Phi_{3,3}}\big(D_3\big)$$
$$\Delta N_2 = \frac{1}{\Phi_{2,2}}\big(D_2 - \Delta N_3\Psi_{2,2} - \big[\Delta N_3\Phi_{2,3}\big]\big)$$
$$\Delta N_1 = \frac{1}{\Phi_{1,1}}\big(D_1 - \Delta N_2\Psi_{1,1} - \big[\Delta N_2\Phi_{1,2} + \Delta N_3\Psi_{1,2}\big] - \big[\Delta N_3\Phi_{1,3}\big]\big).$$

In some situations, the maximum energy of the proton spectrum exceeds the energy range detected by the stack. While the true maximum energy cannot be determined, the reconstruction method can be amended to artificially impose a maximum energy by adding a synthetic RCF layer to the stack with zero signal. In this work, the energy spacing between the synthetic RCF layer the last layer was set to match the spacing between the last two layers (i.e. $E_{synth} - E_n = E_n - E_{n-1}$). Because of the accelerated spetrum is typically exponential, there are relatively few protons at the highest energies and this assumption does not introduce a large error to the measurement.

To validate this reconstruction approach, test data was produced using equation (3.3) and an input proton spectrum to calculate the deposited energy at each layer of film in the stack ($E_{\text{deposited}}$, or D) shown in Figure 3.4. The input spectrum was described by the following function,

$$\frac{\mathrm{d}N(E)}{\mathrm{d}E} = \frac{N_0}{E}e^{-E/kT} \quad (E < E_{\text{cutoff}}),$$

where N_0 was set to 10^{13}, the temperature (kT) was 15 MeV and the cutoff energy (E_{cutoff}) was 65 MeV. The input spectrum and the resulting deposited energy distribution are plotted in black in Figure 3.5. The reconstruction method was used to calculate initial values for ΔN at each layer. The quality of the results can be checked by comparing $E_{\text{deposited}}$ calculated using the input spectrum and equation (3.3) with $E_{\text{deposited},r}$ calculated using equation (3.6) and the reconstructed values for ΔN. After the initial calculation using the reconstruction

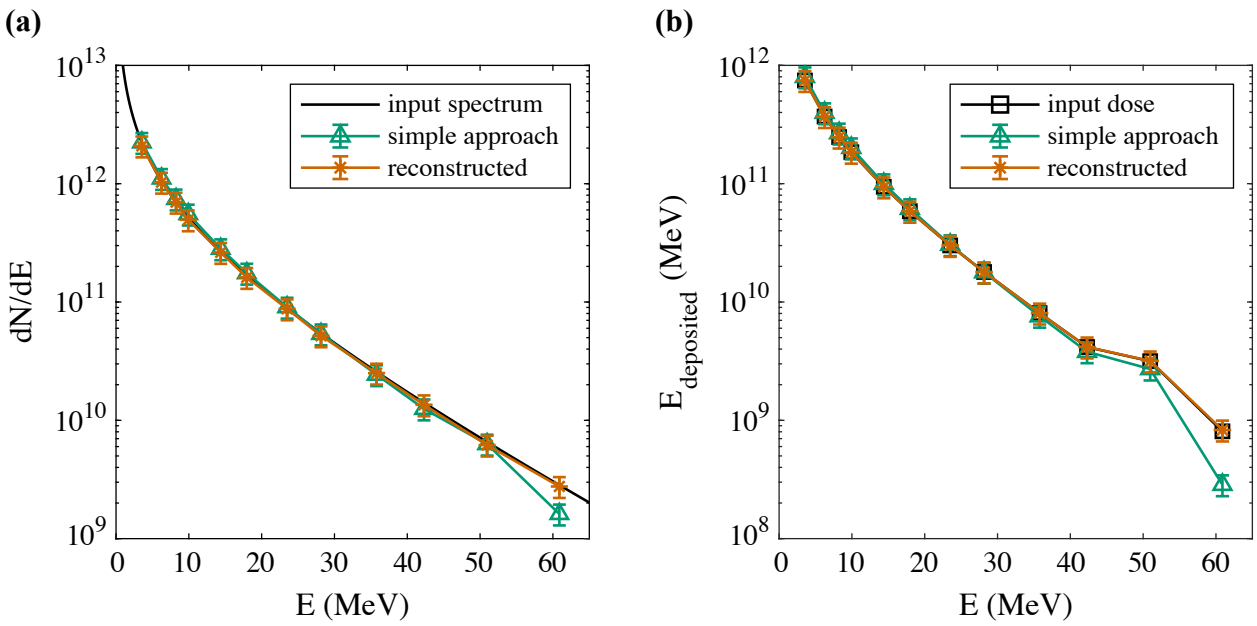

Figure 3.5: Test data was used to validate spectrum reconstruction methods. (a) The input spectrum is compared with the results from the simple approach and a full reconstruction. (b) Calculations of the energy deposited at each RCF layer using the spectra in (a) are compared.

method, a least-squares optimization was used to adjust the values for ΔN in order to improve the agreement between $E_{\text{deposited}}$ and $E_{\text{deposited},r}$. The optimization was based on the built-in MATLAB function **fminsearch**.

The results from the full reconstruction approach described above are compared to the test data in Figure 3.5 (orange stars). For comparison, the results obtained using the simple approach (dividing $E_{\text{deposited}}$ by the peak of the response function) are also plotted (green triangles). The error bars are not related to the reconstruction, but instead represent the 20-30% absolute error in RCF measurements due to batch-to-batch variations in the sensitivity of the film [111]. In general, both methods exhibit reasonable agreement with the input spectrum. The full reconstruction performs much better for the higher energy part of the spectrum.

Due to limitations imposed by the relatively low sensitivity and errors due to variations in sensitivity, other detectors, like CR39, or different spectrometer designs, such as

Thomson parabolas, are better suited to high precision measurements of the proton energy spectrum. In addition, Thomson parabola spectrometers can simultaneously measure multiple ion species. However, even using the simplest approach, RCF spectrometry can provide a reasonable measurement of the proton energy spectrum while simultaneously recording spatial information. This facilitates studies such as the work presented in Chapter 4, where the beam quality and spatial uniformity was measured as a function of energy.

3.4 Quantitative proton radiography inversion

Charged particle radiography, or deflectometry, is a technique used to diagnose electric and magnetic fields in the HED plasmas. In typical HED experiments, a secondary laser pulse accelerates a beam of protons or electrons [9,48,49]. As the beam passes through the principal interaction, the particle trajectories will be altered by the electric and magnetic fields present in the plasma. These deflections are measured by stacks of film or scintillating screens.

Many experiments have relied on proton deflectometry to measure and identify HED electromagnetic phenomena such as laser-driven magnetic field generation [8, 10], Weibel-type filamentation and magnetic self-organization [61, 62],high power laser channeling [60], and nanosecond (non-relativistic) laboratory magnetic reconnection [25, 34, 36, 63]. One approach for producing energetic protons involves using many laser beams to implode a capsule containing D-^{3}He fuel. Fusion of the fuel results in a quasi-monoenergetic, spatially uniform source of 14.7 Mev protons.

All of the experiments presented in this thesis used another approach where secondary high intensity laser pulse accelerates a proton beam to multi-MeV energies via the Target Normal Sheath Acceleration (TNSA) mechanism [50–53, 117]. The broad spectrum of accelerated proton energies leads to a temporal dispersion during transit from the source to the main interaction, with higher energy protons arriving earlier than lower energies. The Bragg peak behavior of ion stopping means that each energy penetrates to a unique depth

in the detector, thus a stack of radiochromic film can capture a time series of images of the electromagnetic field dynamics in a single shot [48].

Proton images are often used as a qualitative diagnostic. Features in the image are compared to simulation or simple models and synthetic radiographs. However, quantitative measurements of path integrated electric and magnetic fields can be extracted from the relative deflections of protons in the image. What follows is largely drawn from the work of Kugland *et al.* [118], including much of the notation. After introducing the basic concepts governing proton imaging, we derive an expression which can be solved numerically and implement algorithms to invert proton images and extract quantitative electric or magnetic field information. In addition to a full 2D Cartesian coordinates solution, we develop a 1D polar coordinates (quasi-2D) solution for azimuthally symmetric systems.

3.4.1 Basic imaging concepts

Proton radiography experiments generally operate in a point-projection geometry. A schematic of a typical experiment is shown in Figure 3.6. A source of protons, whether a broadband source accelerated via the TNSA mechanism or a monoenergetic source generated by D-^{3}He fusion, is located a distance l from the main interaction. The detector, often a stack of radiochromic film (RCF) or a piece of CR-39, is positioned a distance L behind the main interaction. In most experiments, $L \gg l$ and $l \gg a$, where a is the characteristic spatial scale of the field structure being diagnosed.

The mapping between the undisturbed proton beam distribution, $I_0(x_0, y_0)$, and the distribution at image plane, $I(x, y)$, is determined by

$$I(x, y) = \frac{I_0(x_0, y_0)}{|\frac{\partial(x,y)}{\partial(x_0,y_0)}|}. \tag{3.12}$$

where $|\partial(x, y)/\partial(x_0, y_0)|$ is the absolute value of the determinant of the Jacobian matrix relating the object and image planes.

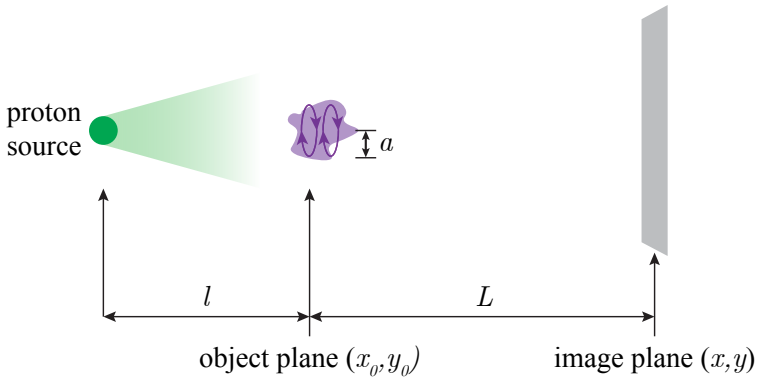

Figure 3.6: Schematic representation of a typical point-projection proton radiography experiment

As the particles pass through the main interaction, the trajectories will be deflected by the electric and magnetic fields. The deflections, α_x and α_y, for a proton traveling with velocity v_z in the $-\hat{z}$ direction can be related to the electric or magnetic fields by

$$\alpha_x = \frac{\Delta p_x}{p_z} = \frac{q}{m_p v_z}\int B_y \mathrm{d}z \quad \text{or} \quad = \frac{q}{m_p v_z^2}\int E_x \mathrm{d}z \tag{3.13}$$

$$\alpha_y = \frac{\Delta p_y}{p_z} = -\frac{q}{m_p v_z}\int B_x \mathrm{d}z \quad \text{or} \quad = \frac{q}{m_p v_z^2}\int E_y \mathrm{d}z. \tag{3.14}$$

The image coordinates can be related to the object plane coordinate as

$$x = x_0 + \frac{L}{l}x_0 + \alpha_x L \tag{3.15}$$

$$y = y_0 + \frac{L}{l}y_0 + \alpha_y L \tag{3.16}$$

where $\tan\alpha \approx \alpha$. If L or $\boldsymbol{\alpha}$ are large, the relationships the image and object coordinates become nonlinear, indeed for very large $\boldsymbol{\alpha}$ proton trajectories can begin to cross and form strong caustics in the image. In the caustic, or proton-crossing, regime, the relationship between I and I_0 is no longer unique and the radiograph cannot be inverted.

Here it is useful to introduce a dimensionless parameter which characterizes the nonlin-

earity of the mapping,

$$\mu \equiv l\alpha/a \tag{3.17}$$

When $\mu \ll 1$, then the mapping is approximately linear and equations (3.15) and (3.16) can be simplified to $x = (1+L/l)x_0$ and $y = (1+L/l)y_0$. As $\mu \to 1$, the mapping is nonlinear and the full expressions must be used. In this case, special care must be taken when generating the proton distribution at the image plane, I. When calculated according to equation (3.12), I is function of the object plane coordinates, (x_0, y_0). In order to produce the correct proton distribution at the image plane, I must be interpolated on to (x, y) calculated according to equations (3.15) and (3.16). If $\mu > 1$, caustics form in the image. We limit the following discussion to situations where $\mu < 1$, where the relationship between I and I_0 is unique and can be inverted.

Using equations (3.15) and (3.16), we can derive equation (7) of Kugland *et al.* [118],

$$\Big|\frac{\partial(x,y)}{\partial(x_0,y_0)}\Big| = \Big|\Big(1+\frac{L}{l}+\frac{\partial\alpha_x}{\partial x_0}L\Big)\Big(1+\frac{L}{l}+\frac{\partial\alpha_y}{\partial y_0}L\Big) - L^2\frac{\partial\alpha_x}{\partial y_0}\frac{\partial\alpha_y}{\partial x_0}\Big|.$$

Note: simple rotations of proton trajectories will not create intensity modulations in the proton image. Therefore, measurable deflections can be considered irrotational, $\nabla \times \boldsymbol{\alpha} = 0$, and the deflections can be related to a scalar deflection potential

$$\boldsymbol{\alpha} = \nabla\Phi.$$

Noting that $(1 + L/l) = M$, the magnification, and introducing the normalizations $\tilde{x} = x_0M/w_x$, $\tilde{y} = y_0M/w_y$, $\tilde{\alpha}_i = \alpha_iL/w_i$, and $\tilde{\boldsymbol{\alpha}} = \tilde{\nabla}\tilde{\Phi}$, where w_i is the full beam width at the detector, we can rewrite equation (7) of Kugland *et al.* [118], as

$$\frac{1}{M^2}\Big|\frac{\partial(x,y)}{\partial(x_0,y_0)}\Big| = \Big|1+\tilde{\nabla}^2\tilde{\Phi}+\frac{\partial^2\tilde{\Phi}}{\partial\tilde{x}^2}\frac{\partial^2\tilde{\Phi}}{\partial\tilde{y}^2} - \Big(\frac{\partial^2\tilde{\Phi}}{\partial\tilde{x}\partial\tilde{y}}\Big)^2\Big|. \tag{3.18}$$

Combining equations (3.12) and (3.18), and normalizing the undisturbed beam as $\tilde{I}_0 =$

I_0/M^2, we finally derive the following expression that can be solved numerically,

$$\tilde{\nabla}^2\tilde{\Phi} = \frac{\tilde{I}_0 + \epsilon}{I + \epsilon} - 1 - \frac{\partial^2\tilde{\Phi}}{\partial\tilde{x}^2}\frac{\partial^2\tilde{\Phi}}{\partial\tilde{y}^2} + \Big(\frac{\partial^2\tilde{\Phi}}{\partial\tilde{x}\partial\tilde{y}}\Big)^2, \tag{3.19}$$

where ϵ is a small number to help prevent singularities in regions of large intensity modulation.

3.4.2 2D Cartesian coordinates

We developed a MATLAB routine to solve equation (3.19) iteratively using a five-point stencil Poisson solver and breaking the equation into parts, first solving the linear portion before including the nonlinear terms. A sketch of the code is shown in Algorithm 1 in Appendix B.

In order to validate the code, we use the standard "ellipsoidal blob" test field. From equation (93) of Kugland *et al.*, an azimuthal magnetic field profile is given

$$B_\theta = B_0\frac{r_0}{a}\exp\Big(-\frac{r_0^2}{a^2} - \frac{z_0^2}{b^2}\Big),$$

where $r_0 = \sqrt{x_0^2 + y_0^2}$, and a, b are constants parameterizing the spatial extent of the field. According to equations (3.13) and (3.14), this field yields simple expressions for the deflections

$$\alpha_x = -\frac{q}{m_p v_z}B_0\frac{\sqrt{\pi}b}{a}r_0\exp\Big(-\frac{r_0^2}{a^2}\Big)\sin\theta,$$

$$\alpha_y = \frac{q}{m_p v_z}B_0\frac{\sqrt{\pi}b}{a}r_0\exp\Big(-\frac{r_0^2}{a^2}\Big)\cos\theta.$$

Using these deflections, we can compute the Jacobian according to equation (7) of Kugland *et al.*, and generate the proton image with equation (3.12).

For the following examples, we set $l = 6$ mm, $L = 80$ mm, and the proton kinetic energy, $KE_p = 30$ MeV, typical of experiments using a TNSA proton source. The peak

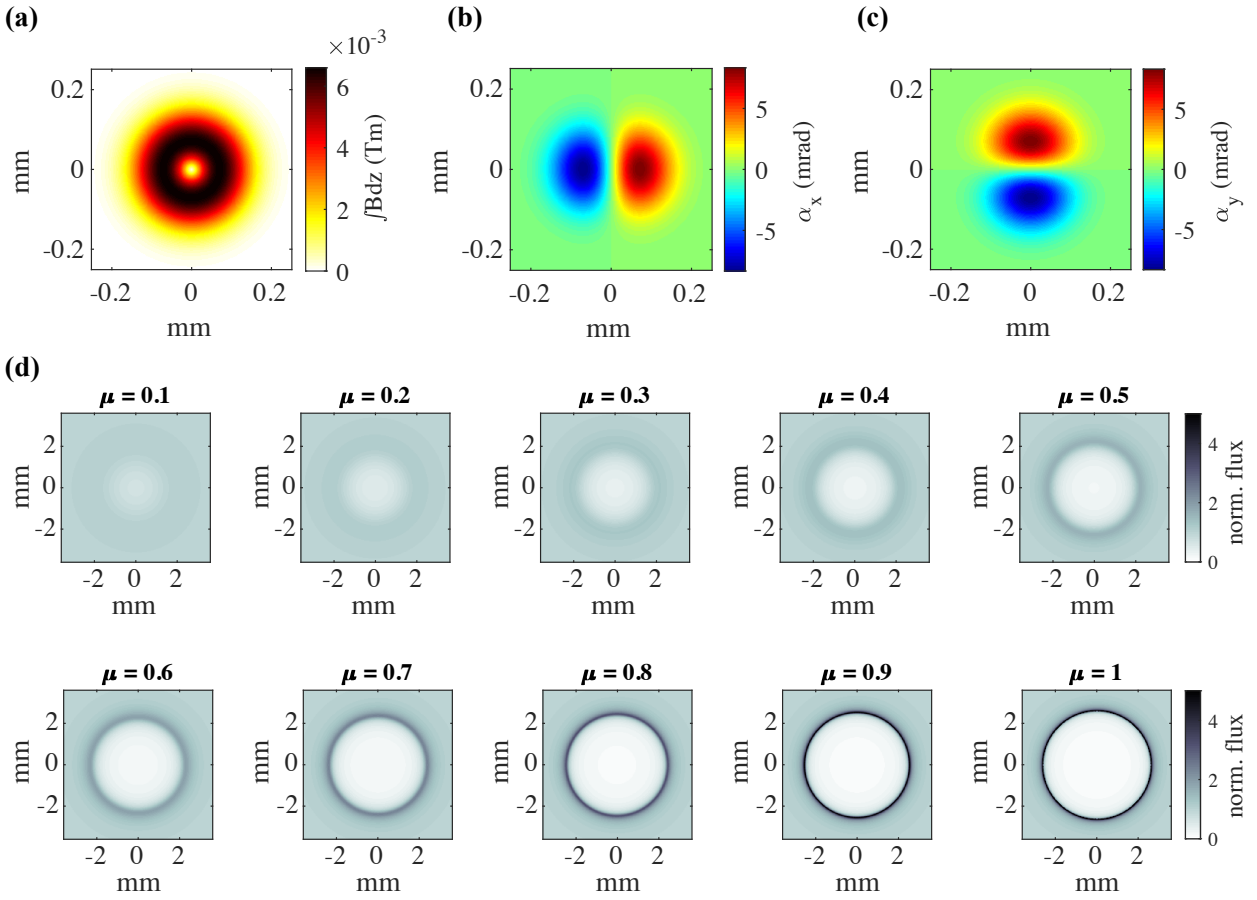

Figure 3.7: (a) Example path integrated magnetic field profile for $\mu = 0.5$ and the corresponding deflections α_x (b) and α_y (c). Synthetic proton images for $\mu = 0.1$ to 1 are compared in panel (d)

magnetic field was gradually increased such that μ ranged from 0.1 to 1. The spatial scale of the field was held constant at $a = 100$ μm and $b = 10$ a. An example of the path integrated magnetic field profile is shown in Figure 3.7(a). This profile corresponds to $\mu = 0.5$, and the deflections α_x and α_y are shown in 3.7(b) and (c) respectively. For each value of μ, synthetic images generated using equation (3.12) are compared in Figure 3.7(d). For simplicity, the initial undisturbed proton distribution is perfectly uniform. As μ increases, the proton accumulation in a ring pattern becomes stronger and stronger. When $\mu \geq 1$, the trajectories of protons begin to cross, and equation (3.12) is no longer valid.

The proton images shown in Figure 3.7(d) were used to test the inversion algorithm. For

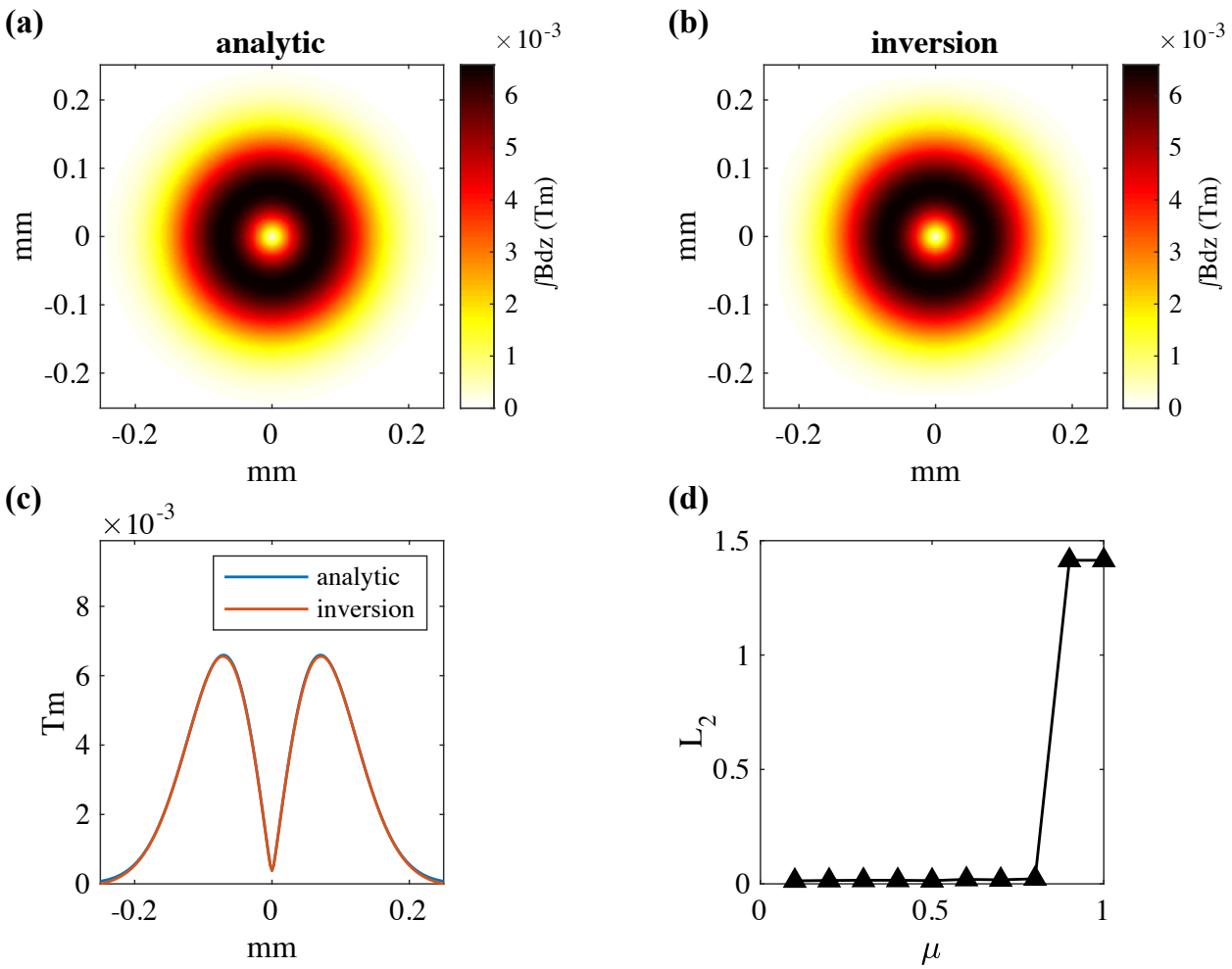

Figure 3.8: Panel (a) shows the analytic path integrated field for $\mu = 0.5$ (same as Figure 3.7), while (b) shows the field calculated by the inversion code. Line-outs through the fields are compared in panel (c). The L_2 norm comparison between the analytic and inverted field is plotted as a function of μ in (d).

each value of μ, the images were inverted to retrieve normalized deflection potential and spatial coordinates ($\tilde{\Phi}$, $\tilde{x}$, $\tilde{y}$). The deflections, α_x and α_y, were calculated according to the normalizations described in section 3.4.1. Finally, the path integrated fields were found using equations (3.13) and (3.14).

To assess the accuracy of the inversion as a function of μ, the results were compared to

the analytic field profile using the L_2 norm,

$$L_2 \equiv \sqrt{\frac{\sum_x \sum_y (B_{calculated} - B_{analytic})^2}{\sum_x \sum_y (B_{analytic})^2}}$$

a metric similar to that used by Graziani *et al* [119]. The L_2 norm was calculated independently for the x and y components of the fields and the results were added in quadrature, $L_2 = \sqrt{L_{2,x}^2 + L_{2,y}^2}$. Figure 3.8 (a-c) shows an example comparison between the analytic field profile and the inversion results for $\mu = 0.5$. The complete results of the scan of μ are summarized by Figure 3.8(d), which shows L_2 as a function of μ. In general, there is excellent agreement between the inversion results and the analytic field for $\mu < 0.9$. However, the inversion fails completely for $\mu \geq 0.9$.

From these results, we conclude that this 2D Jacobian inversion method is a robust approach to proton image inversion for small to moderate degrees of nonlinearity. It possible that the functionally could be extended to $0.9 \leq \mu < 1$ by using a finer grid in order to better resolve the small spatial scales of high flux features. Other approaches for nonlinear images can potentially solve the inversion problem for larger values of μ and more complex field geometries. In particular, a number of methods have been developed base reframing the inversion as a Monge transport problem [119–121] based on minimizing the total distance traveled by a particle as it is transported from the source to the detector. However, these approaches can be slow, taking anywhere from 1 to 3 hours to analyze a single 201×201 pixel image [120, 121]. Using the same image size in this test, the complete analysis of all 10 images only took 58 seconds. Therefore, the MATLAB routine described here is considerably faster and while maintaining high accuracy for $\mu < 0.9$.

3.4.3 1D polar coordinates

While the full 2D Cartesian Jacobian method described above is very fast for small images, experimental images can often be quite large. For example, a 6×6 cm^2 piece of RCF

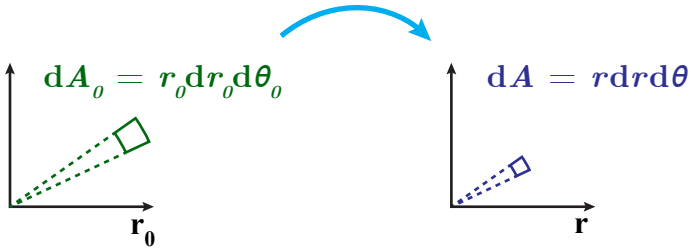

Figure 3.9: Conceptual schematic of the mapping in polar coordinates between the object plane (r_0,θ_0) and image plane (r,θ)

(typical of OMEGA EP experiments) scanned with 600 dpi resolution yields approximately 1400×1400 pixel images. While the images are usually cropped before analysis, the analysis can be slow, especially considering the RCF stack often contains 10-20 pieces of film. In many cases, the symmetry of the experiment can be leveraged to simplify the analysis. For example, magnetic fields generated by a single nanosecond laser pulse are approximately azimuthally symmetric. Therefore, the full field can be described by the 1D radial profile.

In order to take advantage of this symmetry, the basic mapping equations described in section 3.4.1 must be converted to polar coordinates. Equations (3.15) and (3.16) are now

$$r = r_0 + \frac{L}{l} r_0 + \alpha_r L \tag{3.20}$$

$$\theta = \theta_0 + \alpha_\theta \tag{3.21}$$

and the Jacobian matrix is

$$\frac{\partial(r,\theta)}{\partial(r_0,\theta_0)} = \begin{bmatrix} \frac{\partial r}{\partial r_0} & \frac{\partial r}{r_0 \partial \theta_0} \\ \frac{r \partial \theta}{\partial r_0} & \frac{r \partial \theta}{r_0 \partial \theta_0} \end{bmatrix}.$$

Based on the azimuthal symmetry, we assume that $\partial\theta_0 = \alpha_\theta = 0$. We can simplify the determinant of the polar Jacobian to

$$\left| \frac{\partial(r,\theta)}{\partial(r_0,\theta_0)} \right| = \frac{r}{r_0} \left(1 + \frac{L}{l} + \frac{\partial \alpha_r}{\partial r_0} L \right) \tag{3.22}$$

Combining equations (3.12) and (3.22), we can derive and expression that can be directly

integrated to solve for α_r,

$$\alpha_r = \int \frac{M}{L}\left[\frac{r_0}{Mr}\left(\frac{J_0}{J}\right) - 1\right]\mathrm{d}r \tag{3.23}$$

where we have replaced I,I_0 with J,J_0 to signify 1D profiles rather than 2D images, and we use $M = 1 + L/l$.

Implementation of this method for the work described in thesis (see Chapter 5) has focused on magnetic field measurements. If we denote the path integrated magnetic field as $\mathcal{B}_\theta = \int B_\theta \mathrm{d}z$, equation (3.23) can be rewritten:

$$\mathcal{B}_\theta = \frac{1}{\nu_B}\int \left[\frac{r_0}{\tilde{r}}\left(\frac{J_0}{J}\right) - 1\right]\mathrm{d}r \tag{3.24}$$

where $\nu_B = Le/Mm_p v_z$ and $\tilde{r} = Mr$. This integral is complicated by the fact that $\tilde{r}$ is a function of $\mathcal{B}_\theta$:

$$\tilde{r} = r_0 + \nu_B \mathcal{B}_\theta$$

Therefore the integral must be solved numerically, updating $\tilde{r}$ at each step. This was accomplished using a 4th order Runge-Kutta method. The details of the implementation are sketched in Algorithm 2 found in Appendix B. It should be noted that the present implementation assumes $\mathcal{B}_\theta(r = 0) = 0$, which is typically valid for laser-driven field profiles (see for example [8–10]).

To test this method, we return to the field profiles and proton images described above. Instead of the full image, we take a line-outs of the radial proton flux profile for analysis. A summary of the results is shown in Figure 3.10. Again, we find excellent agreement between the inverted and analytic field profiles. This method performs reasonably well all the way up to $\mu = 1$. The comparison between the inverted and analytic fields for $\mu = 1$ is shown in Figure 3.10(b). Despite the strong nonlinearity, this method accurately predicts the peak path-integrated field strength. In addition, the complete analysis of all 10 images (including reading image from file and plotting results) took 10.3 seconds. Therefore, in configurations with azimuthal symmetry, this method can be extremely useful, even in the case of strong

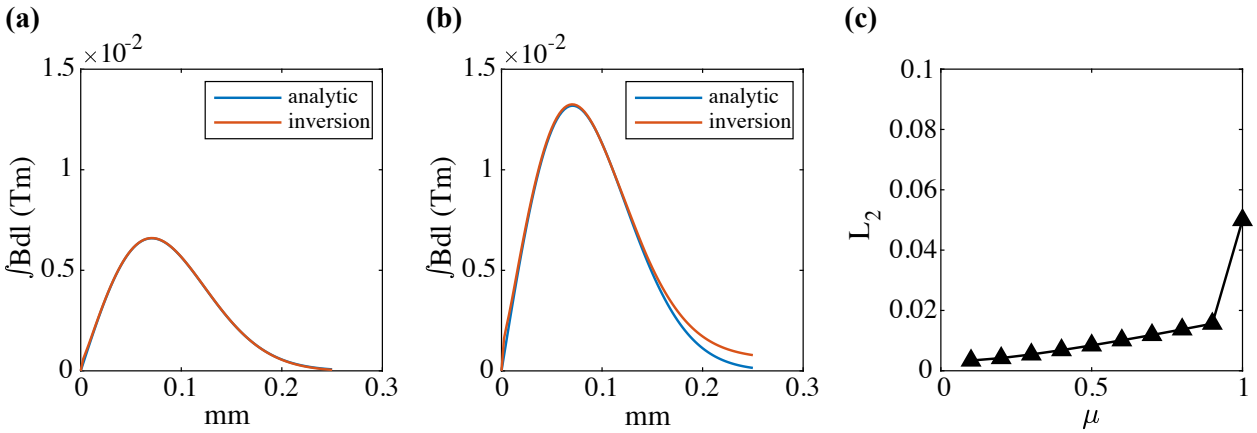

Figure 3.10: (a-b) Comparison of inverted azimuthal field profile with the true analytic field for (a) $\mu = 0.5$ and (b) $\mu = 1$. Again, the L_2 norm comparison between the analytic and inverted field is plotted as a function of μ in (c) (note: vertical axis has a much smaller range than Figure 3.7(d)).

fields.

3.4.4 Forward scattering

If the fields are too strong for the inversion methods described above, a forward scattering method involving particle tracking through assumed field profiles can be used to attempt to match features in the proton image. For example, the magnetic fields generated by high intensity laser pulses can be extremely strong, with peak field strengths on the order 100 MG (see Chapter 5 for a further discussion). For such fields with typical proton energies and imaging parameters, $\mu > 1$ and the Jacobian inversion relationship breaks down.

Instead, investigations of strong fields have relied on a combination simulation, simple expressions and particle tracking to reproduce features observed experimentally [9, 10, 69]. While previous work has used full 3D particle tracking, the method described here takes advantage of the fact that the longitudinal extent of the field (i.e. l_z) is much smaller than L, the distance to the detector. Even when $\mu > 1$ and caustics form in the image, individual particles only undergo comparably small transverse motions while passing through the plasma. Therefore, the full particle trajectory through the field can be approximated

by a single push from the path-integrated fields, reducing the number of calculations from $N_p \times N_{z\ \text{steps}}$ to N_p.

What follows is a brief description of the workflow for this approach. First, we choose either a simulated field or a functional form for the field profile (often similar to the "ellipsoidal blob" above). Then we initialized particles with random positions at the object plane. Initial propagation angles are determined by the trajectory from a point source to the particle's position at the object plane. Using equations (3.13) and (3.14), we calculate the deflection for each particle due to the path-integrated field and update the particle angle. Image plane positions are calculated using the updated angles and synthetic images are produced by making a 2D histogram of the final particle positions.

Figure 3.11 compares synthetic proton images generated by the equation (3.12) (Jacobian method) and by this simplified particle tracking method. We observe good agreement for $\mu = 0.4$. However, when $\mu = 4$ proton trajectories cross and equation (3.12) is invalid, leading to pixelated results with extreme intensity values (as shown in figure 3.11(d)). Crossing particle trajectories gives rise to the diffuse signal surrounding the strong caustic ring feature in Figure 3.11(e).

The forward scattering particle approach is limited because it requires a advanced determination of the field profile, whether through simulation or guessing a functional form. While it is possible to develop an iterative algorithm based on forward scattering, this method typically lends itself to guess-and-check approach where parameters such as field strength or radial extent are manually varied until features in the synthetic image resemble experimental data. Reasonable guesses or staring points may be obtained using numerical modeling of the laser-plasma interactions.

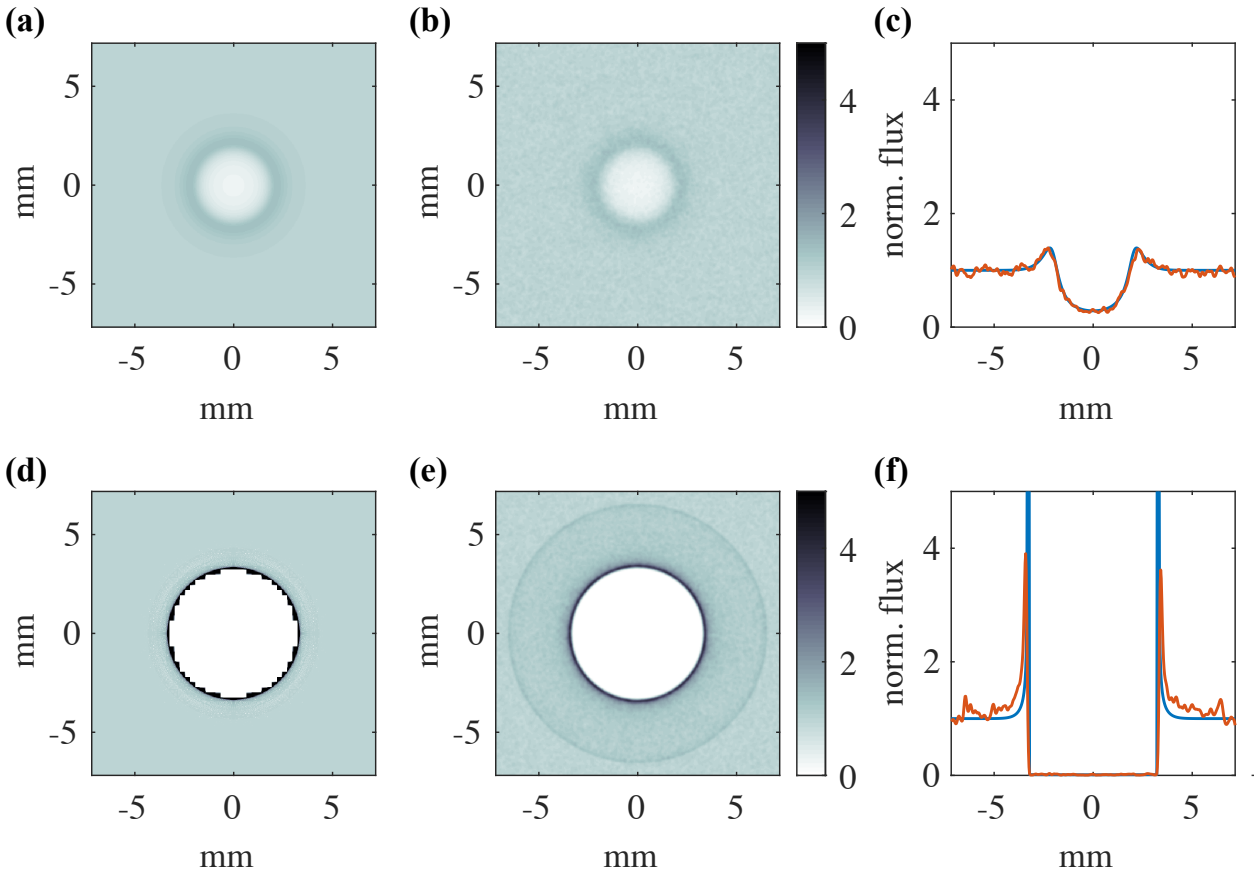

Figure 3.11: The particle method for generating synthetic proton images is compared with the Jacobian method for $\mu = 0.4$ (a-c) and 4 (d-f). The first column shows synthetic images calculated with equation (3.12), while the second shows 2D histograms of the particle positions. The third column compares line-outs through the image, with the Jacobian plotted in blue and the particle method in orange.

3.5 Particle-in-cell (PIC) simulations

Numerical simulations aide interpretation of experimental results and enable further exploration of underlying physics. In principle, the behavior of a plasma can be completely described by combining the Lorentz force ($\frac{\mathrm{d}\vec{p}}{\mathrm{d}t} = \frac{q}{m}(\vec{E} + \vec{v} \times \vec{B})$) with Maxwell's equations. However, simulating a system of many particles in a 3D volume can be extremely computationally expensive. The particle-in-cell (PIC) method [122] takes advantage of the charge-to-mass ratio dependence of the Lorentz force to represent collections of particles by a single macroparticle. For each time step, the full particle position and momentum of the macropar-

ticles are tracked while the fields are solved on a grid. The PIC calculation is broken into four steps. First, the gridded field values are interpolated to the macroparticle positions. Then, particle positions and momenta are advanced according to the Lorentz force. Next, currents and charge densities based on new macroparticle positions and momenta are interpolated back onto the grid. Finally, the fields are updated by solving Maxwell's equations.

The grid size (Δx) must be chosen so that relevant length scales are resolved, such as the laser wavelength or the Debye length. For numerical stability, the time step must obey the Courant-Friedrichs-Lewy (CFL) condition ($\Delta t^2 < \frac{1}{\Delta x^2} + \frac{1}{\Delta y^2} + \frac{1}{\Delta z^2}$). Higher fidelity is achieved by using smaller grids and more macroparticles per grid cell (or particles-per-cell (PPC)), but this is limited by increased computational expense.

Throughout this thesis, the PIC code OSIRIS was used to support experimental results. OSIRIS is a state-of-the-art, fully relativistic PIC code developed by the OSIRIS Consortium, consisting of UCLA and IST (Lisbon, Portugal) [123, 124]. The code is 3D3V, meaning it can be run with full 3D Cartesian spatial dimensions and tracks momentum in all directions, though simulations are often in 2DV3 due to computational considerations. In addition, the code can run with 2D axisymmetric cylindrical coordinates and a quasi-3D module based on an azimuthal harmonic expansion was recently implemented [125]. A number of 2D and 3D OSIRIS simulations will be discussed in the following chapters, all of which were run using the Flux high performance computing cluster at the University of Michigan.

CHAPTER 4

Proton Beam Emittance Growth in Multipicosecond Laser-Solid Interactions

High intensity laser-solid interactions can accelerate high energy, low emittance proton beams via the target normal sheath acceleration (TNSA) mechanism. Such beams are useful for a number of applications, including time-resolved proton radiography for basic plasma and high energy density (HED) physics studies. In experiments using the OMEGA EP laser system, we perform the first measurements of TNSA proton beams generated by up to 100 ps, kilojoule-class laser pulses with relativistic intensities. By systematically varying the laser pulse duration, we measure degradation of the accelerated proton beam quality as the pulse length increases. Two dimensional particle-in-cell (PIC) simulations and simple scaling arguments suggest that ion motion during the rise time of the longer pulses leads to extended preformed plasma expansion from the rear target surface and strong filamentary field structures which can deflect ions away from uniform trajectories and therefore lead to large emittance growth. Optimal laser pulse conditions are identified such that this source can be used to diagnose magnetic field generation and interaction dynamics in Chapters 5 and 6.

4.1 Introduction

The interaction of a high intensity laser pulse with thin solid foil targets can produce a burst of high energy ions [50–52] accelerated via the target normal sheath acceleration (TNSA) mechanism [53]. The laser pulse excites a population of hot electrons which stream through the target and establish a strong, electrostatic sheath field on the rear surface. The sheath field can drag protons and other ions out of the contaminant layer on the target surface, accelerating them to energies of many 10s of MeV. The acceleration occurs over time-scales comparable to the laser pulse duration (typically ranging from 100s of fs to 10s of ps). The accelerated beam propagation is nearly laminar [55, 56], emanating from the rear of the target as if from a small, virtual source [57]. These qualities make laser-accelerated ion beams a potentially attractive source for charged particle radiography [57, 126] or fast ignition [105, 127], and could lead to biomedical applications, such as cancer radiotherapy [128], or as a high-current ion injector for conventional accelerators [129] (see also the reviews by Daido *et al.* [81] and Macchi *et al.* [80] and references within).

While improvements to stability, energy, and bandwidth must be made before laser-driven ion beams become a practical source for accelerator or biomedical applications, proton radiography is routinely implemented as a diagnostic tool on high energy, high power laser systems throughout the world. Ultrafast TNSA beams of protons have been instrumental in measuring a number of high energy density (HED) electromagnetic phenomena including laser-driven magnetic field generation [8, 10], Weibel-type filamentation and magnetic self-organization [61, 62], high power laser channeling [60], and laboratory magnetic reconnection [25, 36, 63]. Compared to D^3He fusion, an alternate HED radiography source which produces mono-energetic protons, the ultrafast proton beams provide improved spatial resolution due to the small virtual source [57, 59] and the quasi-Maxwellian energy spectrum can be employed to achieve temporal resolution by allowing for time-of-flight dispersion of protons before reaching the radiography subject. The broad spectrum makes possible single shot, time-resolved measurements of ultrafast dynamics with picosecond temporal resolution

(as shown in references [10] and [60]).

In recent years, there has been a concerted computational and experimental effort to revisit the physics of laser-solid interactions on newly available high-energy laser systems. OMEGA EP, for example, is capable of delivering relativistically intense laser pulses ($I\lambda^2 > 10^{18}$ $Wcm^{-2}\mu m^2$) with kilojoule energies and multipicosecond pulse durations. Simulations suggest that the multipicosecond interaction will heat plasma electrons beyond the ponderomotive potential of the laser [64, 65, 130, 131]. Indeed, recent experimental results have confirmed that these high energy, multipicosecond laser systems accelerate ions to maximum energies beyond those predicted by traditionally cited scaling laws [66–68].

While these results are promising, little attention has been paid to the accelerated beam quality. A spatially uniform, low emittance beam is essential for many potential applications of laser-driven protons. In particular, accurate and reproducible diagnosis of electromagnetic fields requires a uniform beam profile. Additionally, attempts to focus or manipulate the beam would be limited by the transverse emittance. Potential gains in maximum proton energy afforded by multipicosecond laser pulses could be outweighed by degraded beam uniformity.

For example, the long rise time of the kilojoule, multipicosecond pulse can preheat the target, initiating plasma expansion from the rear surface [132]. Early work studying the impact of laser prepulse due to amplified spontaneous emission (ASE) demonstrated that preformed density gradients can suppress the sheath electric field and reduce the maximum accelerated ion energies [133–136]. In addition, expansion of the rear surface can modulate the beam divergence [134, 137] and introduce non-uniform structures into the beam [138].

In this chapter, experiments exploring the impact of laser energy and pulse duration on the accelerated beam quality are presented. The results demonstrate that the proton beam quality is significantly degraded as the laser pulse duration increases. The maximum proton energies agree well with previous results and scalings from kilojoule-class, multipicosecond laser systems, including first published measurements of TNSA driven by 100 ps laser pulses

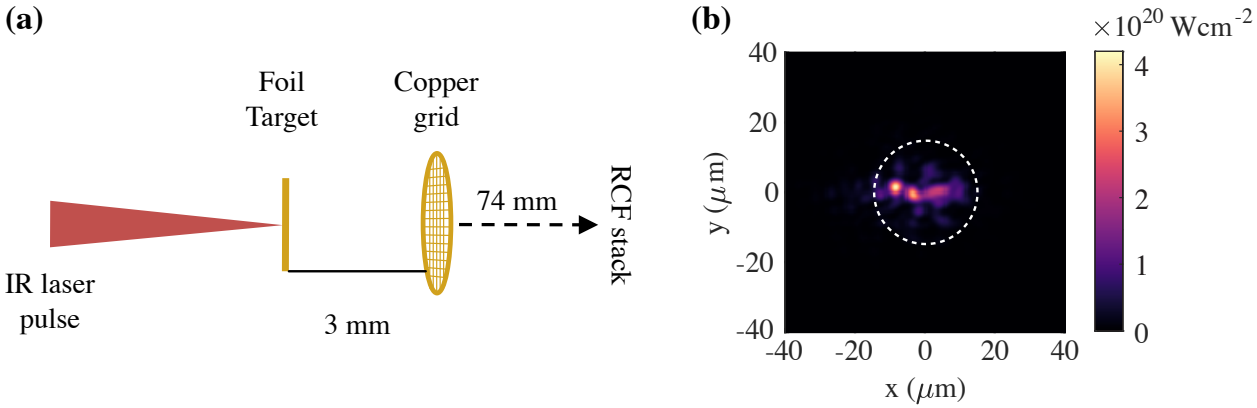

Figure 4.1: (a) Schematic of the experimental setup. Copper grids were mounted 3 mm behind the 2 mm x 2 mm foil targets. The radiochromic film stack was positioned 74 mm behind the grid. (b) An example vacuum focal plane intensity profile measured on-shot for a pulse with 296 J of energy and a 0.7 ps duration. The white circle encloses 80% of the energy.

with relativistic intensities. However, the degraded uniformity at longer pulse durations makes these beams unsuitable for proton radiography. 2D particle-in-cell (PIC) simulations suggest that significant plasma expansion and formation of filamentary magnetic field structures during the rise time of the laser pulse increase the emittance of the proton beam for longer pulse durations. These results should inform the development and implementation of proton radiography diagnostics on existing and future HED facilities.

4.2 Experimental methods

Experiments were performed on the OMEGA EP laser system using two chirped pulse amplified (CPA), infrared (IR) beams. Taking advantage of the flexibility of the OMEGA EP CPA system, laser parameters such as pulse duration and energy were scanned to cover a range of pulse durations (nominally 0.7, 10 and 100 ps). Table 4.1 lists the laser parameters used in the experiment, including on-shot measurements of the pulse duration [139] and energy. The available laser energy depends on the pulse duration and ranged from approximately 150 to 2000 J. Despite $f/1.8$ focusing, the focal spot on target is typically large, with 80%

Table 4.1: A list of the laser parameters used in the experiment. The nominal pulse duration is shown in the first column. On-shot measurements of pulse duration, laser energy, and focal spot r_{80} are shown in columns 2, 3, and 4. Calculated laser power (rounded to nearest 5 TW) and peak intensity are in columns 5 and 6.

Pulse Duration					
Nominal (ps)	Measured (ps)	Energy (J)	r_{80} (μm)	P (TW)	I_0 (Wcm^{-2})
0.7	0.7 ± 0.1	296 ± 7	14.8	420	$4.2 \pm 0.4 \times 10^{20}$
0.7	0.6 ± 0.1	143 ± 4	17.2	240	$1.8 \pm 0.2 \times 10^{20}$
10	11.5 ± 1.2	753 ± 19	14.9	65	$5.6 \pm 0.6 \times 10^{19}$
10	11.1 ± 1.1	376 ± 9	17.1	35	$1.8 \pm 0.2 \times 10^{19}$
100	99.7 ± 10.0	1944 ± 49	15.7	20	$1.5 \pm 0.2 \times 10^{19}$
100	95.4 ± 9.5	1006 ± 25	15.4	10	$9.4 \pm 1.0 \times 10^{18}$

of the laser energy contained in a radius, $r_{80} = 15.9 \pm 0.8$ μm. However, as shown in Figure 4.1(b), on-shot measurements of the laser fluence profile [140] reveal regions with high peak intensity that can be 5 to 10 times greater the r_{80} intensity.

The targets were 2 mm x 2 mm flat copper foils with a thickness of 50 μm, and were shot at normal incidence. In order to assess the beam quality of the accelerated protons, a fine copper grid was placed 3 mm behind the foil target. The grid bars were nominally 25 ± 5 μm thick and the width and grid pitch were 10 μm and 83 μm, respectively. Any non-uniformity in the proton beam would be visually represented by a distortion of the imprinted grid pattern.

The accelerated proton beams were detected with layered stacks of radiochromic film (RCF). Exploiting the Bragg peak in proton stopping range, the film stacks were assembled with interleaved layers of film and aluminum filters to sample particular proton energies across the broad energy spectrum. This spectral information is often converted to time-of-flight between the source and the interaction being probed in order to achieve time-resolved radiography. In this experiment, the successive film layers allowed for direct comparison of the beam quality at different proton energies.

The RCF stacks were composed of Gafchromic^{TM} HD-V2 and MD-V3 film. After exposure, the pieces of film were digitized with an Epson V850 Pro flatbed scanner with 600 dpi

resolution. The raw RCF signal was first converted to optical density ($OD = -\log_{10}$(Exposed Signal/Unexposed Signal)) and then to deposited dose [108, 110] in order to retrieve the proton fluence.

4.3 Experimental results

In successive shots, the laser power was scanned between approximately 10 and 420 TW. The detected proton beams are shown in Figure 4.2 grouped by laser pulse duration. As expected, the maximum observed proton energy increased with laser intensity, exceeding 60 MeV from a 0.7 ps pulse with 296 J of laser energy. The longer pulse duration, higher energy shots resulted in more signal at lower proton energies.

The proton spectra were reconstructed following methods outlined in Schollmeier *et al.* [116]. Proton spectra from the highest intensity shots at each pulse duration are shown in Figure 4.3. RCF spectrometry has relatively low energy resolution compared to other techniques, especially Thomson Parabola spectroscopy used in references [66] and [67]. In addition, RCF is less sensitive to low proton doses than other detectors, such as CR-39, so these measurements likely underestimate the cutoff proton energy. Batch-to-batch variations in the sensitivity of the film give rise to a 20-30% absolute error in determining proton number [111]. The error bars in Figure 4.3 correspond to this absolute error, rather than the relative error between RCF layers.

While protons were accelerated to energies exceeding 20 MeV with the 1944 J, 99.7 ps pulse, the conversion efficiency was considerably lower than the shorter pulse durations. We estimate a $0.46 \pm 0.1\%$ conversion to protons with kinetic energies exceeding 3.5 MeV, compared to $4.7 \pm 1\%$ and $3.4 \pm 0.9\%$ conversion for the 296 J, 0.7 ps pulse and 753 J, 11.5 ps pulse, respectively. The 11.5 ps pulse resulted in the highest overall beam charge, 2.3 ± 0.5 μC, while the 0.7 ps pulse gave 1.4 ± 0.3 μC and the 99.7 ps pulse gave 1.3 ± 0.5 μC. Note that the low energy portions of the beams overfilled the RCF detectors, and the grid

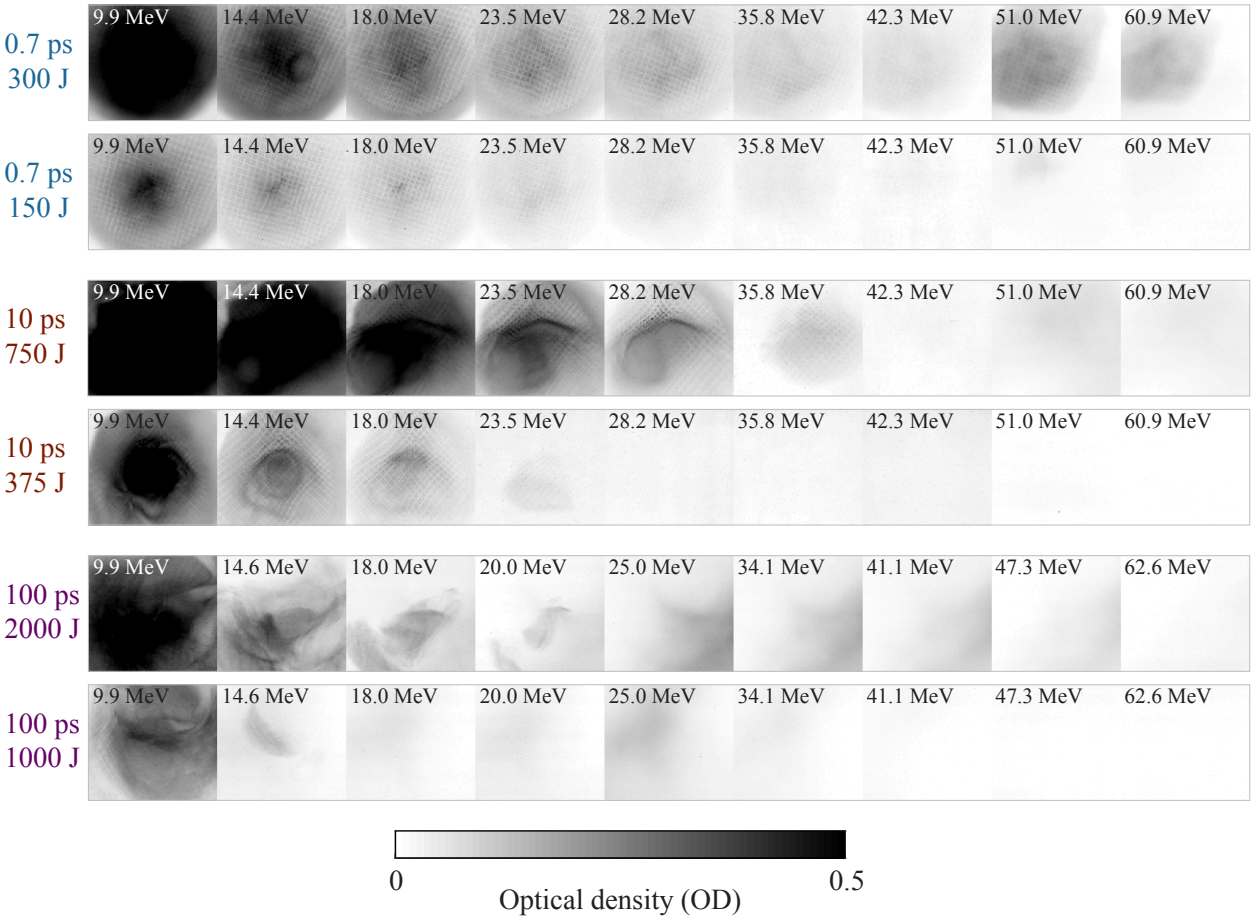

Figure 4.2: Radiochromic film stacks provide a visual comparison of the accelerated proton beam spectra and qualities. The diffuse signal present on later pieces of film, particularly in the nominally 100 ps shots, can likely be attributed to high energy electrons that co-propagate with the proton beam. (It should be noted that a different stack design was used for the 100 ps shots, but comparable penetration depths are shown here). The color scale saturates low energy portions of the beams to emphasize the comparison between higher proton energies.

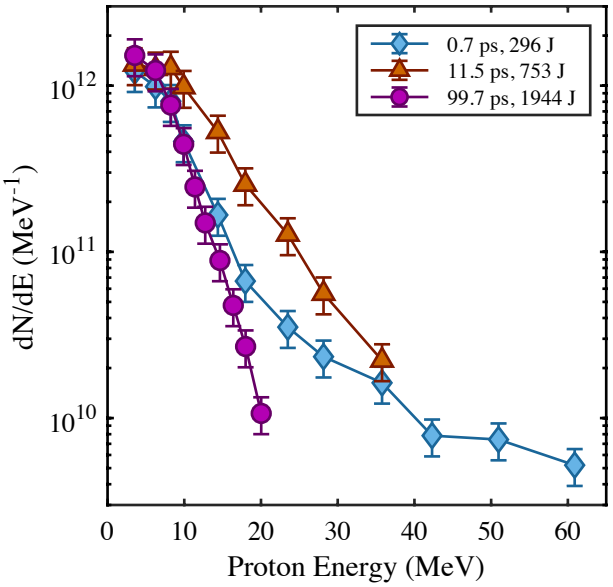

Figure 4.3: Reconstructed proton spectra from the highest intensity shots for each laser pulse duration.

target partially obscured the beams. Therefore, these estimates provide a lower bound on the conversion efficiency and beam charge.

Figure 4.4(a-c) compares representative proton beam profiles for the three pulse durations explored. For clarity, the nominal pulse duration will be used for reference throughout the following discussion. It is immediately evident that the grid pattern is significantly distorted in the 10 ps pulse duration case and completely absent in the 100 ps case. Beyond visual inspection, the 2D Fourier transform of the grid pattern was used to quantify the beam quality across the entire proton energy range for each pulse duration. In Fourier space, a high resolution image of the grid will result in well defined mode structure. As the resolution is degraded, fewer high order modes will be present in the Fourier transform. In addition, distortion or warping of the grid pattern will result in broadening of the mode features. Line-outs through the 2D Fourier transforms of the shown proton data are plotted together in Figure 4.4(d). The periodic mode structure is evident the 0.7 ps data, while the 10 ps results are broadened and less prominent due to the distortion of the grid. Just as there is no visible grid pattern in the 100 ps data, no mode structure appears in the Fourier transform.

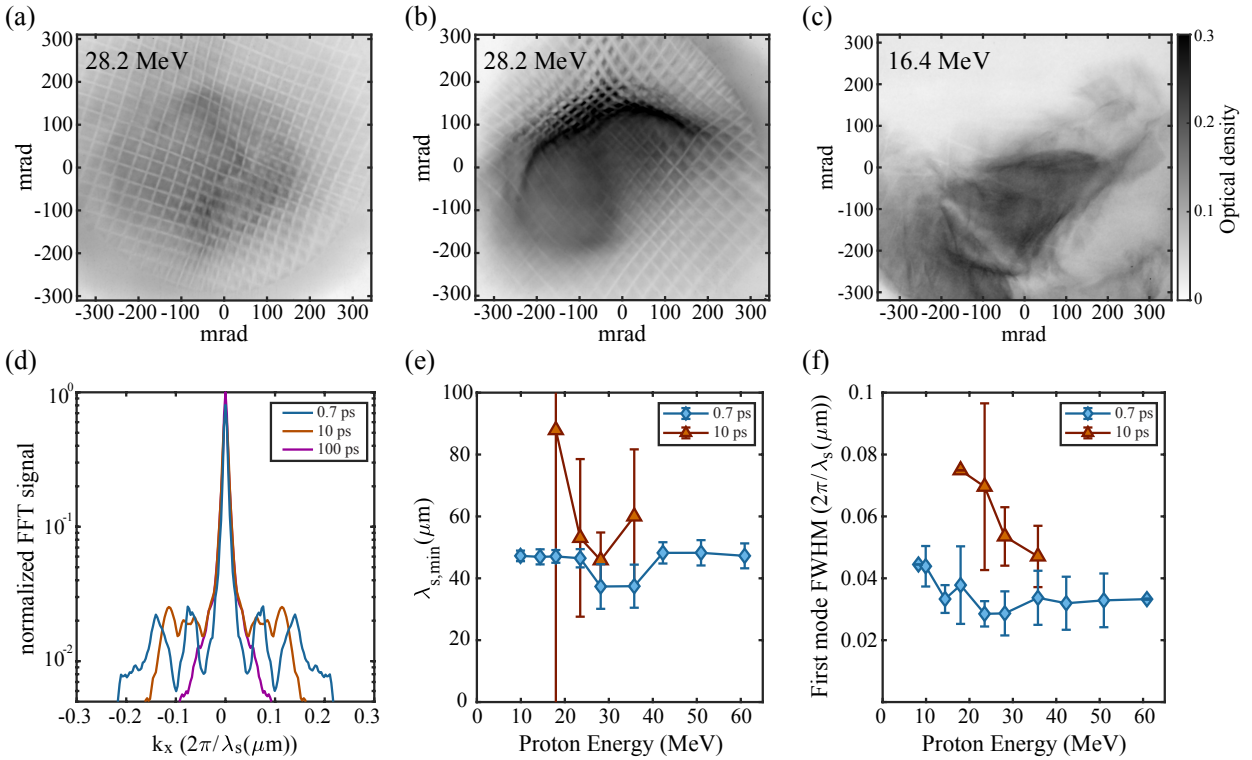

Figure 4.4: (a-c) Selected RCF data from the highest intensity shot for each pulse duration: (a) 0.7 ps, (b) 10 ps, and (c) 100 ps. (d) Line-outs through the 2D Fourier transforms of the data in (a-c) shows the effect of the proton beam quality the on mode structure. Analysis of the Fourier transforms reveals the minimum spatial wavelength resolved (e) and the broadening of the first mode peak due to distortion of the grid pattern (f).

The highest order mode observed along the primary grid axes can be interpreted as the average minimum spatial scale resolved ($k_{s,max} = 2\pi/\lambda_{s,min}$). Figure 4.4(e) shows the minimum spatial scale resolved across the entire energy spectrum for the 0.7 and 10 ps results. The error bars include effects of anisotropy in the mode structure (i.e., $k_{x,max} \neq k_{y,max}$) and uncertainty in the magnification of the grid image. Low energy portions of the beams and all of the 100 ps results fall well above the plotted range. As a measure of the warping and distortion, the full width at half maximum of the first order mode is plotted in Figure 4.4(f).

Overall, the 0.7 ps pulse duration results in the best beam quality. However, even the best beam exhibits degraded imaging quality for protons with kinetic energies below 10 MeV. At higher energies, despite a visually uniform beam and grid structure, the resolution appears degraded likely due to a combination of reduced proton signal, increased transmission

through the grids (reduced contrast), and scattering of the high energy protons as they pass through front layers of the RCF stack.

As the laser pulse duration is increased, the beam quality is significantly degraded. Though still visible in the 10 ps case, strong modulations in the beam profile distort and blur the grid pattern. With a 100 ps pulse duration, poor beam quality renders the grid nearly indistinguishable across the entire spectrum.

Even for the most uniform beams, there is still some warping and distortion of the grid pattern. This can likely be attributed to electrical charging of the grid target by the fast electrons passing through in advance of the proton beam and the electrons that co-propagate with the protons. This effect will be more pronounced for slower protons which pass through the grid after charge has been deposited by the higher energy portion of the beam. In addition, the slower velocity means the low energy protons will experience larger deflections. Often times during proton radiography experiments carried out on OMEGA EP, the proton source foil is enclosed in a plastic tube capped by a thin foil in order to protect it from ambient plasma, debris or radiation from the primary interaction (see for example the experimental setup used by Gao *et al.* [8]). This tube assembly could potentially experience similar, or more pronounced, charging effects, impacting the lower energy portions of the proton beams.

4.4 Simulation results

In order to explore the impact of laser pulse duration on the underlying interaction dynamics and ion acceleration, we performed 2D particle-in-cell (PIC) simulations with the fully relativistic OSIRIS 4.0 framework [123]. We examined the interaction of laser pulses different durations with over-dense targets. In the experiment, the pulse durations ranged from a few times the ion response time, $t_i \approx 2\pi/\omega_{pi}$, to 10s or 100s of t_i. This suggests that ion motion during the longer pulses likely influences the interaction dynamics and could contribute to differences observed experimentally. Due to the computational expense of carrying out PIC

simulations lasting many tens of ps, we chose to reduce the simulated ion mass in order to speed up the ion dynamics. This allows us to approximate the long timescale dynamics with shorter, more computationally accessible pulse durations. The following results compare the interactions of a $1\tau_0$ laser pulse and a $10\tau_0$ pulse, where τ_0 is defined to be 100 fs. Consistent with the experiment, the longer pulse duration has more energy, but lower intensity. Here the $1\tau_0$ pulse has a peak normalized intensity (a_0) of 5, while the longer $10\tau_0$ pulse is reduced to $a_0 = 2.5$. The laser pulses interact at normal incidence with an over-dense plasma slab. The peak density is $25n_c$, where $n_c = \epsilon_0 m_e \omega_0^2 / e^2$ is the critical density for a laser frequency ω_0. A uniform exponential profile with a characteristic scale length of $\lambda_0/2$ extends from the front surface, where λ_0 is the laser wavelength. The front and rear surfaces of the target are composed of reduced-mass protons ($m_p^* = 0.1 m_p$), while the bulk target has a mass of $m_i^* = 2m_p^*$. The bulk target is $10\lambda_0$ thick and the rear reduced-mass proton layer thickness is $1\lambda_0$. The simulation box size is 1200×1200 $(\mathrm{c}/\omega_0)^2$ and is resolved by 12000×12000 cells with 100 particles-per-cell for both ions and electrons. Cubic particle interpolation was used to limit numerical heating. Absorbing boundary conditions were used for the particles and open, Perfectly Matched Layers (PML) boundaries for the fields.

Previous studies of laser-accelerated proton beams have concluded that filamentation instabilities driven by the high energy electrons determine the beam quality and emittance [56]. The filamented electron beam can drive strong return currents and generate filamentary magnetic field structures which deflect protons away from otherwise uniform trajectories. In addition, the presence of a low density preformed plasma on the rear surface of the target in advance of the peak of the laser pulse has been shown to enhance Weibel-like instability formation that can lead to strong modulations in the accelerated proton beam [141, 142]. Even without filamentation, recent work by Nakatsutsumi *et al.* using higher intensities and thinner targets demonstrated that strong azimuthal magnetic fields on the rear surface can inhibit proton acceleration and impact the beam quality [143]. With these simulations, we investigate the influence of pulse duration on emittance growth mechanisms.

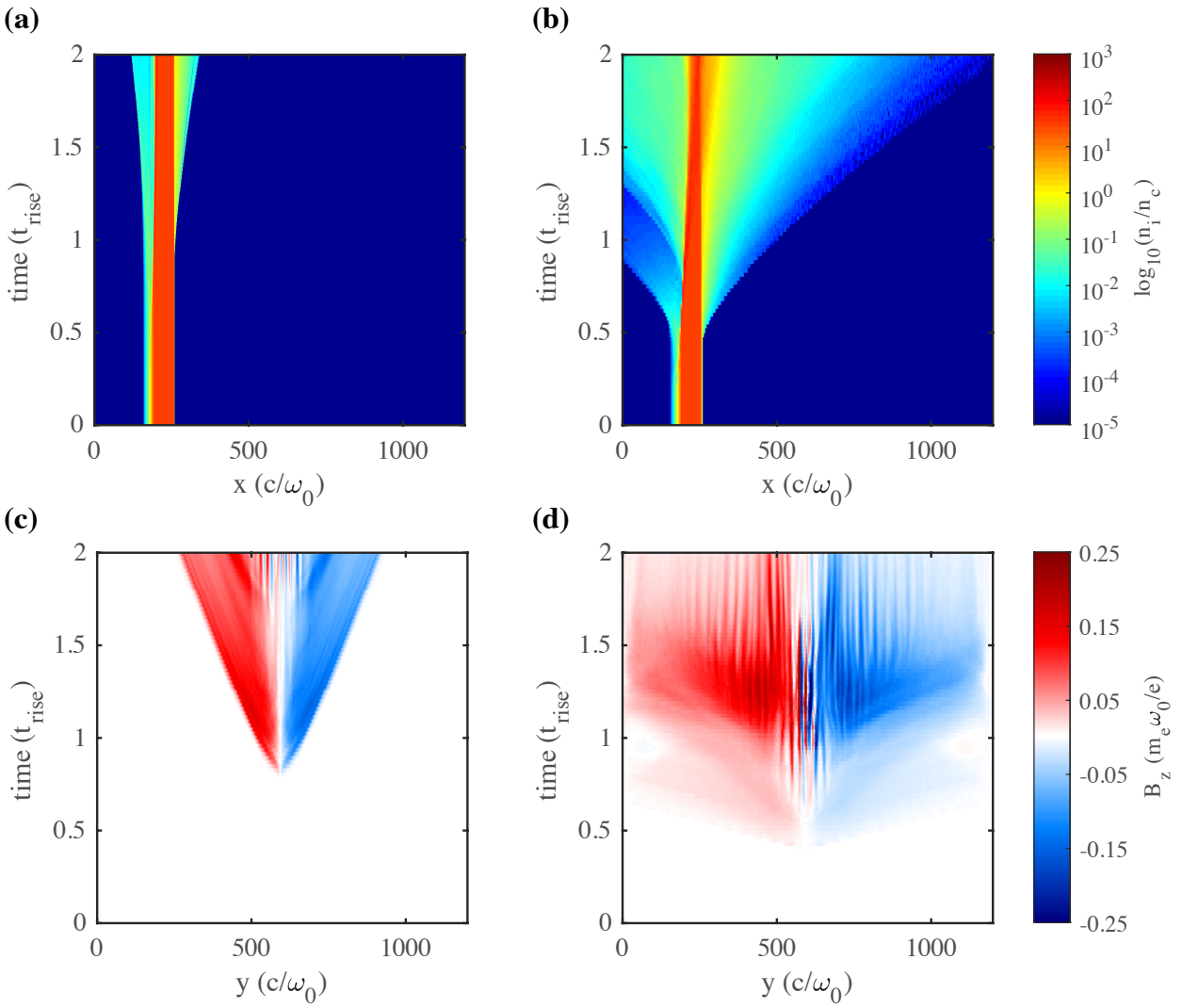

Figure 4.5: The time evolution of the ion density (a-b) and out-of-plane magnetic field (c-d) is compared between the two pulse durations. The time axis is normalized to the rise time of the respective laser pulse, with the left column corresponding the a $1\tau_0$ pulse and the right to the $10\tau_0$ pulse. The ion density is measured along the laser axis and the magnetic field is measured at the rear surface of the target.

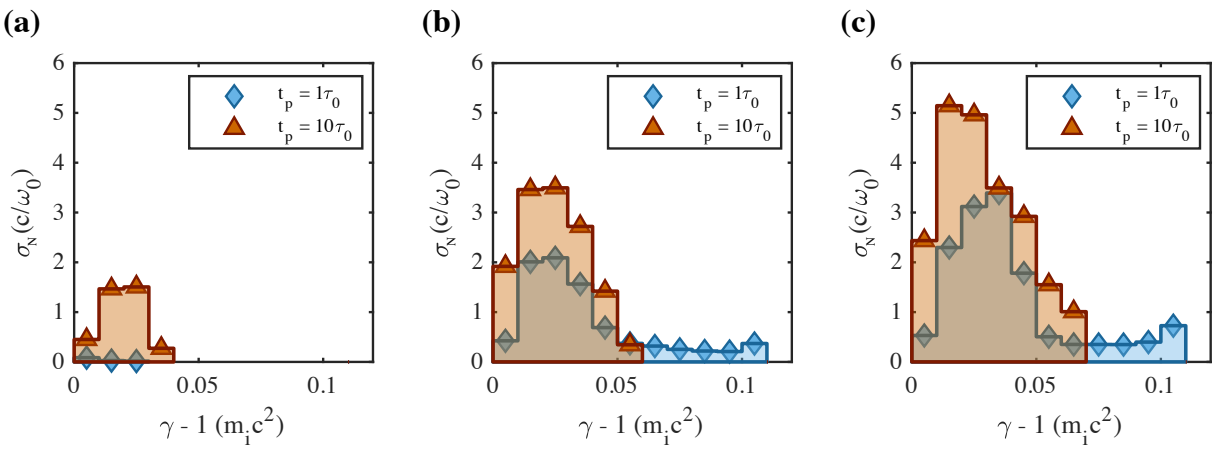

Figure 4.6: The normalized emittance, σ_N, is measured for 10 energy bins across the spectra for both pulse durations. To capture the evolution, the emittance is measured at peak of the pulse (a), $5\tau_0$ after the peak (b), and $10\tau_0$ after the peak (c).

The temporal evolution of the ion density and rear-surface magnetic field are shown in Figure 4.5. In each panel, the time axis is normalized to the rise time of the respective laser pulse, with the peak arriving on target at time = 1. The first column corresponds to the $1\tau_0$ pulse duration and the second column to the $10\tau_0$ pulse duration. The ion density evolution (Figure 4.5 (a) and (b)) reveals significantly more expansion of low density plasma from the rear surface of the target during the rise time of the $10\tau_0$ pulse. While filamentary structures are evident in the out-of-plane magnetic field in both pulse duration cases (Figure 4.5 (c) and (d)), the fields are enhanced in the longer pulse duration case despite lower incident laser intensity.

To assess the accelerated beam quality, the normalized transverse emittance of the protons was measured for 10 bins across the energy spectra. The normalized emittance describes the phase space area occupied by the beam, and is a conserved quantity during vacuum propagation. For the following analysis, the normalized emittance is calculated as:

$$\sigma_N = \sqrt{\langle y^2 \rangle \langle (p_y/mc)^2 \rangle - \langle y p_y/mc \rangle^2}$$

where y is the transverse spatial dimension, p_y is the transverse momentum, and $\langle\rangle$ signifies

the distribution average. Good beam quality is associated with a *lower* emittance. Figure 4.6 shows the temporal evolution of the normalized emittance for both pulse durations as a function of proton energy. Figure 4.6(a) corresponds the arrival time of the peak of the respective pulse. Panels (b) and (c) correspond to $5\tau_0$ and $10\tau_0$ after the peak, respectively. There is good qualitative agreement between the simulation results and the experiment. The higher energy portions of the short pulse case have the lowest emittance, while the lower energy protons are more strongly impacted by the developing filamentary field structures. The longer pulse duration exhibits a larger overall emittance. In addition, ion acceleration and emittance growth has already commenced by the time the peak of the pulse arrives on target (Figure 4.6(a)).

Direct comparison of simulations to the experiments is challenging because the interaction and ion acceleration depend strongly the exact details of the laser pulse profile and the target composition and thickness. For example, as previous studies have noted [56], electron-ion collisions in the bulk target will help smooth current filaments, particularly for high-Z target materials. Without including collisions, our simulations potentially overestimate strength of the filaments and the extent of the preformed plasma expansion. However, we do not expect collisional effects to change the general trends observed here.

4.5 Discussion

In the experiment, we observed a significant degradation of the proton beam quality as we increased the laser pulse duration. The 2D PIC simulation results suggest that ion motion during the rise time of the longer pulses leads to enhanced plasma expansion from the rear surface of the target and to formation of stronger filamentary field structures. The characteristic scale length of preformed plasma at the peak of the pulse can be estimated by $l_s = c_s t_p/2$, where $c_s = (Zk_BT_{he}/m_i)^{1/2}$ is the sound speed with hot electron temperature k_BT_{he}, and t_p is the pulse duration. The hot electron temperature is given by the ponderomo-

tive potential [144] of the half-maximum laser intensity, $k_B T_{he} = m_e c^2[(1 + \langle a_0/2 \rangle^2)^{1/2} - 1]$, (here, $\langle\rangle$ represents the time average). From this, we can derive an approximate scaling for the characteristic plasma gradient length as a function of pulse duration and peak intensity,

$$l_s(\mu\text{m}) \propto (Z m_e/m_i)^{1/2}(a_0/2)^{1/2} t_p(\text{ps})/2.$$

Figure 4.7 shows a comparison of this simple model and the density profiles observed in the simulation. While the model overestimates the plasma scale length for the shorter pulse duration, there is reasonable agreement for the longer pulse duration case. At the very least, the model provides order of magnitude estimates of the extent of plasma formation on the rear surface. Turning to the experimental data, we predict $l_s \approx 6$ μm, 50 μm, and 266 μm for the 0.7 ps, 10 ps, and 100 ps pulse duration shots compared in Figures 4.3 and 4.4. While charging of the secondary target certainly contributes to the distortion of the grid pattern, simulations suggests that most of the structures and non-uniformity in the beam can be attributed to enhanced expansion of the target during the longer pulses.

In addition to degrading the beam quality, large preformed plasma density gradients should reduce maximum proton energies. With a sharp interface, the maximum sheath electric field is given $E = \sqrt{2} k_B T_e / e\lambda_D$, where $k_B T_e$ is the hot electron temperature, e is the electron charge, and λ_D is the Debye length [78]. However if $l_s \gg \lambda_D$, the field is reduced to $E = k_B T_e / e l_s$ [135]. Alternatively, strong magnetic fields can inhibit sheath formation by confining or scattering hot electrons away from the central axis [143]. In Figure 4.8, the maximum proton energies observed in the experiment are compared with predictions based on the analytical model described by Schreiber *et al.* [4]. As mentioned above, the RCF measurements likely slightly underestimate the maximum proton energies and represent a lower bound. In general, the 0.7 ps results show reasonable agreement with the model, while the 10 ps and 100 ps results fall below the predictions. Unlike other models [78, 79], the Schreiber model stays finite as $t_p \to \infty$, and therefore appears to more accurately predict the maximum proton energies for the 100 ps pulse duration results. Despite the long scale

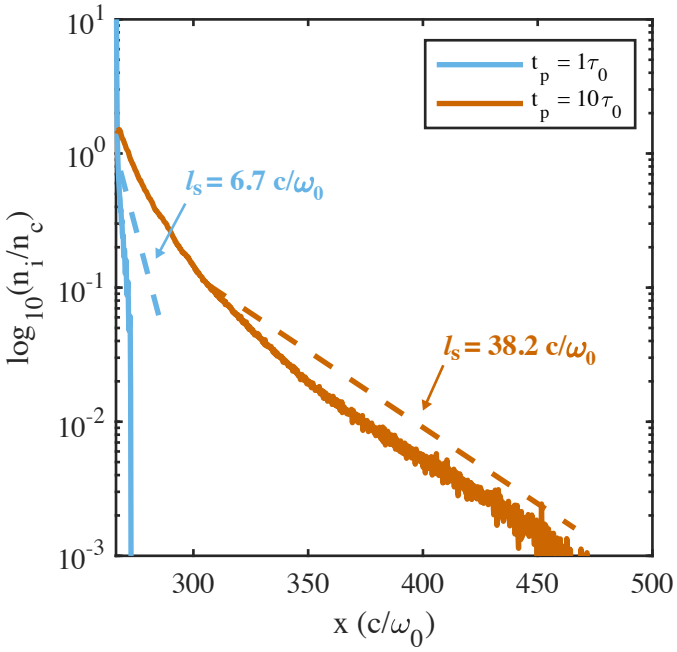

Figure 4.7: At the peak of the respective laser pulse, the rear surface plasma profile from the simulations is compared with the simple scale length estimate developed in the text (dashed lines).

lengths predicted, protons are still accelerated to multi-MeV energies in all cases, potentially due to the impact of super-ponderomotive electron heating or laser self-focusing in front-side preformed plasma. Maximum energies measured here in the 100 ps pulse duration case exceed previous observations from kilojoule-class laser-solid interactions with 100s of ps pulse durations and lower intensities [145, 146].

4.6 Conclusion

For high energy, high power laser systems, these results demonstrate that the laser pulse duration should be minimized to limit expansion of plasma from the rear target surface during the pulse and ensure optimal proton beam quality. While the promise of superponderomotive electron heating and favorable ion energy scaling from multipicosecond interactions may yet prove useful for other applications, such as fast ignition [105, 127] and neutron generation [147, 148], the non-uniformity of the accelerated proton beams make them unsuitable

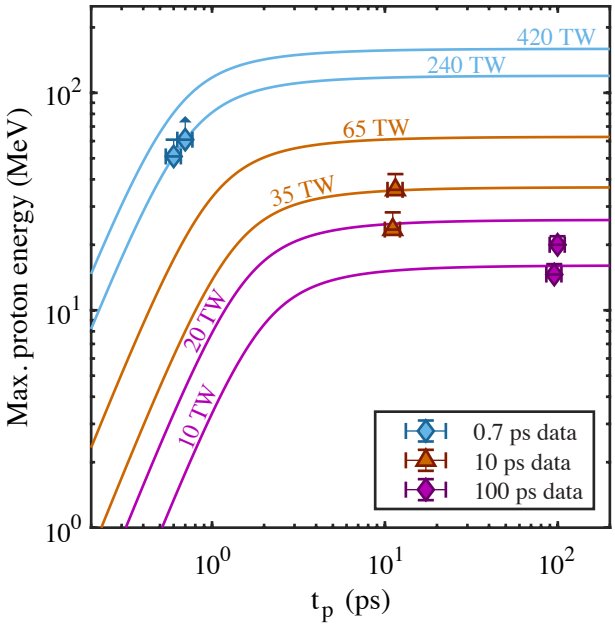

Figure 4.8: The maximum proton energies observed in the experiment are compared to the analytical model developed by Schreiber *et al.* [4]. For the highest intensity shot with a 0.7 ps pulse duration, the arrow indicates that the proton energy spectrum extended beyond the range detected by the RCF stack by an unknown amount.

for ultrafast proton radiography or other applications that require a uniform, low-emittance beam. Even with optimal laser pulse conditions, proton radiography experiments and detector stacks should be designed to emphasize protons with energies exceeding 10 MeV. These results will be used in subsequent chapters, and can help guide future experimental designs both on OMEGA EP and other HED facilities, such as the NIF-ARC which can also produce kilojoule, multipicosecond laser pulses.

CHAPTER 5

Target Material Effects on Magnetic Field Generation Driven by High Power Lasers

In this chapter, experimental and computational observations of target material effects on magnetic field generation in high-power laser produced plasmas are discussed. Experiments performed with the OMEGA EP laser system explored both nanosecond laser pulses focused to moderate intensity ($I_L = 2 \times 10^{14}$ Wcm^{-2}) and multipicosecond pulses focused to high intensity ($I_L > 10^{19}$ Wcm^{-2}) interacting with foil targets. Using proton radiography, we measured the strength, spatial profile, and dynamics of self-generated magnetic fields as the target material was varied between plastic (CH), aluminum and copper. In the case of moderate intensity pulses, radiation-driven double ablation fronts in higher Z targets initiate multiple regions of Biermann battery ($\nabla T_e \times \nabla n_e$) magnetic field generation. Extended magneto-hydrodynamics (MHD) simulations with radiation transport reproduced key aspects of the experiment, including field generation and double ablation front formation. At high intensities, we observe rapid expansion of the magnetic fields, and enhanced filamentation in lower Z, insulator targets. Particle-in-cell simulations are used to elucidate the generation mechanism and evolution of magnetic fields, as well as the impact of preformed plasma scale length on laser-driven field generation. These results should help inform magnetized high energy density (HED) and laboratory astrophysics experiments, such as laser-driven magnetic reconnection, where precise knowledge of the initial magnetic field topology is crucial and can help benchmark computational models used to study HED

plasmas relevant to inertial confinement fusion.

5.1 Introduction

High power laser-matter interactions can create high energy density (HED) conditions with extreme temperatures, densities, and pressures in the laboratory [5]. This is of particular importance for inertial confinement fusion (ICF) research [17] and laboratory investigations of astrophysical phenomena [6]. At moderate intensities, strong magnetic fields (∼MG) can be self-generated in high power laser-produced plasmas [7, 86, 87, 149]. The generation and spatial profile of such magnetic fields have important consequences for energy transport in ICF-relevant plasmas [12, 14–16, 21, 22], stabilization of hydrodynamic instabilities [23], and HED magnetic reconnection [25, 34, 36–38, 150]. At very high laser intensities, extremely strong self-generated fields (∼100 MG) facilitate exploration of exotic, high energy astrophysical processes in the laboratory [44, 45, 151–154]

The mechanisms governing magnetic field generation and transport depend on the laser intensity regime and the effect of target material is poorly understood. At moderate intensities, $I_L = 10^{14} - 10^{15}$ Wcm^{-2}, the laser pulse ablates the surface of the dense target. In this intensity range, low-Z targets should be fully ionized in the focal region. Laser energy is transported beyond the critical density by electron thermal conduction, which drives the ablation [19]. The low opacity means that radiation transport will have negligible impact on the ablation dynamics. Perpendicular temperature and density gradients in the ablated plasma plume generate strong azimuthal magnetic fields ($\mathcal{O}$ MG) via the Biermann battery mechanism ($dB/dt \propto \nabla T_e \times \nabla n_e$) [85]. Fast electrons accelerated during the laser-plasma interaction have a long mean-free-path compared to plasma gradient length scales. As a result, the fields can be advected away from the focal region through the Nernst effect [12, 16, 155]. While the plasmas are typically weakly magnetized, self-generated fields can still impact energy flow [16, 21, 22].

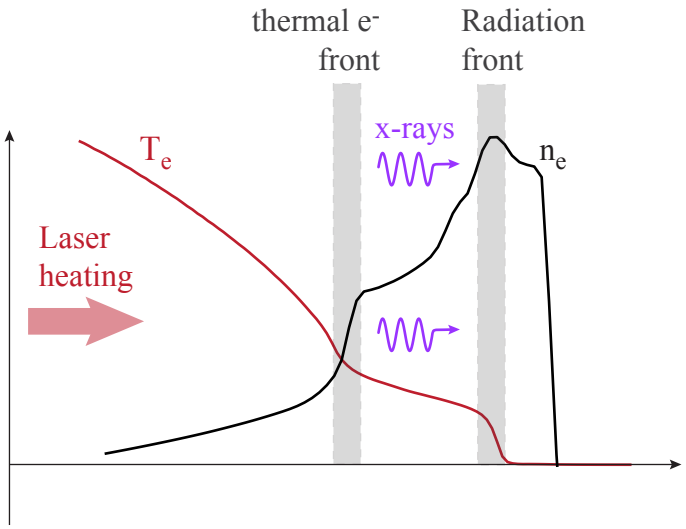

Figure 5.1: An illustration of double ablation front formation showing the electron temperature (red) and density (black) profiles. The laser heats plasma electrons from the left. In mid- to high-Z plasmas, the hot corona will emit strong radiation. The radiation and thermal electron energy will be absorbed at different locations resulting in two regions of strong temperature gradients separated by a "plateau" of relatively flat electron temperature.

At higher Z, the hot coronal plasma will emit strong radiation which is absorbed in dense, opaque regions of the target. This establishes a radiation driven ablation front, akin to x-ray driven ablation in indirect drive ICF [156–158]. At lower density, a combination of radiation and electron heat transport can drive a second ablation front. The two ablation regions are separated by a "plateau" of relatively flat density and temperature profiles. As a results, there are two distinct regions with strong gradients which can independently initiate Biermann battery magnetic field generation. The precise details these double ablation front (DAF) structures, such as the spatial extent of the plateau region, depend on the target material. An illustration of the ablation dynamics is shown in Figure 5.1.

Previous studies of DAF structures have primarily used 1D simulations to support analytic predictions [157, 158]. In general, research has focused on the prospect of taking advantage of DAF structures to inhibit lases-plasma instabilities and stabilize direct-drive ICF implosions [156–160]. More recently, DAF structures have been proposed as platform for laboratory investigations of stellar opacity [161]. Magnetic fields have been thus far

neglected, and any analysis of multidimensional effects has been limited to stabilization of hydrodynamic instabilities [156].

Due to limited availability of large-scale HED facilities such as the National Ignition Facility (NIF) or the OMEGA laser facility, computational modeling is an essential part of HED and ICF research. With this work, magnetic field generation in low to mid-Z plasmas can be compared with numerical models to validate predictions in this regime. Experiments with low-Z targets used high-precision proton radiography measurements to demonstrate that magneto-hydrodynamics (MHD) modeling must be extended to include Nernst advection, resistive magnetic diffusion and cross-field, Righi-Leduc heat flow in order to accurately predict the spatial profile of the magnetic fields [8, 47]. However, computational efforts often center on high-Z materials (typically gold) used in hohlraums for indirect drive ICF [21, 22]. Coupling between kinetic effects, radiation transport and magnetic field generation likely influence energy flow in mid to high-Z plasmas, as well as during ICF implosions [24].

When the laser intensity is increased such that $I_L \lambda_{\mu\mathrm{m}}^2 > 10^{18}$ $\mathrm{Wcm}^{-2}\mu\mathrm{m}^2$, the electric field of the laser pulse can accelerate target electrons to relativistic energies ($\lambda_{\mu\mathrm{m}}$ is the laser wavelength in microns). Accelerated electrons spread rapidly from the focal region, driving strong currents in the target. As fast electrons expand into vacuum from the target surfaces, the charge imbalance establishes a sheath electric field [78]. Strong azimuthal magnetic fields are generated by transverse gradients of the expanding sheath [9, 10, 89, 143]. The sheath electric field confines a portion of the fast electron population to expand along the target surface. This radially expanding sheet of current drives the sheath and azimuthal magnetic fields away from the focal spot with a velocity near the speed of light [9]. Recent experiments in this intensity regime have observed peak magnetic field strengths of 10-100 MG through optical probing [46, 162], ultrafast electron radiography [9], or proton radiography [10, 69]

Few experiments have directly measured the effect of target material on magnetic field generation driven by high intensity lasers. Schumaker *et al.* discussed the potential for target-dependent levels of preformed plasma expansion to impact field generation [9], while

Albertazzi *et al.* observed subtle differences between aluminum and gold targets [69]. Poor resolution, either due to the broad electron spectrum [9] or due to scattering of low energy protons in the dense target [69], limited the ability to clearly resolve differences between the materials.

In this chapter, we report on systematic, high resolution proton radiography measurements of target material effects on magnetic field topology generated during high power laser-solid interactions. In both intensity regimes, clear qualitative differences were observed in the proton images. In the moderate intensity case, experimental results coupled with extended magneto-radiation hydrodynamics simulations demonstrate that radiation-driven double ablation front (DAF) structures in mid-Z targets establish two distinct regions of Biermann battery field generation. At higher intensities, we measure enhanced filamentation of relativistic electrons in low-Z, insulating targets compared to conductors. A simple particle-in-cell (PIC) model is used to explore the fundamental mechanism governing magnetic field generation by high intensity pulses. In addition, 2D PIC simulations are used to explore the impact of preformed plasma scale length, whether due to laser prepulse or pre-expansion of the target, on the details high intensity laser-driven magnetic field generation.

5.2 Experimental methods

Experiments were performed with the OMEGA EP laser system at the University of Rochester's Laboratory for Laser Energetics, which can produce energetic pulses with durations ranging from 0.7 ps to 10 ns. The flexibility of the system facilitates investigations spanning large intensity and pulse duration ranges. In these experiments, we examined effect of target material on laser-driven magnetic field generation in two intensity regimes. High power, moderate intensity interactions were driven by a long pulse beam with a 351 nm wavelength, 1250 J of energy and 1 ns square temporal profile was focused to an 820 μm diameter super-Gaussian spot with a peak intensity of $(2.2 \pm 0.07) \times 10^{14}$ Wcm^{-2}. High

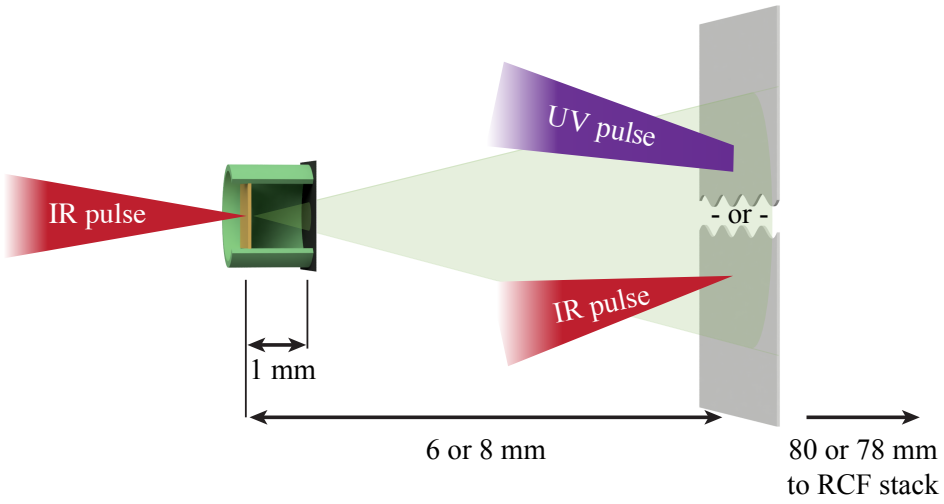

Figure 5.2: A schematic of the OMEGA EP experiment.

intensity interactions were driven a 500 J, 10 ps infrared (IR) pulse was focused on target by an $f/1.8$ off-axis parabolic mirror to intensities of $(5 \pm 1) \times 10^{19}$ Wcm^{-2}. Thin foil targets were either 50 μm thick CH plastic, 25 μm thick copper, 25 μm thick aluminum, or 50 μm thick aluminum coated with 1 μm of copper.

Protons accelerated by the target normal sheath acceleration (TNSA) mechanism [50–53] were used to image the magnetic field structures in a point-projection geometry. A second high intensity laser with 300 J in a 0.7 ps pulse was focused to intensities exceeding 10^{20} Wcm^{-2} on to 1×1 mm^2 foils. The proton source foils were either 50 μm thick copper or 20 μm thick gold. In order to protect the proton source from x-ray preheat and plasma generated during the main interaction, the high intensity laser target was housed in a plastic tube capped by a 5 μm tantalum foil, similar to the assembly described by L. Gao *et al* [8]. After passing through the main interaction, the proton beams were detected by stacks of radiochromic film (RCF). As shown in Figure 5.2, the proton source was positioned 6 or 8 mm in front of the main interaction and the RCF stack was 80 or 78 mm behind, resulting in magnifications of 14.3 or 10.8.

The accelerated proton beams in the experiment exhibited a quasi-Maxwellian energy spectrum typical of the TNSA mechanism with maximum energies exceeding 60 MeV. Due

to time-of-flight dispersion of protons between the source and main interaction, the broad spectrum makes possible single shot, time-resolved measurements of ultrafast dynamics with picosecond temporal resolution (as shown in references [10] and [60], for example). The relative timing between laser pulses could be adjusted with ±20 ps error in order to measure the full dynamics of more slowly evolving features associated with the moderate intensity interactions. After converting the raw RCF signal to proton dose [108, 110], quantitative magnetic field measurements can be retrieved from the relative transverse deflections of protons in the beam [48, 118] as described in Chapter 3.4.

5.3 Magnetic signatures of double ablation fronts

When comparing material effects on the magnetic fields generated by the moderate intensity UV beam, the relative timing between the nanosecond UV pulse and the high intensity pulse accelerating the proton probe was set to 750 ps. Figure 5.3(a-c) compares the proton images of the field topology for plastic (CH), aluminum, and copper-coated aluminum taken with 42.8 MeV protons. In all cases, we observe a strong ring patterns of proton accumulation. The CH results closely resemble those published by Gao *et al.* [8], with a pronounced ring pattern associated with azimuthal fields generated by strong perpendicular temperature and density gradients surrounding the laser focal spot. Due to the Nernst effect, the fields are convected by fast electrons ($v_e \approx 2 - 3 \times v_{the}$) to lower density, lower temperature regions near the edge of the ablated plasma [8,12,15,16]. A faint ring with larger radius is the result of weaker fields present near the edge of the expanding coronal plasma [8]. The primary difference between the different materials is emergence of a second prominent concentric ring of proton accumulation in higher-Z targets. The radial separation of the two rings increases between aluminum and copper-coated aluminum targets, indicating that the radial extent of magnetic fields is sensitive to the atomic number of the target.

Due to the azimuthal symmetry of the ring features, a 1D polar-coordinates image in-

version technique can extract magnetic field information. Using the method described in Chapter 3.4.3, radial line-outs from the proton fluence were inverted for each material. The primary challenge of proton image interpretation is the accurate inference of the undisturbed, reference proton profile. No reference data was taken due to limited shot time and significant shot-to-shot fluctuations in the beam profile and total signal which would render any reference data ineffective.

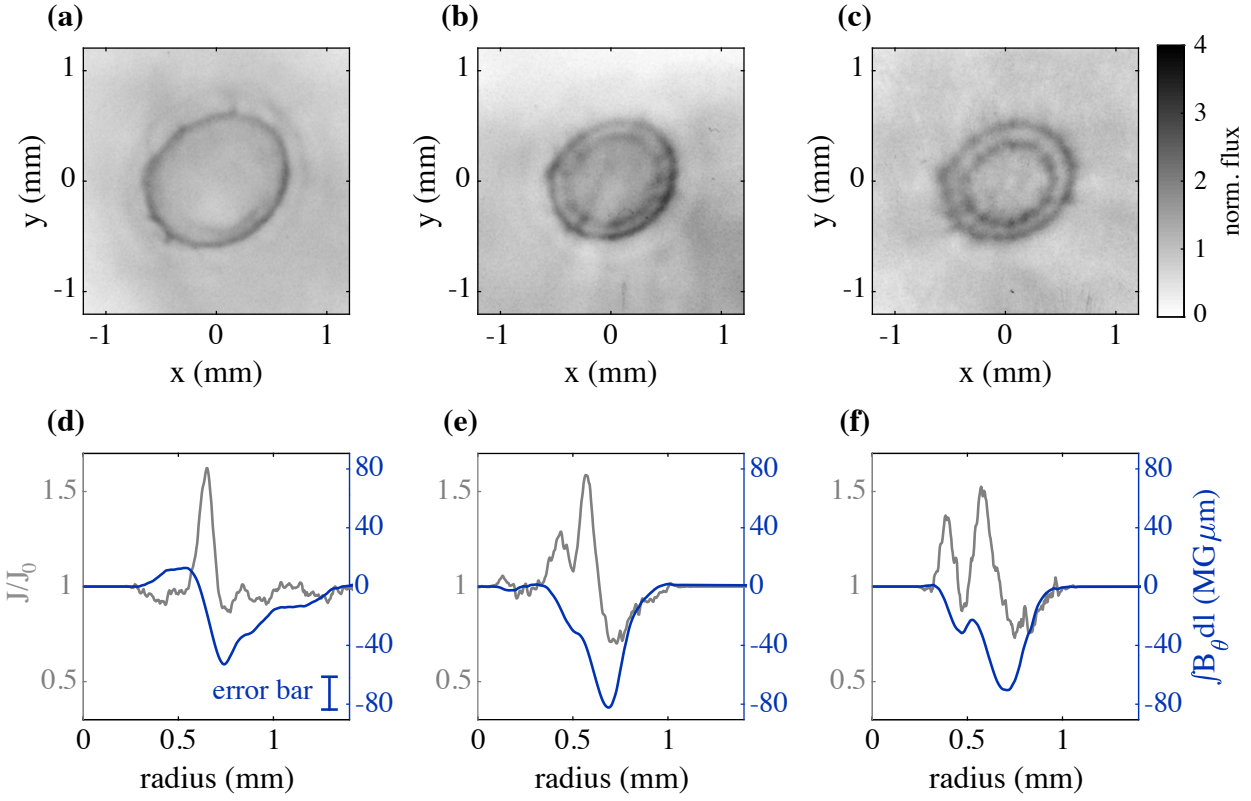

Figure 5.3: Experimental proton images for three different target compositions: (a) plastic (CH), (b) aluminum, (c) aluminum with a 1 μm copper coating. The fields were measured by 42.8 MeV protons. Corresponding 1D-polar inversion results are shown in (d-f). For each material, the line-out normalized by the inferred reference (J/J_0, gray) and the resulting field profile (blue) are plotted. Two concentric rings present with high Z targets is due to Biermann battery magnetic field generation at both fronts of a double ablation front structure.

Here, undisturbed profiles (J_0) were inferred directly from the radial line-outs (J) using iterative Fourier filtering. During each iteration, a Gaussian low-pass Fourier filter is applied to line-out. Then the total signal is adjusted such the flux is conserved (i.e. $\sum J = \sum J_0$) A

key assumption made during this analysis is that the fields should drop to zero at the center and near the outer edge of the image. This is accomplished by blending the filtered signal with the original line-out near the edges using a super-Gaussian mask, such that $J/J_0 = 1$ as $r \to 0$ and $r \to r_{max}$. The filter and super-Gaussian widths are manually adjusted until the inverted field goes to zero as $r \to r_{max}$.

The resulting J/J_0 and inverted path-integrated magnetic field structure for each material are shown in Figure 5.3(d-f). Uncertainties in determining J_0 and blurring due small-angle proton scattering in the solid targets introduces large errors in absolute field strength (~ 20 MGμm). In addition, this interpretation assumes all deflections are due to magnetic fields because electric fields are expected to be relatively weak [8].

Based on the proton images and path-integrated fields, the plastic target has expanded to the largest radius. The peak field occurs at ≈0.6 mm, near the edge of the driving laser focal spot, and coronal fields extend to >1 mm radius in excellent agreement with previously published results [8]. Changing the material from CH to Al or Cu, an interior field structure emerges which becomes more prominent at high Z. This is indicative of the formation of second ablation front region with strong temperature gradients.

Two-dimensional (2D), cylindrically-symmetric simulations were performed using the extended-magnetohydrodynamics (MHD) code, Gorgon [24,163,164]. Gorgon includes magnetic transport from bulk plasma flow, Nernst, cross-gradient-Nernst, resistive diffusion and Biermann Battery generation [24]. The thermal transport is anisotropic and includes Righi-Leduc heat-flow. Multi-group non-diffusive radiation transport is also utilized using a P 1/3 automatic flux-limiting method. The Frankfurt equation of state (FEoS) is used [165]. The laser is treated using a ray-trace method with inverse-Bremsstrahlung heating of the electron population.

In general, the simulations of the CH target agree with both previous simulation work [8,47] and the experimental results presented here. A single ring of azimuthal magnetic field is generated via the Biermann battery mechanism in the strong temperature and density

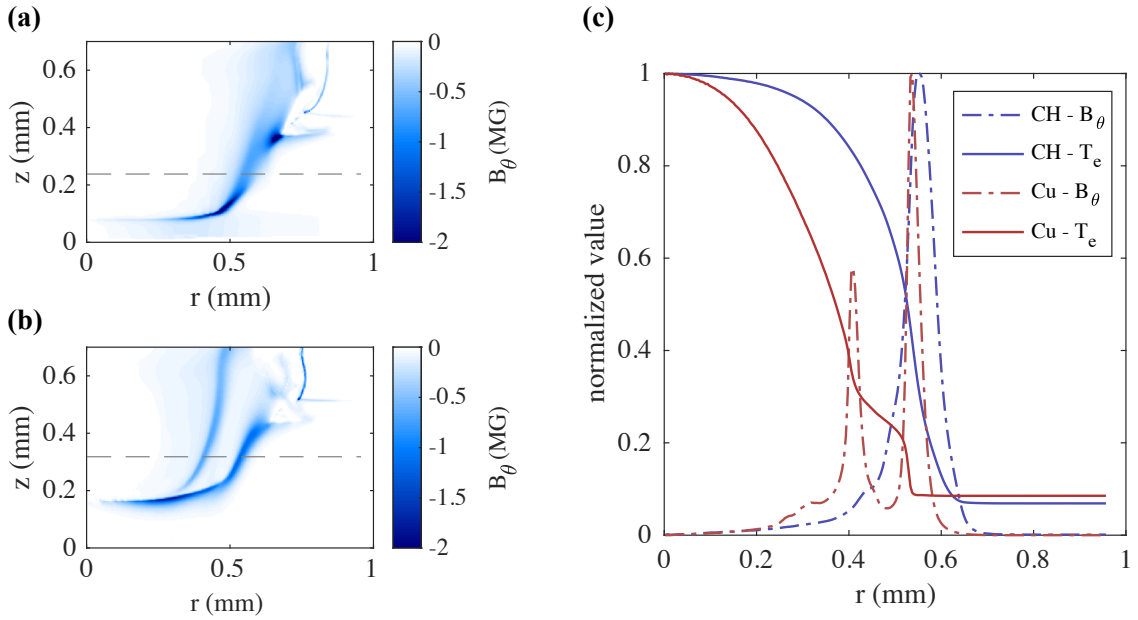

Figure 5.4: 2D axisymmetric Gorgon simulation results show Biermann battery field generation profiles for CH (a) and Cu (b) at a time of 750 ps. Radial profiles (along the lines indicated in (a) and (b)) of the magnetic field and electron temperature are plotted together in panel (c).

gradients near the edge of the laser focal spot. For copper targets, the simulations reveal a double ablation front at the target surface. The hotter coronal plasma is dominated by thermal conduction, while the denser plasma is dominated by radiation transport. As a result, there are two regions of strong field generation - one located near the electron thermal conduction ablation front (inner) and the other near the radiation driven front (outer). Between the two ablation fronts is a "plateau" region of relatively low temperature gradient. Therefore, the Nernst effect is suppressed and the inner field is not advected toward the outer field.

The simulation results are summarized in Figure 5.4. Taken at $t = 750$ ps to match the experimental measurements shown in Figure 5.3, the 2D magnetic field profiles for CH and copper are shown in Figure 5.4(a) and (b). Radial line-outs through the magnetic field and electron temperature for each material are plotted in Figure 5.4(c). The line-out location is

indicated by the dashed line in (a) and (b). Two distinct radial regions of field generation are evident in the copper simulation. The line-outs shows the spatial relationship between the strong temperature gradients at each ablation front and the magnetic field generation. The separation between the fields is determined by the width of the "plateau" region between the ablation fronts.

From the simulations, the plasma β can be calculated to characterize the relative importance of thermal and magnetic pressures on the dynamics ($\beta = n_e k_B T_e/(B^2/2\mu_0)$). Laser-driven plasmas are typically strongly driven ($\beta \gg 1$). In the CH target simulation, the strongest magnetic field regions in the coronal plasma correspond to β in the range of ∼25–50. A similar β range is observed in the inner field region (thermal electron front) of copper simulation, however the strong fields and relatively low temperatures at the outer field region (radiation front) result in $\beta \sim 5$. Therefore, the magnetic fields at the radiation front can play a more significant role in the plasma dynamics. This relatively low β could be an important consideration for interpretation of indirect drive ICF experiments or laser-driven magnetic reconnection experiments using higher Z targets.

5.3.1 Time evolution of double ablation fronts

Experimental measurements of the DAF temporal evolution can be used to further validate the simulation. In successive shots on 25 μm copper foils, the relative timing between the driving laser and proton probe was adjusted to measure 250 ps, 500 ps and 750 ps into the field evolution. The experimental results and corresponding simulated magnetic fields are compared in Figure 5.5.

Significant blurring due to scattering in the solid copper target limits the proton imaging resolution. However, two distinct rings of proton accumulation, evidence of the DAF structure, can be resolved after 750 ps. In the simulation, the double field structure forms by 500 ps and the fields continue grow over the subsequent 250 ps. Overall, there is qualitative agreement between the simulation and experiment, but improved imaging resolution

is necessary to make more complete comparisons. Future experiments could explore time evolution on layered targets.

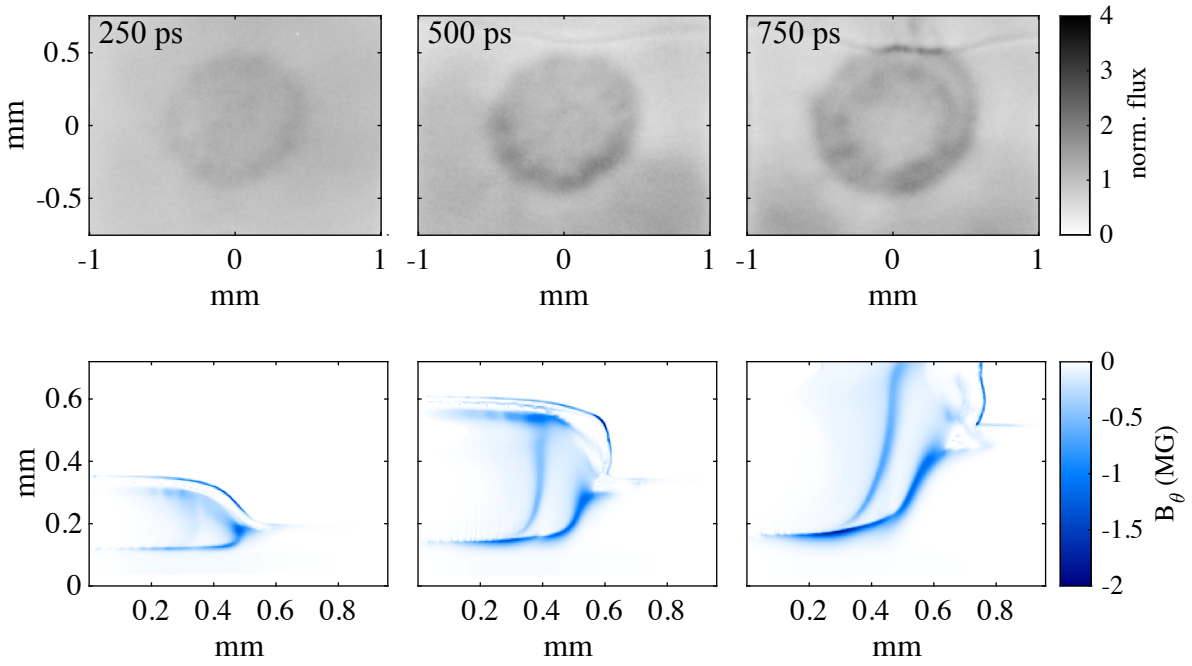

Figure 5.5: Measurements of the field evolution on solid copper foils made with 33.4 MeV protons at 250 ps, 500 ps, and 750 ps. Corresponding times from the Gorgon simulation are shown in the second row. Note, the top edge of the foil target is evident in the 500 ps and 750 ps experimental results. Note: numerical effects result in thin regions of spurious field generation at the edge of the expanding plasma.

The results of the material comparison and time evolution demonstrate that DAF structures drive two regions of Biermann battery magnetic field generation in higher Z targets. The combination of temperature plateaus and regions of high magnetization can influence electron heat transport. In addition to non-local transport, radiation plays an important role in the evolution of self-generated magnetic fields. While the simulations presented here show clear evidence of DAF structures, future work will improve the modeling to mitigate spurious fields that form near the plasma-vacuum edge, though these are not expected to significantly alter the conclusions drawn here. Future work will improve the radiation boundary conditions which caused these simulation to over estimate the effect of radiation far from the focal spot.

5.4 Material effects in high intensity interactions

At high intensity, the strong azimuthal magnetic fields are generated by transverse gradients of the expanding sheath electric field [89, 143]. The peak electric field strength on the surface of the target can be estimated $E_0 = \sqrt{2}k_B T_e/e\lambda_D = \sqrt{2n_e k_B T_e/\epsilon_0}$, where $k_B T_e$ is the temperature of the hot electron population, e is the elementary charge, and λ_D is the Debye length [78]. From Faraday's law, assuming the sheath field is azimuthally symmetric and primarily oriented in the target normal ($\pm\hat{z}$) direction, $\partial \boldsymbol{B}/\partial t = -\nabla \times \boldsymbol{E} \approx \partial E_z/\partial r$, and we can predict the peak azimuthal field magnetic field strength:

$$\frac{B_\theta}{\Delta t} \approx \frac{E_z}{\Delta r} \quad \Rightarrow \quad B_0 \approx E_0/c \quad \Rightarrow \quad B_0 \approx \sqrt{2\mu_0 n_e k_B T_e}. \tag{5.1}$$

Assuming a conversion efficiency f from laser energy E_L to hot electron energy, the number of electrons accelerated can be estimated by $N_e \approx fE_L/k_B T_e$, with f typically $\approx 0.1 - 0.3$ [79,166]. The "acceleration volume" is approximately $ct_L \times \pi r_L^2$, where r_L and t_L are the focal spot radius and laser pulse duration, respectively. We can calculate the density of electrons driving the field generation by $n_e \approx fE_L/(ct_L \pi r_L^2)k_B T_e \approx fI_L/ck_B T_e$. Therefore, we can derive an expression for the peak magnetic field strength as a function of laser intensity:

$$B_0 = \sqrt{2\mu_0 f I_L/c}.$$

From this simple model, we estimate peak field strengths of ≈ 200 MG for the laser intensity used in this experiment. As the fields expand, the strength should decrease following a $1/r$ dependence [9].

Proton images of fields generated on a copper, aluminum, or plastic (CH) target are compared in Figure 5.6. Each series corresponds to a single shot measurement, and the proton energies ranged from approximately 20 to 40 MeV. The relative timing on each RCF layer is based on the different times-of-flight for the corresponding proton energies, and t_0

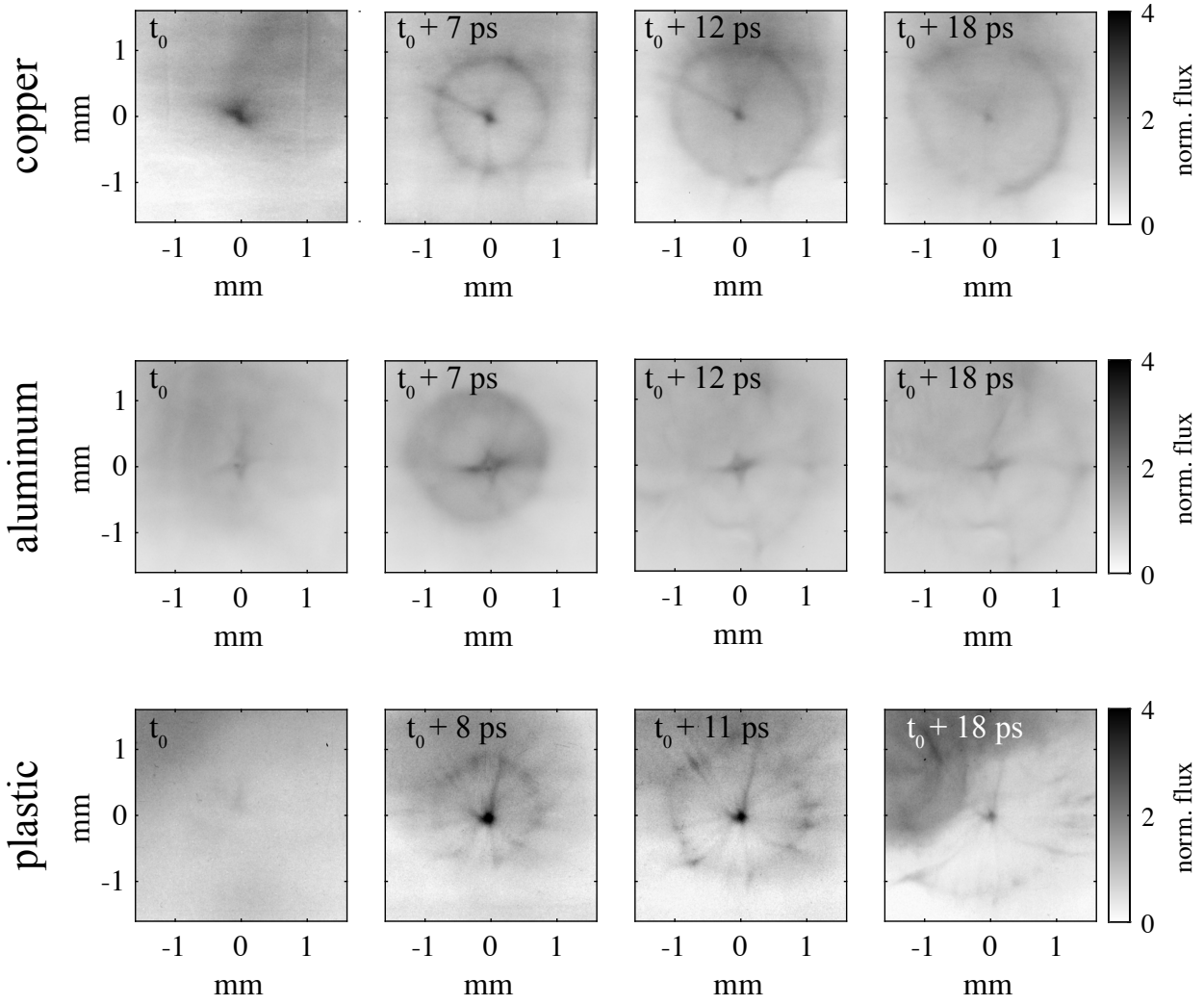

Figure 5.6: Proton images of magnetic field generation and evolution driven by the interaction of a high intensity laser pulse with a copper, aluminum or plastic target.

was chosen to be the first RCF layer to exhibit evidence of the fields. The spacing between layers in the RCF stack yielded a 3 to 6 ps time sampling. Therefore, confidence in t_0 is limited to $\approx \pm 3$ ps, however the relative timing is well determined by the stack design.

Quantitative measurements of the field strengths in this geometry is challenging because the fields are strong enough to cause crossing proton trajectories and caustic features in the image. In addition, protons accelerated during the main high intensity interaction will also be detected on the RCF, producing a non-uniform background signal. Despite these limitations, we can still draw comparisons between the different materials using the proton

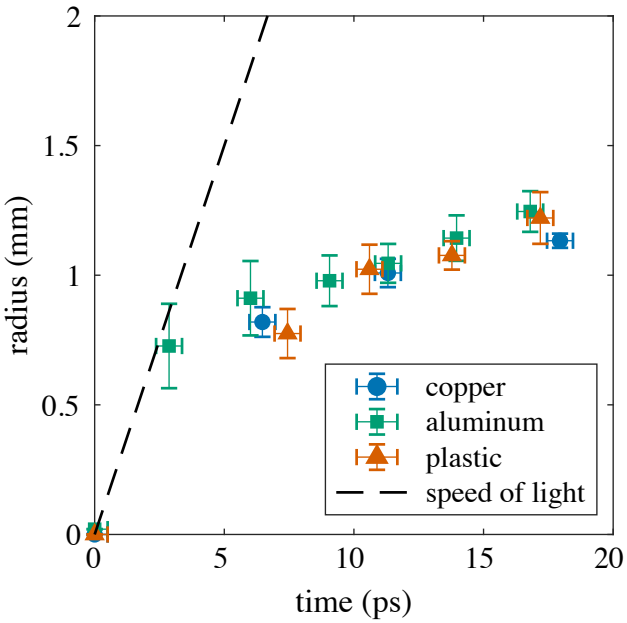

Figure 5.7: Measurements of the ring feature radius for each material are plotted as a function of time

images. The copper result exhibits a ring-dot caustic structure similar to those observed by Sarri *et al.* [10]. While still present, the ring feature is less prominent and more disrupted for aluminum target. In the plastic target case, numerous spoke-like features extend from the central dot, and the ring feature is strongly disrupted. Figure 5.7 compares the average radius of the ring features as a function of time for the different material. In general, the ring expands to a radius of approximately 1 mm, with the initial expansion near the speed of light. This is rapid expansion and then slowing is consistent with measurements made by Schumaker *et al.* [9] and Sarri *et al.* [10], though the radial extent observed here is much larger likely due to higher driving laser energy (500 J compared to $\sim$ 1 J and 50 J, respectively).

In order to investigate the origin of the spoke-like features in the proton images, a forward-scattering approach was used to generate synthetic proton images using test fields (see Section 3.4.4 for details on this approach). The functional form for the path-integrated magnetic

field profile is

$$\int B_\theta \mathrm{d}z = -B_1 \frac{\sqrt{\pi}\delta l_1}{a_1} r \exp\big[-(r/a_1)^2\big]\sqrt{2}\exp[1/2] + B_2 \frac{\sqrt{\pi}\delta l_2}{a_2} r \exp\big[-((r-r_2)/a_2)^2\big], \tag{5.2}$$

where B_1 and B_2 determine the peak field strengths, a_1 and a_2 set the radial width of the field, and δl_1 and δl_2 represent the thickness. This field profile is based on the addition of two Gaussian ellipsoidal field structures described in Section 3.4 and in Kugland *et al.* [118]. The radial position of the peak of the second field structure is given by r_2. While only magnetic fields are considered here, the second field structure could be interpreted as a radial electric field near the edge of the expanding plasma.

The spoke-like features are most prevalent in the CH target results. A potential source is enhanced filamentation of the relativistic electron currents in the insulating target [167,168]. To approximate the combined effect of a number of filamentary field structures on the proton image, additional fields were superimposed on to the profile described by equation (5.2). The filament structures were also based on the Gaussian ellipsoidal field (the same functional form as B_1 in equation (5.2)), and were positioned radially, evenly spaced surrounding the center.

The results from the forward-scattering are summarized in Figure 5.8. Experimental proton images from copper and CH are compared in (a) and (b), respectively. The proton energies were (a) 29.4 MeV for copper and (b) 39.9 MeV for CH. Figure 5.8(c) shows the synthetic proton image generated using equation (5.2) and the following parameters: $B_1 =$ 200 MG, $a_1 = 250$ μm, $B_2 = 5$ MG, $r_2 = 700$ μm, $a_2 = 0.25 r_0$, and $\delta l_1 = \delta l_2 = 10$ μm. The corresponding path-integrated field profile is shown in Figure 5.8(e). Synthetic images were produced using 35 MeV protons. To account for the finite proton source size and the effect of scattering in the target, the synthetic images are smoothed using a 50 μm full-width-half-maximum (FWHM) Gaussian source.

Spoke-like features can be produced in the synthetic proton image by adding "filaments"

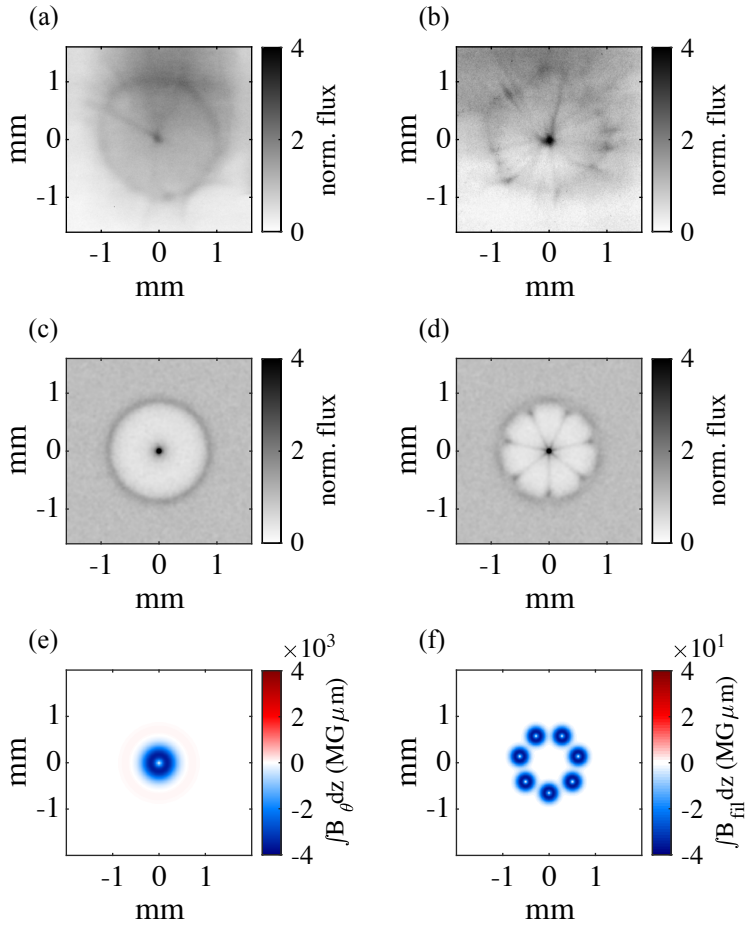

Figure 5.8: (a-b) Proton images of magnetic field generated on copper (a) or plastic (b) targets. The relative timing is approximately 11 to 12 ps after t_0. (c-d) Synthetic proton images generated with the forward-scattering approach demonstrating the formation of spoke-like features. (e) The path-integrated magnetic field profile used to generate the images. (f) "Filament" field structures added to the profile in (e) to produce spoke-like features in (d).

with the following parameters: $B_f = 0.01B_1$, $a_f = 140$ μm, and $\delta l_f = \delta l_1$. The resulting synthetic proton image and "filament" fields are shown in Figure 5.8(d) and (f), respectively. Note that the peak of the filament fields is only 1% of the overall peak field strength, and the colorbar in Figure 5.8(f) has been adjusted.

Despite the use of reasonable values for field strength and spatial profile, this approach does not yield quantitative analysis of the proton images. However, key features can be reproduced, including the ring-dot caustic structure. Relatively modest azimuthal perturbations introduced by the addition "filament" structures causes clear spoke-like features in the

proton image. Such azimuthal perturbations are likely caused by filamentation of relativistic electron currents due to resistivity gradients [169] or Weibel-like instabilities [170].

Due to the link between magnetic fields and the sheath electric field (equation (5.1)), we can draw upon the extensive exploration of target conditions for TNSA in order to illuminate how material properties might impact magnetic field generation. Experimental and computation studies of electron transport in laser-solid interactions have identified various mechanisms driving filamentation of the relativistic electron beam which can essentially be broken into a few categories: resistive filamentation in the dense bulk target [167–169,171,172], ionization front instabilities [173,174], Weibel-like filamentation in low density plasma present on the target surface [141,142,170,175–177], or a combination of these mechanisms [162,178]. Typically, filamentary instabilities are more prevalent in insulating targets [167, 174]. The characteristic growth timescales for these mechanisms range from a few femtoseconds for Weibel-like instabilities [141], to 10s or 100s of femtoseconds for resistive instabilities in insulating or conducting targets, respectively [168, 172].

In this experiment the laser pulse duration was 10 ps, which is many times the characteristic time scales for all of the aforementioned instabilities. Therefore, we are likely observing a dynamic combination of these mechanisms. Initially, the resistive instability will grow 10 to 100 times faster in the insulating (CH) targets. During the multipicosecond drive, the targets will begin to expand, producing conditions susceptible to Weibel-like filamentation. The amount of target expansion during the long rise time of the laser pulse can be estimated based on the laser intensity, pulse duration and an assumed hot electron temperature [70] (see also Chapter 4). No matter the material, low density plasma with scale lengths ($|\partial n_e|/n_e$) of 10s of microns can extend from the target surface. The combination of these two instabilities likely explains why we observe some evidence of filamentary fields in all materials ("spokes", and disruption of the ring feature), while they appear most prevalent in the insulating CH target.

5.4.1 Simulations of field generation mechanism

Full 3D simulations of the experiment with a 10 ps laser pulse and mm spatial scales would be prohibitively computationally expensive. While some 3D effects like filamentation will not be reproduced, 2D simulations using the state-of-the-art, fully relativistic PIC code OSIRIS [123, 124] allow us to test the fundamental physics of magnetic field generation, and probe the origins of features observed in the proton images. Two classes of simulation were performed. First, simulations with cylindrical coordinates were used to examine the field generation mechanism and test the simple theoretical prediction of equation (5.1). Next, 2D Cartesian simulations of overdense laser-plasma interactions examine the impact of preformed plasma on field generation and transport.

In an ideal case, magnetic field generation by a high intensity laser pulse should be azimuthally symmetric around the laser focal spot. As the fields expand, the strength should decrease following a $1/r$ dependence [9]. This radial behavior cannot be accurately captured with 2D Cartesian simulations. Therefore, r-z cylindrical coordinates simulations were used to examine the field generation and evolution. A laser field cannot be used with the cylindrical geometry in OSIRIS, so a simplified model was developed which replaces the laser-solid interaction with an impulse of hot electrons. Initially, the population of hot electrons has a Gaussian density profile described by

$$n(r,z) = n_0 \exp\Big[-\Big(r/r_0\Big)^2\Big]\exp\Big[-\Big((z-z_0)/r_0\Big)^2\Big],$$

where n_0 is the peak hot electron density (normalized to n_c), r_0 is the characteristic radius, and z_0 is the position of the target surface. For this set of simulations, the domain was 100 μm $\times$ 100 μm, resolved by 3000 $\times$ 3000 cells. The target was a fully ionized electron-proton plasma slab with a thickness of 10 μm and a uniform electron temperature of 5 keV. The target density was 10 n_c, the critical density, and an exponential plasma profile extended from each surface with a 0.5 μm scale length. Figure 5.9(a) shows the initial electron density

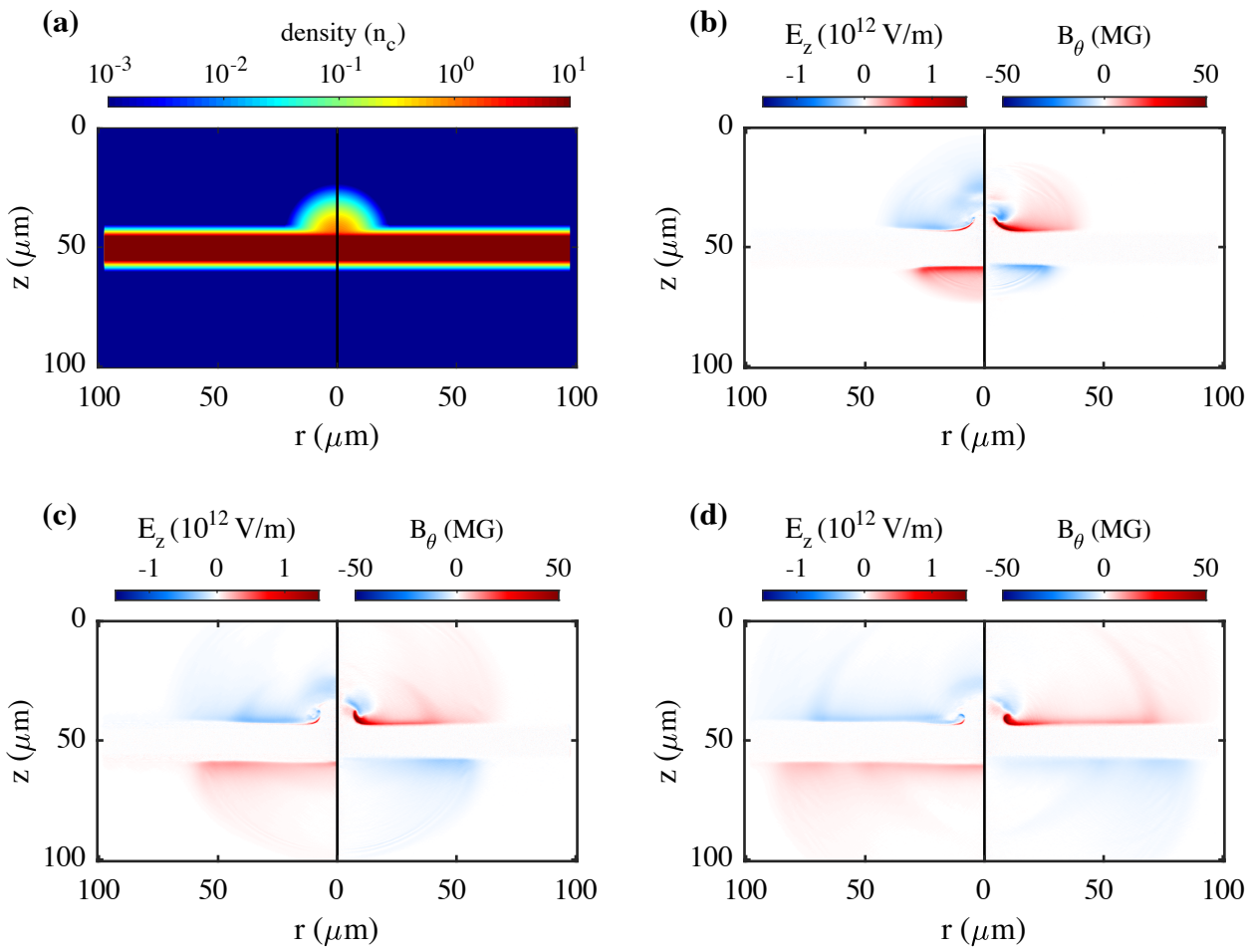

Figure 5.9: (a) Initial electron density profile for the field generation simulations. (b-d) A time series of the electric and magnetic field evolution at the times 98, 196, and 294 fs.

profile. The hot electron population r_0 was set to 8.4 μm for a full-width-half-max of $\sim$10 μm.

As the system evolves, fast electron expansion generates a sheath electric field and azimuthal magnetic field along both surfaces of the target. An example time series of the field evolution is shown in Figure 5.9(b-d). In each panel, the sheath electric field is plotted on the left and the azimuthal magnetic field is on the right. The color scales are set such that $E_{\max} = c\,B_{\max}$. Driven by the relativistic electrons, the fields expand along the surface with velocities near the speed of light.

While holding the other fixed at 1, the hot electron density or temperature were scanned between normalized values of 0.5, 1, 2, 5, and 10, where temperature is normalized to the

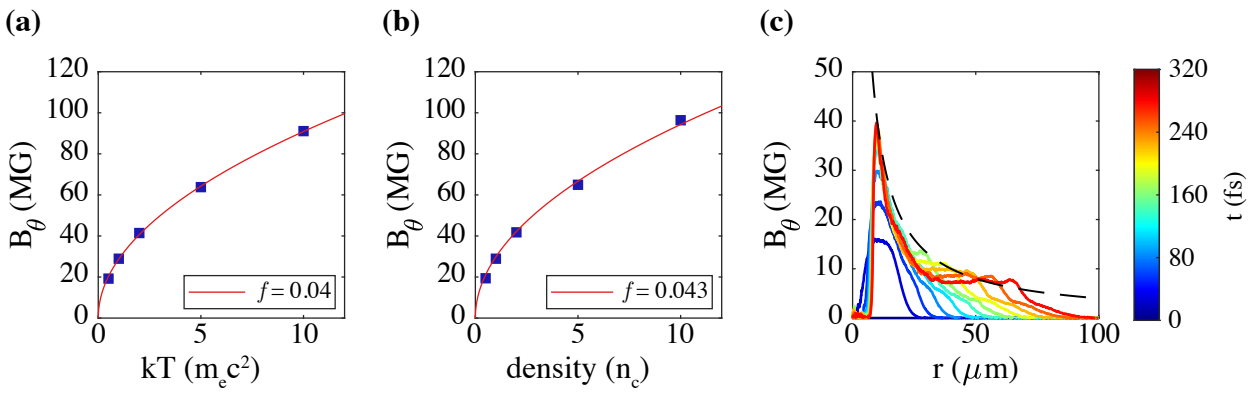

Figure 5.10: (a-b) The results from the parameter scan are fit with equation 5.3. (c) Line-outs along the front target surface show that the temporal evolution of the surface magnetic field follows a $1/r$ dependence (dashed line).

electron rest-mass energy, $m_e c^2$ and density is normalized to the critical density, n_c. The hot electron population is defined by a relativistic Maxwell-Jüttner distribution. In each simulation, the magnetic field strength at a radius of $2r_0$ was monitored and the maximum value was recorded. The results of the parameter scan are summarized in Figure 5.10(a) and (b), where the maximum magnetic field is plotted as a function of hot electron temperature (a) or density (b). For each parameter scan, the results were fit using an ordinary least-squares approach with a modified form of equation (5.1),

$$B_0 = \sqrt{2\mu_0 f n_e k_B T_e}, \tag{5.3}$$

where the fitting factor f is introduced. Physically, f represents an escaped fraction, or ratio between the density of electrons driving the field generation and the peak density. Excellent agreement is found between the results and the simple predictions with $f \approx 0.04$. In addition, line-outs of the front surface field at different times in the evolution are plotted in Figure 5.10(c). The line-outs represent the average field within a 2 μm thick region along the front target surface. As predicted by Schumaker *et al.*, the field evolution closely follows a $1/r$ dependence (dashed line).

This simplified simulation model accurately captures key aspects of laser-driven field

generation and evolution, in particular the connection between the strong sheath electric field and the azimuthal magnetic field. While neglecting the laser-plasma interaction and complications introduced by 3D effects such as instabilities, these simulations confirm the fundamental mechanism and scaling of high intensity laser-driven magnetic field generation.

5.4.2 Impact of preformed plasma

The native prepulse of a high intensity laser can propagate ahead of the main pulse and ablate the surface the solid target, producing a low density preformed plasma. Rather than interacting with a sharp solid interface, the main laser pulse will first propagate through, and interact with, low density plasma that extends from the solid surface with an approximately exponential profile. The length of that preformed plasma can dramatically impact the laser interaction [179–181]. For example, laser absorption can be enhanced due to the low density plasma leading to more efficient coupling of energy to the hot electrons. As discussed above, magnetic field generation is driven by hot electrons. In order to explore how details of the laser-plasma interaction can impact magnetic field generation, we simulated the interaction of a high intensity pulse with different preformed plasma scale lengths.

Again, computational expense prohibited full-scale simulations of the 10 ps interaction used in the experiment. However, the simple model presented above indicates that key aspects of field evolution can be examined using scaled down simulations (in both space and time). In normalized units, the simulation domain was 500×1500 $(c/\omega_0)^2$ (approximately 84×252 $(\mu m)^2$) resolved by 5000×7500 cells. The simulated laser pulse had a duration of 1790.1 $1/\omega_0$ (1 ps), a normalized vector potential (a_0) of 5, and was focused to a Gaussian spot with a beam waist, w_L, of 50.68 (c/ω_0) (8.5 μm) for a 10 μm FWHM. The laser pulse propagates in the x-direction and interacts at normal incidence with a fully ionized electron-proton slab target with a peak density of $100n_c$, where n_c is the critical density for 1 μm light. For each species, 100 particles-per-cell and cubic interpolation was used. The target was 60 c/ω_0 ($\sim$10 μm) thick. On the front surface (laser-side), an exponential preformed

plasma had a scale length of either 1/4, 1/2, 1 or 2 λ_0, where λ_0 is the laser wavelength. The preformed plasma had a Gaussian transverse profile with a width matched to the laser focal spot, with the exception of the 2 λ_0 case where the width was increased to $2w_L$.

Figure 5.11(a-d) show the 2D azimuthal magnetic field profile measured approximately 100 fs after the peak of the laser pulse (t_{peak}) for each scale length. In all cases, fields have formed on both the front and rear surface of the target. A large enhancement of the field strength is observed as the scale length is increased above $1/4\lambda_0$.

Outside of the focal region, the fields are generated by the expanding fast electrons and sheath field. However, as the scale length increases, an oppositely oriented field is generated within the focal region as the laser pulse bores a channel into the dense target and accelerates an axial electron current [46, 182]. The relative strength of the channel magnetic field and the surface fields is sensitive to the scale length of the exponential preformed plasma. Line-outs of the magnetic field profile taken at $2w_L$ (surface field) and $1/2w_L$ (channel field) are compared in Figure 5.11 (d) and (e). A $1\lambda_0$ scale length yielded the strongest surface field with a peak around 100 MG. The strength of the oppositely oriented channel field enhances as the scale length is increased from 1 to $2\lambda_0$. No channel field is observed for scale lengths $\leq 1/2\lambda_0$.

From the simple theoretical model of field generation, the peak strength is proportional to $\sqrt{fI_L/c}$. The intensity was constant across this set of simulations, so the preformed plasma is primarily impacting f. Figure 5.11(f) shows the integrated electron spectra within the simulation domain measured 100 fs after the peak of the pulse for each scale length. While the hot electron temperatures were similar in each case (measured from the slope of distribution tail to be around 1 MeV), the hot electron number, and therefore density, significantly increases as the scale length rises from $1/4\lambda_0$. However, the theoretical model does not account for laser channeling. Despite the enhanced coupling observed for a $2\lambda_0$, the surface field is weaker. Instead, the laser drives stronger axial currents and the channel field increases.

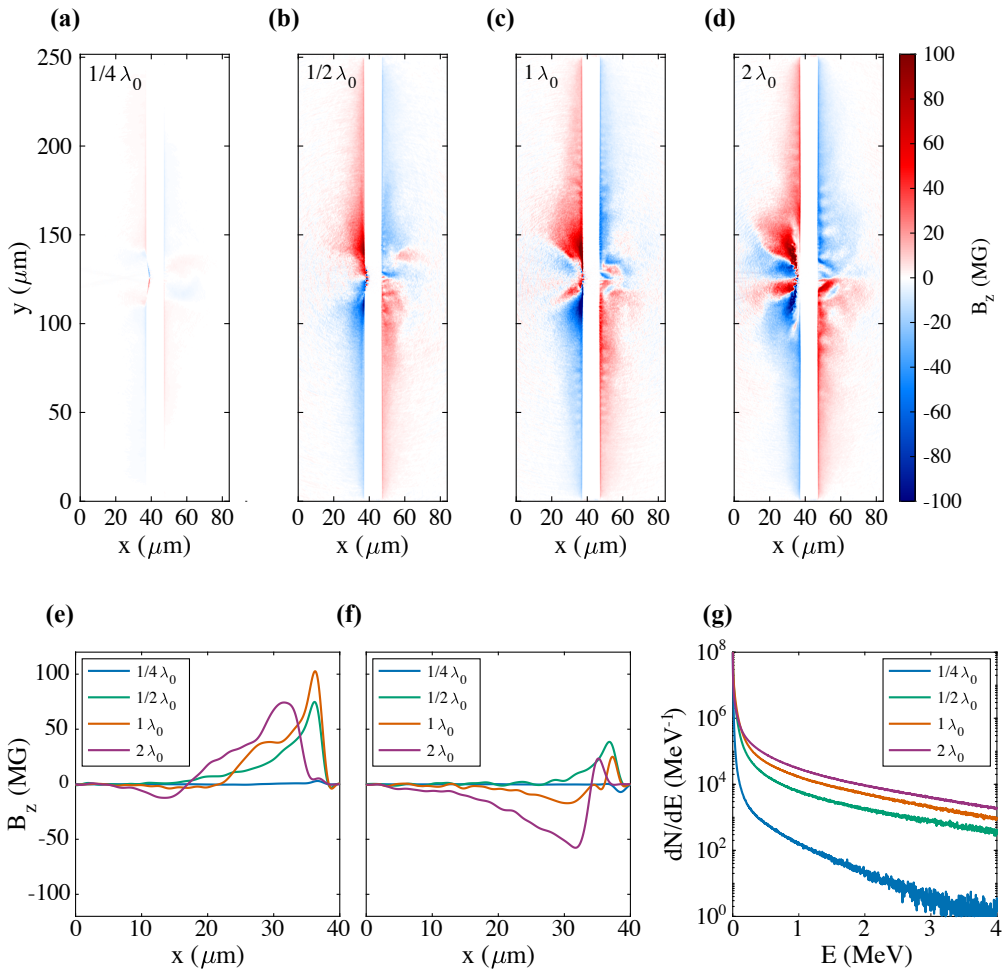

Figure 5.11: (a-d) Magnetic field profiles measured 100 fs after the peak of the laser pulse for preformed plasma scale lengths of 1/4, 1/2, 1, and $2\lambda_0$, respectively. Line-outs through the profiles taken at $2w_L$ and $1/2w_L$ are plotted in (e) and (f). Electron spectra 100 fs after the peak of the laser pulse are compared in (g).

These simulations demonstrate how enhanced coupling can drive stronger fields, and also reveals that laser channeling can significantly alter the spatial profile and peak strength. In addition, evidence of filamentary field structures can be seen in the 2D field profiles (Figure 5.11(a-d)). As discussed in Chapter 4, these field structures are caused by filamentation of fast electron currents. Such filamentary fields are enhanced by the presence of low density preformed plasma which would be expected to form during the long rise time of the 10 ps pulsed used experimentally.

Finally, Figure 5.12 shows the impact of preformed plasma scale length on the magneti-

zation parameter, $\sigma_{cold} = B^2/\mu_0 n_e m_e c^2$. In general, the evolution can be broken into three stages during the picosecond interaction. Initially, as the laser intensity rises ($t \approx 0.7\ t_{peak}$), a relatively low density of hot electrons begin driving field generation along the surface resulting in large σ_{cold} (shown in the top row of Figure 5.12). Near t_{peak}, the field strength continues to grow, but expansion of the bulk target increases the local density in high field regions, reducing σ_{cold}. At later time ($t = 1.5\ t_{peak}$, shown in the bottom row of Figure 5.12), continued target expansion pushes strong fields into lower density plasma, once again resulting in regions of where $\sigma_{cold} > 1$. Overall, the presence of low density preformed plasma enhances σ_{cold}, yielding regions where the magnetic energy density exceeds the electron rest mass energy density, and potentially enabling laboratory studies of highly energetic magnetized interactions, such as relativistic reconnection.

5.5 Conclusion

These experiments and simulations demonstrate that target material can have a profound effect on the topology of magnetic fields generated in high power laser-solid interactions. At moderate intensities, radiation transport in mid-Z targets drives double ablation front structures, initiating multiple regions of Biermann battery field generation. The temperature "plateau" and relatively high magnetization near the electron ablation front form a transport barrier. These results serve as a good benchmark for extended radiation-MHD simulation tools, which are an essential part of ICF and HED research. Future experiments could explore high Z targets and make higher resolution measurements of the time evolution.

With high intensity pulses, filamentation of relativistic electron currents is enhanced in insulating, low-Z targets. The filamentation mechanism is likely a combination of resistive and Weibel-like instabilities during the multipicosecond drive. While full scale 3D simulations are prohibitively computationally intensive, simplified 2D simulations capture key aspects of the field generation mechanism. Using a simplified model and neglecting the laser-plasma

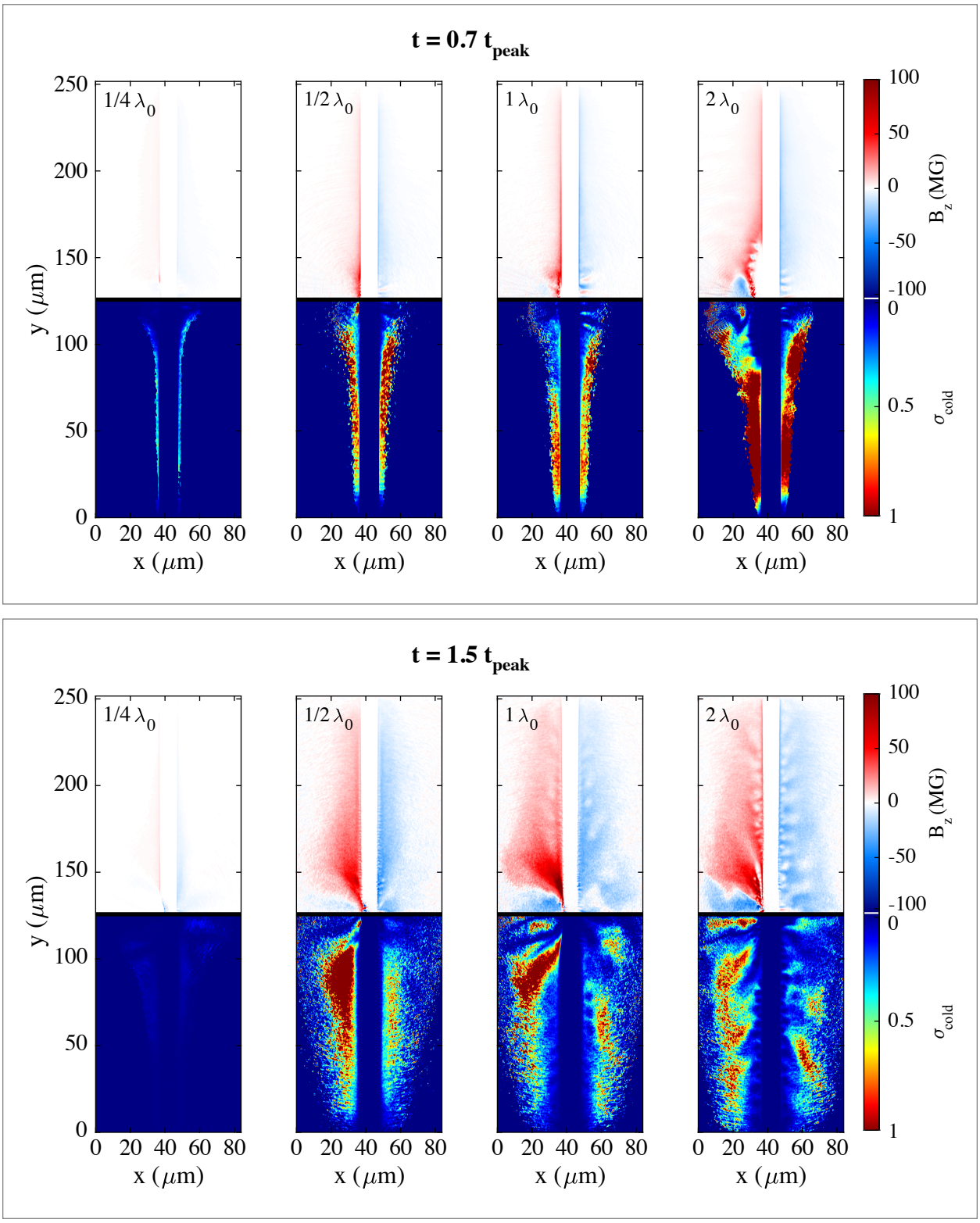

Figure 5.12: The effect of performed plasma scale length on the evolution of the magnetization, σ_{cold}, at two different times during the high intensity interaction.

interactions, cylindrically symmetric simulations illustrate the link between the hot electron population, strong sheath field formation and magnetic field generation. In addition, these simulations validate a simple theoretical prediction and scaling argument for the peak field strength.

Simulations of the laser-solid interactions investigate the role of preformed plasma field generation. As the preformed plasma scale length is increased, the coupling of laser energy into hot electrons is enhanced. In general, this yields stronger fields and higher magnetizations (σ_{cold}). However, as the scale length increases beyond $1\lambda_0$, laser channeling begins to dominate and strong channel fields form within the focal region. In addition, based on the simulation results shown here and in Chapter 4, preformed plasma expansion enhances filamentary field formation. Such filamentary fields likely contribute to the spoke-like features observed in the proton images.

CHAPTER 6

Proton Radiography of Highly Asymmetric Laser-Driven Magnetic Interactions

The work presented here combines elements previous chapters by using proton imaging to diagnose a highly asymmetric magnetic interaction. In experiments performed at the OMEGA EP laser facility at the Laboratory for Laser Energetics, a typical laser-driven magnetic reconnection geometry was adapted such that one high intensity pulse ($I \approx 10^{19}$ Wcm^{-2}) was focused alongside a moderate intensity UV long pulse ($I \approx 10^{14}$ Wcm^{-2}) on foil targets. First, the long pulse ablates a region of the target and misaligned temperature and density gradients in the plasma plume generate an azimuthal magnetic field via the Biermann battery mechanism (as described in Chapter 5). After the Biermann field develops, the high intensity pulse arrives on target and produces a relativistic, highly magnetized plasma ($\sigma_{cold} = \frac{B^2}{\mu_0 n_e m_e c^2} \geq 1$) which sweeps across the target surface with velocities near the speed of light. Proton radiography captures the dynamic interaction of the strong, impulsive magnetic field generated by the high intensity pulse and the relatively slowly evolving Biermann battery fields. Quantitative measurements of the magnetic field dynamics will be discussed, as well as 3D particle-in-cell simulation results, which show signatures of a magnetized interaction potentially indicative of bow-shock formation and asymmetric magnetic reconnection.

6.1 Introduction

Strong magnetic fields generated in laser-produced plasmas enable dedicated laboratory exploration of magnetized HED and astrophysical phenomena [6]. In particular, numerous experiments and simulations have been carried out to study magnetic reconnection driven by high power laser pulses with nanosecond durations [25,33–39,41,42,150,183] As discussed in the previous chapter, moderate intensity ($I_L \approx 10^{14}$ Wcm^{-2}), nanosecond laser pulses ablate the surface of solid targets and in the resulting plasma plume there is a misalignment of temperature and density gradients. This generates a strong azimuthal magnetic field due to the Biermann battery mechanism ($\frac{dB}{dt} = \frac{k_B}{en_e}\nabla T_e \times \nabla n_e$). The self-generated fields are carried away from the laser spot by the bulk plasma flow at speeds $\approx c_s$. When two such lasers are fired side-by-side, opposing magnetic fields are driven together in the midplane, establishing a magnetic reconnection geometry. Recent computational work simulated the full 3D field interaction, demonstrating that the Biermann battery effect plays an important role in both generating the fields and mediating the reconnection [184].

The magnetic fields are confined to relatively high density regions of the hot plasmas and field strengths are typically on the order of 1 MG [8]. Therefore the plasma β, the ratio of the plasma pressure to the magnetic pressure ($\beta = nk_BT/(B^2/2\mu_0)$), is high ($\mathcal{O}10-100$). While this limits how well laboratory observations scale to astrophysical systems (typically $\beta \leq 1$ in the solar corona), there is still much that can be learned about magnetic reconnection in HED conditions, such as the importance of two-fluid effects and magnetic island formation [33]. Controlled high power laser experiments can help illuminate the fine details of the dynamic reconnection physics.

Recent experiments successfully extended laser-driven magnetic reconnection to high intensities ($I_L \approx 10^{18} - 10^{19}$ Wcm^{-2}) [44, 45]. At these intensities, the laser accelerates electrons to relativistic velocities and the rapid expansion along the surface establishes a time-varying, target-normal sheath electric field and generates an azimuthal magnetic field surrounding the focal spot. In contrast to the nanosecond pulse experiments described above,

the magnetic fields generated by the short, ultra-high intensity pulses are orders of magnitude stronger ($\mathcal{O}100MG$) and are driven together by relativistic electrons at velocities near the speed of light [9, 44]. Indeed, the magnetic fields are so strong that these high intensity experiments approached the relativistic reconnection regime, where the magnetic energy density of the reconnecting field exceeds rest mass energy density of the surrounding plasma ($\sigma_{cold} = B^2/(\mu_0 n_e m_e c^2) > 1$). Relativistic reconnection is thought to play a key role in powering extremely energetic astrophysical phenomena such as gamma ray bursts (GRBs), relativistic pulsar wind emissions and jets from active galactic nuclei [28–31, 96].

In many astrophysical systems there are significant asymmetries between the global parameters of the interacting plasmas. For example, during the interaction of the solar wind (SW) and Earth's magnetosphere (MS) at the magnetopause, $B_{MS}/B_{SW} \sim 7$, $n_{MS}/n_{SW} \sim 1.4$, and $T_{MS}/T_{SW} \sim 30$ [3]. A number of experiments [185–189] and simulations [190] have explored laboratory analogues of plasmas interacting with magnetized obstacles with a particular emphasis on elucidating mechanisms governing bow shock formation and particle energization.

The laser-driven reconnection geometry was used to study asymmetric magnetic reconnection by varying the relative timing of two nanosecond pulses [40]. The result was modest asymmetries between the temperatures, densities, and characteristic sizes of the two plasmas, while the magnetic field strengths and inflow velocities were similar. It was found that the field annihilation was mediated by collisionless/two-fluid effects, while the reconnection rate was primarily determined by the strong inflow velocities. For the parameter range accessed in that experiment, the reconnection rate was seemingly insensitive to the global asymmetries.

In this chapter, the laser-driven reconnection geometry was further adapted to produce a highly asymmetric interaction. Rather than firing two identical laser pulses side-by-side, experiments were conducted at the OMEGA EP laser facility to study a reconnection geometry established by focusing a short, high intensity pulse alongside a moderate intensity,

nanosecond pulse on solid targets. Due to the strong asymmetries in expansion velocities, the plasma produced by the moderate intensity pulse is quasi-stationary during the interaction. Proton radiography captures the field dynamics as the impulsive magnetic field produced by the high intensity pulse is driven across the target to interact with the Biermann battery fields produced by the moderate intensity pulse. Quantitative measurements of the magnetic field demonstrate modification of the Biermann field profile due to the interaction. A simplified 3D particle-in-cell model shows evidence of magnetic field pile-up and annihilation, as well as density compression and electric field generation at the interface of the two plasmas. Signatures of such field dynamics observed in the experimental proton images.

6.2 Experimental methods

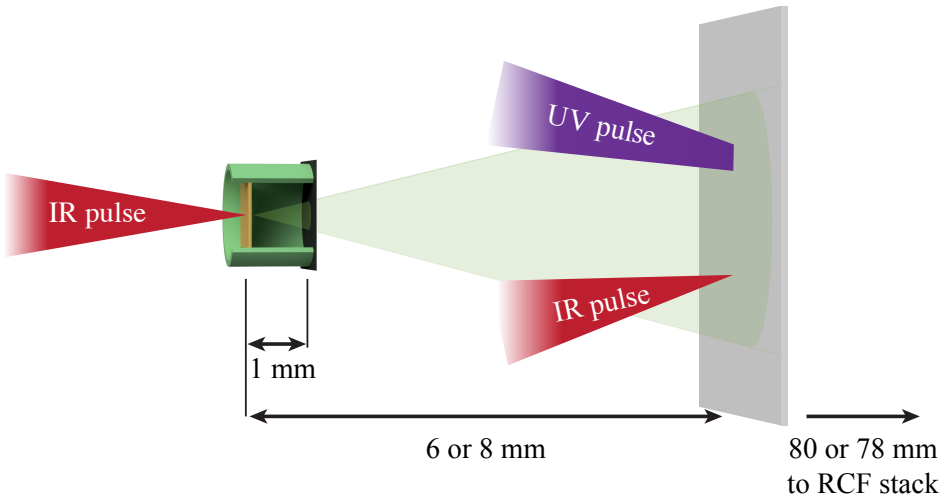

Figure 6.1: A schematic of the highly asymmetric reconnection geometry on OMEGA EP. First the UV long pulse establishes a slowly evolving ablative plasma with Biermann fields. Next the high intensity IR short pulse drives an impulsive magnetic field. A second short pulse accelerates a proton beam to diagnose the electric and magnetic field dynamics associated with the interaction.

Experiments were performed with the OMEGA EP laser system at the University of Rochester's Laboratory for Laser Energetics with a similar setup to Chapter 5. Instead of using either the high intensity or moderate intensity pulse independently, the two lasers are

fired together. The moderate intensity interactions were driven by a long pulse beam with a 351 nm wavelength, 1250 J of energy and 1 ns square temporal profile was focused to an 820 μm diameter super-Gaussian spot with an intensity approximately 2×10^{14} Wcm^{-2}. High intensity interactions were driven a 500 J, 10 ps infrared (IR) pulse was focused on target by an $f/1.8$ off-axis parabolic mirror to intensities of $5 \pm 1 \times 10^{19}$ Wcm^{-2}. The focal spot separation was 1.25 mm and the relative timing was set such that the moderate intensity interaction had evolved for 750 ps before the high intensity pulse arrived on target. These laser conditions were characterized independently in Chapter 5. Thin foil targets were either 50 μm thick CH plastic, 25 μm thick copper, or 25 μm thick aluminum.

As in Chapter 5, protons accelerated by the target normal sheath acceleration (TNSA) mechanism [50–53] were used to image the magnetic field dynamics of the asymmetric reconnection geometry. The second OMEGA EP high intensity laser with 300 J in a 0.7 ps pulse was focused to intensities exceeding 10^{20} Wcm^{-2} on to 1×1 mm^2 foils. The proton source foils, either 50 μm thick copper or 20 μm thick gold, were housed in a plastic tube capped by a 5 μm tantalum foil in order to protect them from x-ray preheat and plasma generated during the main interaction. After passing through the main interaction, the proton beams were detected by stacks of radiochromic film (RCF). The details of the RCF stack can be found in Appendix C. The proton source foil was positioned either 6 or 8 mm from the main interaction. After passing through the main target, protons traveled 80 or 78 mm to the RCF stack, resulting in magnifications of 14.3 or 10.8.

During transit between the source and main interaction, time-of-flight dispersion of the broad proton spectrum makes possible single shot, time-resolved measurements of ultrafast dynamics with picosecond temporal resolution (as shown in references [10] and [60], for example). The relative timing between laser pulses could be adjusted in order to measure the full dynamics of more slowly evolving features associated with the moderate intensity interactions. Based on the RCF stack design, the relative time-of-flight between RCF layers was 3 to 6 ps.

6.3 Experimental results

A single-shot measurement of the field dynamics on a 25 μm copper foil is shown in Figure 6.2. In each image, the proton flux has been normalized by the mean signal. At t_0, first evidence of the high intensity interaction appears. The ring structures associated with the moderate intensity, long pulse produced plasma are already present in the upper half of image. As time progresses, fast electrons sweep across both the front and rear surfaces of the target. After 12 ps, the two plasmas begin interacting as fast electrons drive up into the long pulse plasma and a strong enhancement of proton signal forms at the interface. In the subsequent time steps, evidence of a bow shock-like feature and compression of the long pulse fields appear in the proton images. The rose petal-like features surrounding high intensity spot, particularly evident at later-times (i.e., lower energies), are due to "self-emitted" protons accelerated from the main interaction foil. This non-uniform background signal increases the difficulty of accurate interpretation of the proton images, though key features of the asymmetric interaction are still observable.

The proton energies for this series ranged from 18 MeV (t_0 + 27 ps) to 33 MeV (t_0). Scattering in the relatively high-Z target reduces the resolution of the image. Following the approach used in [45], SRIM [113, 114] can be used to make estimates of the average scattering angle for protons passing through the target. The results of the scattering analysis are summarized in Appendix D. From the scattering angle, the resolution can be estimated as $\approx 2\theta_s L/M$, where L is the distance from the target to the detector and M is the image magnification. For 30 MeV protons, the copper target gives a 5 milliradian scattering angle, blurring the image to result in a $\sim$50 μm resolution. The blurring is expected to be worse for lower energies.

Higher resolution can be achieved by switching to lower-Z materials. The resolution limited by scattering is improved to $\sim$35 μm with 50 μm thick aluminum, and $\sim$6 μm with 50 μm thick plastic, which will be a small contribution to the intrinsic resolution of TNSA proton beams ($\sim 10-20$ μm [57]). Proton imaging results from shots on each target type are

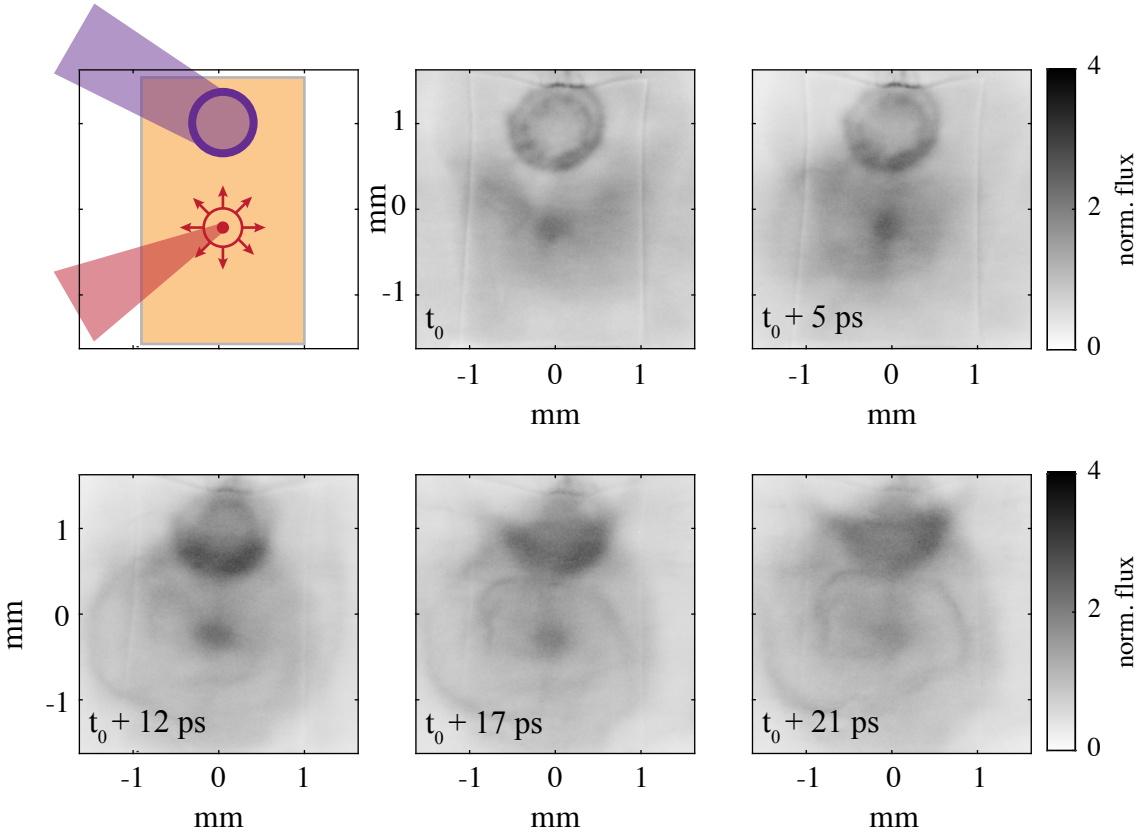

Figure 6.2: A single-shot time series of proton images captures the dynamic interaction between the the long pulse produced plasma and hot electrons driven by the high intensity pulse. The geometry is shown schematically at the top left. As the long pulse interacts in the upper half of the foil, the short pulse drives a rapid expansion from the lower half. Note: "self-emitted" protons from the main interaction contribute a non-uniform background signal to the image.

compared in Figure 6.3. The images have been cropped to emphasize modifications to the long pulse field structure driven by the hot electrons and accompanying magnetic field. Each represent a single-shot measurement of the dynamics, and similar times in the evolution were selected from the image stacks. The proton energies shown for each material (from left to right) are: copper = [29.4, 24.9, 22.2] MeV, aluminum = [32.5, 28.6, 26.0] MeV, and plastic = [30.4, 27.1, 24.8] MeV.

As discussed in Chapter 5, the target material affects the magnetic field topology, altering the initial conditions and potentially limiting comparisons. However, we observe common dynamics across all target materials. In particular, we observe: (1) compression of the ring feature and (2) the formation of a cone-shaped feature at the interface of the two plasmas. It should be noted that the long pulse feature was located near the edge of both the target and film for the copper target data. Larger targets and lower magnification were used for the aluminum and CH data.

Quantitative measurements of the magnetic fields can be extracted by inverting the relative flux in the proton images. One of the primary challenges of quantitative proton image inversion is accurate determination of the undisturbed proton beam profile. Due to the limited shot availability and shot-to-shot fluctuations in the proton beam profile, reference shots are impractical. As a result, the undisturbed beam profile must be inferred from the proton image itself. This is typically accomplished by using Fourier low-pass filtering to remove high frequency components of the image (usually associated with field structures), and leaving behind a smooth beam profile [120, 121]. Another approach masked high intensity portions of the image and fit the remainder with a 2D polynomial [45]. Here, the undisturbed distribution, I_0, is inferred by first by applying a Gaussian low-pass Fourier filter to smooth the proton image, I. Then, concentric super-Gaussian masks are used to blend the filtered image with the original such that $I/I_0 \approx 1$ near the edges and in the center of Biermann field feature. This amounts to assuming the fields should fall to zero at both the center and far from the edge of the long pulse produced plasma, which is likely

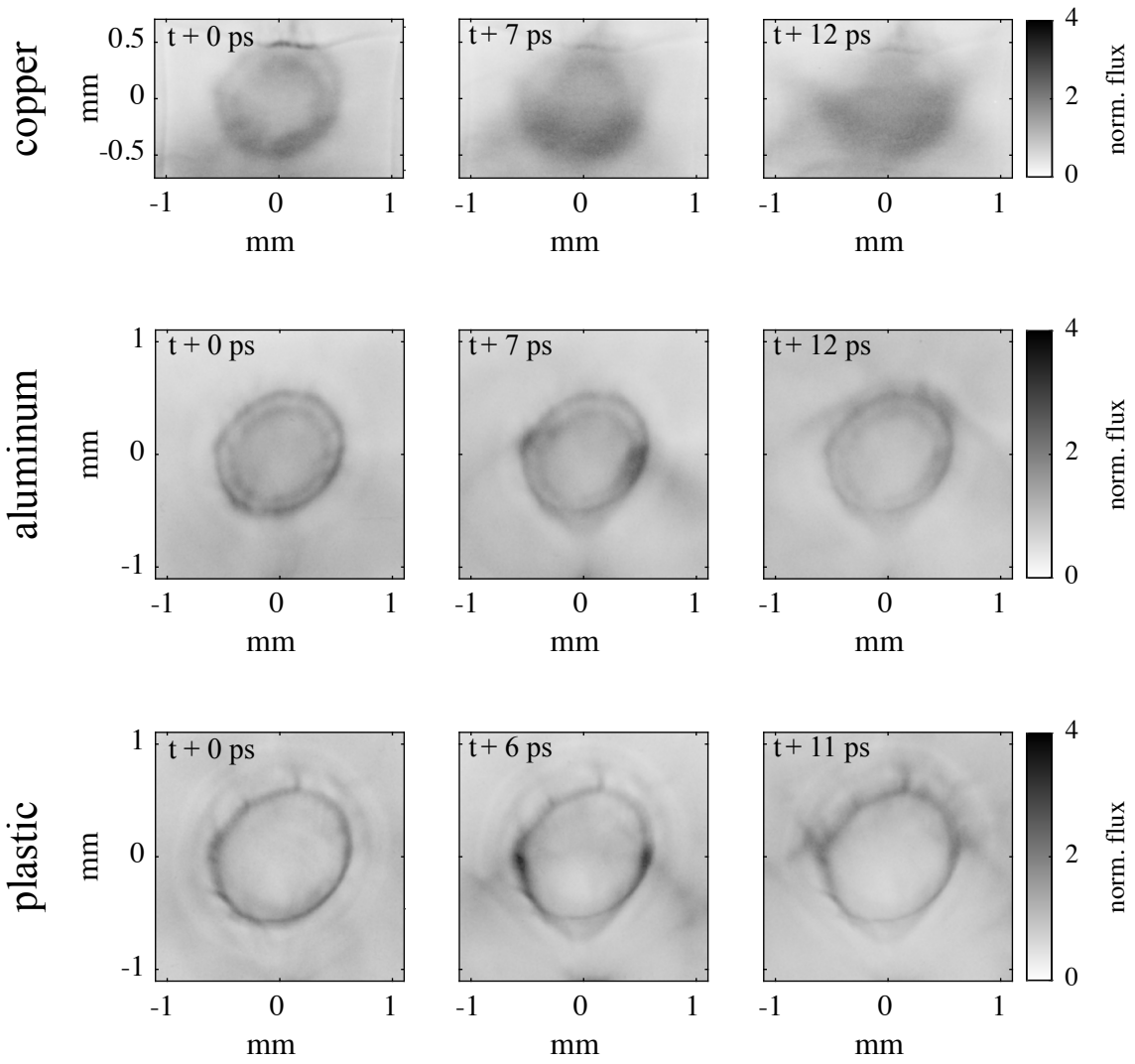

Figure 6.3: Proton images of the asymmetric interaction dynamics on either copper, aluminum, or plastic (CH) targets. Again, the proton flux has been normalized by the mean signal.

valid before the high intensity pulse arrives on target. However, this method of producing reference images will not accurately capture the fields driven by the short pulse, and instead emphasizes modifications to the Biermann battery field.

Proton images normalized by the inferred reference profiles for the CH target interaction are shown in the top row Figure 6.4. The resulting path-integrated magnetic field maps plotted in the bottom row were produced using the 2D Cartesian inversion method described in Chapter 3.4. Uncertainties in determining the precise undisturbed proton distribution (I_0) can lead to large errors in quantitative magnetic field measurement (as large as 20 MGμm). However, the key changes in the field structure are correlated to clear qualitative differences in the proton images.

Before the plasmas interact, at $t = \mathrm{t}_0$, the Biermann battery magnetic field profile closely resembles the results presented in Chapter 5 and published by Gao *et al.* [8]. During the interaction, the cone-shaped feature at the interface appears to correspond to regions of enhanced field which form on either side of the interaction region. As the system evolves, the field maps suggest that the Biermann field reconfigured. Strong fields are driven out of the interaction region (upward, in the image), and a weaker field is left behind. In addition, magnetic null features can be observed which are pushed along the edge of the long pulse plasma. Black arrows in the Figure 6.4 indicate the strong field regions and the magnetic nulls.

For each material, clear qualitative changes to the Biermann magnetic field structure are driven by the high intensity laser-produced plasma. In particular, the cone-shaped feature and corresponding changes to the magnetic field profile are potentially signatures of asymmetric reconnection or collisionless bow-shock formation.

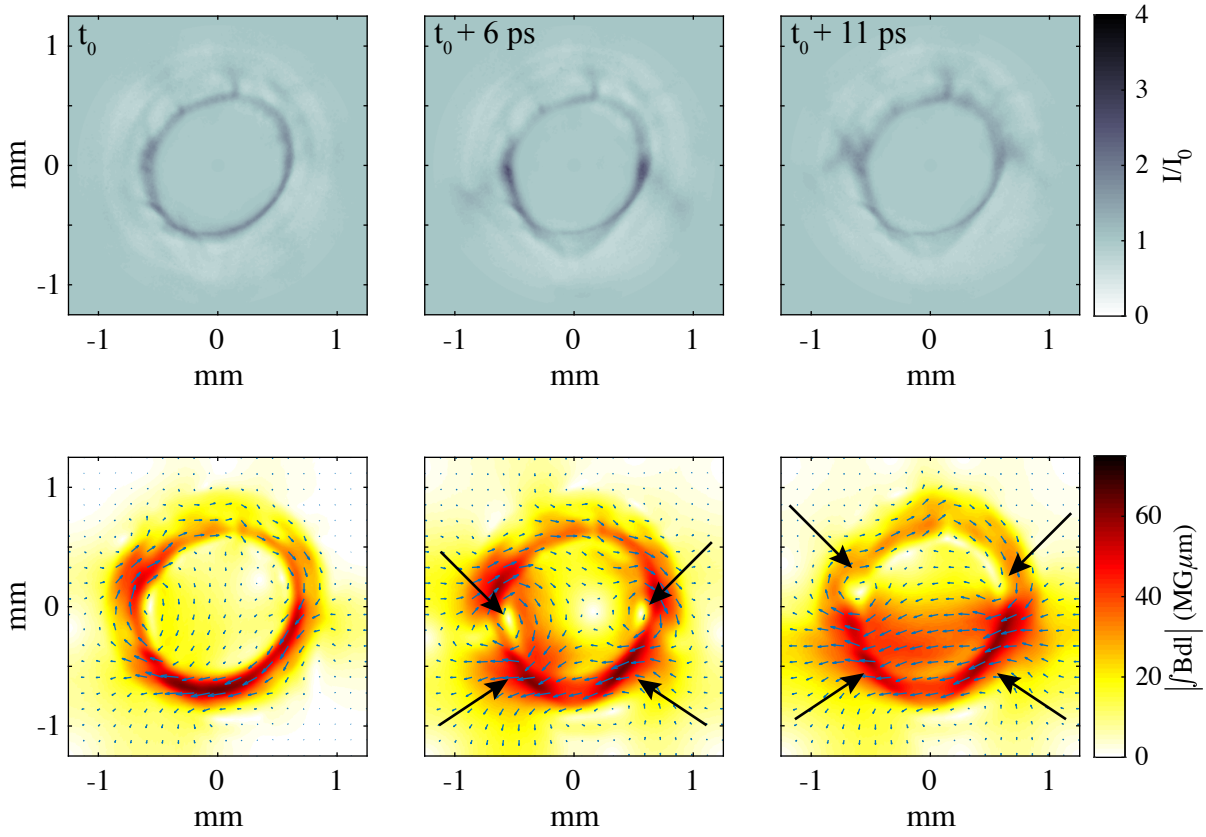

Figure 6.4: For the CH target interaction, inversion of normalized proton images results in quantitative measurements of the path-integrated magnetic field. While uncertainty in determining the undisturbed proton distribution can lead to significant errors the measured field strength, clear qualitative differences can be observed in both the images and field maps. Enhanced field regions and field nulls are indicated by the black arrows.

6.4 Simulation results

In order investigate the underlying physics of the asymmetric interaction, simplified 3D simulations were performed using the fully relativistic particle-in-cell code OSIRIS 4.0 [123, 124]. Rather than simulate the full laser-plasma interaction, the two plasmas were initialized on a slab target with representative temperatures and densities. The initial simulation geometry is depicted in Figure 6.5, where the high intensity interaction is represented by a population of hot electrons, and the moderate intensity interaction is the plasma obstacle.

Using units normalized by the plasma frequency, the simulation domain spanned $[x, y, z]$ = [-150:300, 0:200, -150:150] (c/ω_p), resolved by $1350 \times 400 \times 900$ cells. The time step was 0.211 ($1/\omega_p$). Due to computational expense, only electrons were simulated with 8 particles-per-cell and cubic interpolation, while ions were treated as immobile. Periodic boundary conditions were used in the z direction. Otherwise, open boundary conditions were used for the fields and particles, with the exception of a thermal boundary for target electrons at $y = 0$. The slab target is a uniform plasma in the $x - z$ plane extending from $y = 0$ to $y_s = 50$ (c/ω_p), with a density of $1n_c$. As shown in Chapter 5.4.1, the presence of a critical density surface is essential for sheath electric field and magnetic field generation by the hot electrons. An exponentially decaying profile with a scale length of $1/4\lambda_p$ extends from the slab surface in the $+y$ direction.

The moderate intensity laser-produced plasma is modeled based on concepts developed by Fox *et al.* [150] and Totorica *et al.* [42]. For the remainder of this discussion, this plasma will be referred to as the "plasma obstacle" or simply "obstacle. The initial density profile is described by

$$n_o(r_o, y) = n_0 \cos^2\left(\frac{\pi r_o}{2R_n}\right) \quad \text{if} \quad r_o < R_n \quad \text{and} \quad y > y_s \tag{6.1}$$

where $r_o = \sqrt{(x - x_o)^2 + z^2}$. The peak density is set to $n_0 = 1n_c$, and the radial extent is $R_n = 100$ (c/ω_p). An azimuthal magnetic field is embedded into the obstacle with a spatial

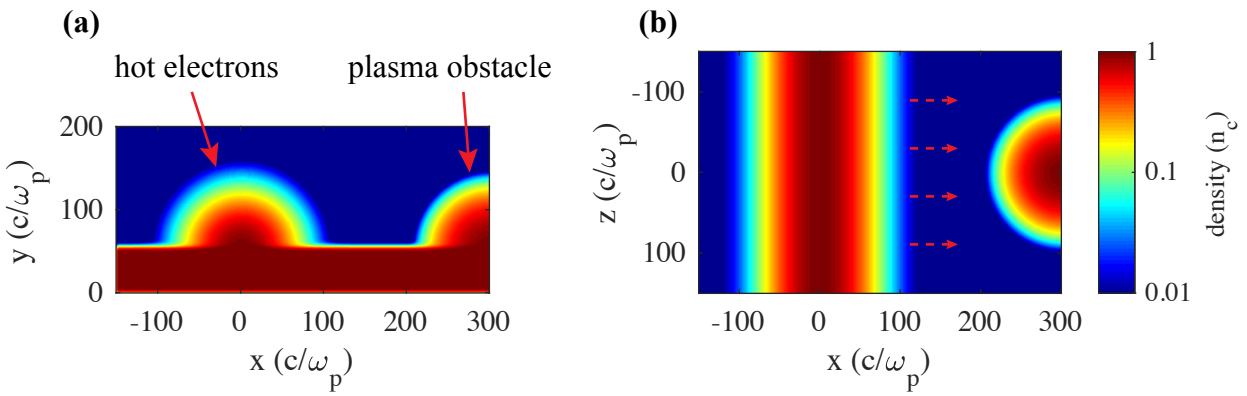

Figure 6.5: Slices through initial 3D density profile are shown at (a) z = 0 and (b) y = 60 (c/ω_p). As the system evolves, a sheet of hot electrons expands across the slab surface toward the plasma obstacle.

profile given by

$$B_o(r_o, y) = B_0 \sin\left(\frac{\pi r_o}{R_n}\right) \exp\left(\frac{-(y - y_B)^2}{L_B^2}\right) \hat{\theta} \quad \text{if} \quad r_o < R_n \quad \text{and} \quad y > y_s \tag{6.2}$$

where $y_B = y_s + \lambda_P$ defines the y position of the peak field and $L_B = R_n/4$ determines the field width. In normalized units, the peak field of the obstacle, B_0, is 0.05 $m_e\omega_p/e$. A uniform temperature for the obstacle (and slab target) of $k_B T_o = 0.01 m_e c^2$ results in a plasma β of $\sim$10. Due to the large asymmetry in thermal velocities between the obstacle and hot electrons from the high intensity interaction, the obstacle is assumed to be stationary.

Based on work described in Chapter 5.4.1, the high intensity laser-driven plasma was simulated by a hot electron population with a Gaussian density profile. The hot electron population has a peak density of $1n_c$ and was initialized with spatially-uniform relativistic Maxwell-Jüttner distribution with $k_B T_h = 2 m_e c^2$. The initial hot electron density profile is described by the following functional form

$$n_h(x, y) = n_0 \exp\left(\frac{-x^2}{L_h^2}\right) \exp\left(\frac{-(y - y_s)^2}{L_h^2}\right) \quad \text{if} \quad y > y_s \tag{6.3}$$

where y_s is the vertical position target surface, and L_h controls the width. In this simulation,

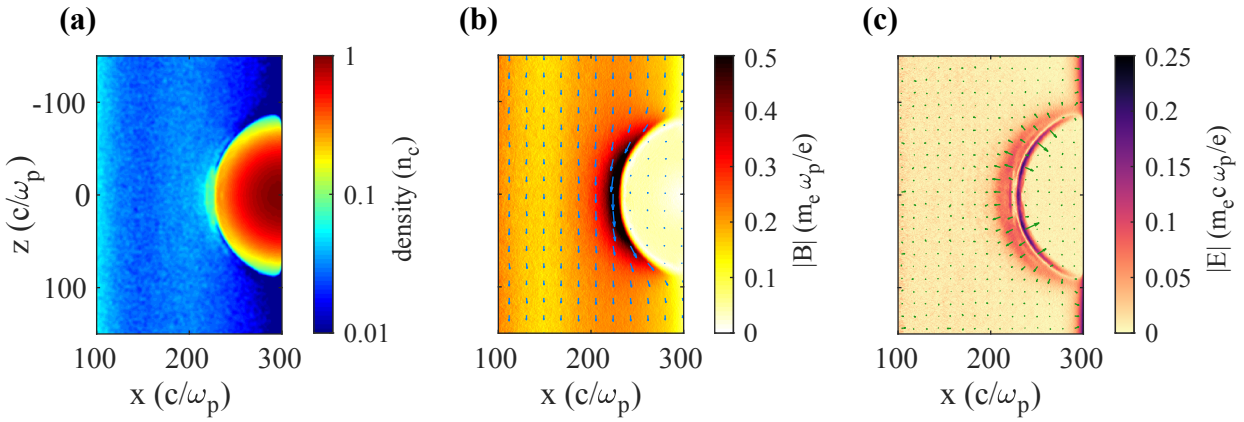

Figure 6.6: Slice through the simulation data at y = 60 (c/ω_p) and time 244 ($1/\omega_p$) after first contact. (a) In the electron density, compression of the obstacle is observed along with the formation of a boundary layer. (b) Self-generated magnetic field stagnates and piles up at the interface and (c) a bipolar, in-plane electric structure is produced. Note that electric fields form at the simulation boundary ($x = 300$ (c/ω_p)) as hot electrons exit the domain.

$L_h = 50$ (c/ω_p) in the x and y directions, while the profile is uniform in the z direction. Coupled with periodic boundary conditions in the z direction, the uniform profile results in the expansion of a quasi-infinite hot electron sheet toward the plasma obstacle. During the expansion, a strong transverse magnetic field is self-generated with an orientation opposite the field embedded in the obstacle.

Figure 6.6 shows a slice through the interaction at y = 60 (c/ω_p) approximately 244 ($1/\omega_p$) after the plasmas first come into contact. The x axis range has been narrowed to emphasize the interaction. A self-generated in-plane magnetic field is swept across the target with the hot electrons. As the two plasmas interact, this magnetic field stagnates and piles up at the interface (see Figure 6.6(b)) enhancing the asymmetry between the self-generated (B_h) and obstacle (B_o) fields, $B_h \sim 10B_o$. Compression of the obstacle is evident in Figure 6.6(a) and a disconnected boundary layer has developed. As shown in Figure 6.6(c), the compression and magnetic pile-up results in the formation of a strong in-plane, bipolar electric field structure along interface between the two plasmas.

Line-outs through the data at $z = 0$ are plotted together in Figure 6.7 and show the spatial relationship between magnetic flux pile-up, obstacle compression and electric field

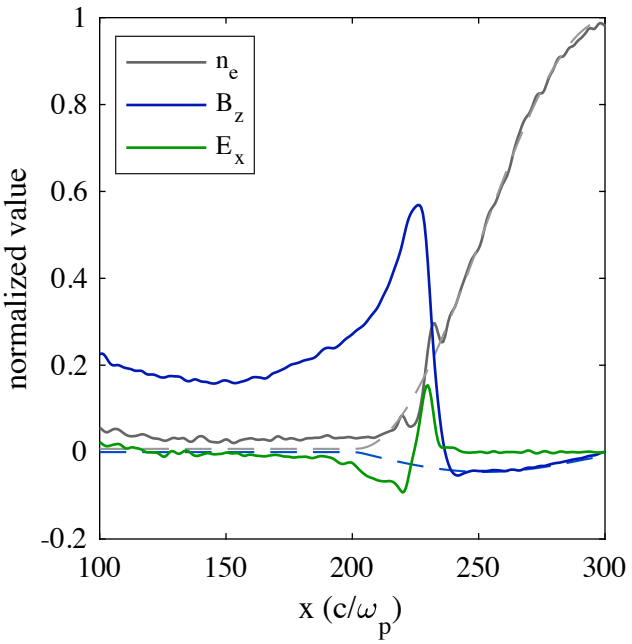

Figure 6.7: Line-outs taken through the data presented in Figure 6.6 at $z = 0$ (c/ω_p), $y = 60$ (c/ω_p), and time 244 ($1/\omega_p$) after the plasmas first come into contact. The initial density and magnetic field profiles are shown as dashed gray and blue lines, respectively.

generation. The initial density and embedded magnetic field profiles are plotted as dashed lines. From the line-outs, it is evident that the hot electron density driving in the field generation is relatively low, with $n_h < 0.1 n_c$ to the left of the interaction. The magnetic field pile-up is spatially correlated with the obstacle compression and bipolar electric field generation. In addition, the embedded magnetic field has been modified, either due to field annihilation or reconfiguration, potentially indicative of collisionless reconnection or shock-formation.

6.5 Discussion

Insight into the physical mechanisms governing magnetic field stagnation and electric field generation can be gained by considering pressure balance at the interface,

$$\langle\gamma_h\rangle n_h m_e c^2 + \frac{B_h^2}{2\mu_0} = n_o k_B T_o + \frac{B_o^2}{2\mu_0} + \frac{1}{2}\epsilon_0 E_{gen}^2 \tag{6.4}$$

where γ_h is the average Lorentz factor of the hot electrons, n_h is the hot electron density, and B_h is the magnetic field driven by the hot electrons. On the right-hand side, n_o, T_o and B_o are the density, temperature, and magnetic field of the obstacle (or long pulse plasma), and E_{gen} is the electric field generated during the interaction. Due to the strong asymmetries in temperature and magnetic field, the thermal and magnetic pressure of the hot electrons will largely be balanced by electric field generation. Simple estimates based on $\langle\gamma_h\rangle \approx 3$ and $B_h \approx 10 - 100$ MG predict a peak electric field strength of $\approx 10^{12}$ V/m. As observed in the simulation, the electron field will be generated in a narrow region with a width on the order of the electron inertial length, (c/ω_p).

While electric fields were generated in the simulation, no clear evidence was observed in the experiment. Instead, proton imaging primarily captured modifications to the Biermann battery magnetic field structure of the long pulse plasma. This is likely because the small spatial scale expected for the electric field falls below even the optimal resolution of TNSA beams ($\sim 10 - 20\mu$m). For example, Figure 6.8 demonstrates the effect of a finite source size by convolving a bipolar field structure with progressively larger Gaussian sources, where l_s defines the $1/e$ width. As the source function approaches realistic widths, the bipolar field disappears.

Beyond the intrinsic resolution limits of TNSA protons, blurring due to scattering in the target will broaden and reduce the intensity of features in the image, affecting the accuracy of the quantitative field analysis and further degrading the ability to resolve micro-physics of the interaction. In addition, protons accelerated from the main interaction foil

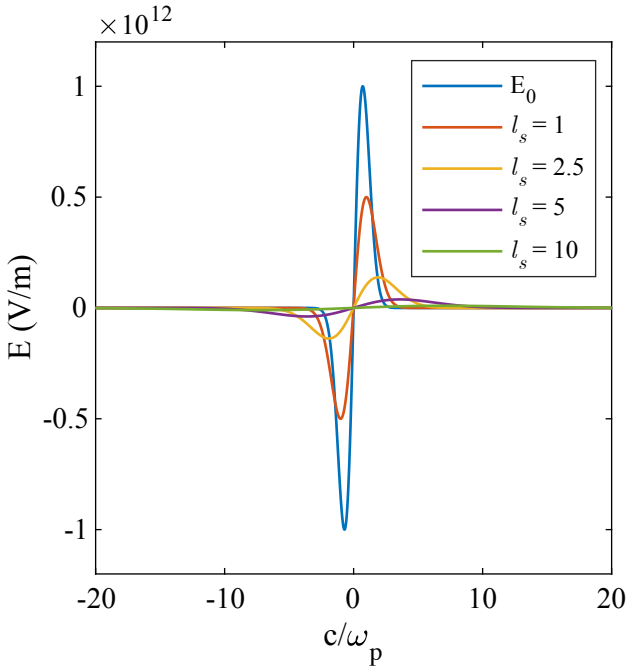

Figure 6.8: The finite source size of TNSA proton beams limits the resolution of small scale field structures. A bipolar field (E_0) with a 1 (c/ω_p) width is convolved with Gaussian sources ranging from 1 to 10 (c/ω_p) in size.

will also be detected in the RCF stack, contributing a non-uniform background signal to images. This increases the difficulty of quantitative image interpretation and undisturbed beam profile inference. The potential for background signal proton signal is unavoidable in this experimental geometry, however the intensity of main interaction laser pulse is lower than the pulse driving the proton imaging source. As a result, the self-emitted protons are typically less energetic than the probe. Higher energy layers of the RCF stack should exhibit less background signal, as well as reduced scattering, providing more accurate measurements of the fields.

The simplified simulation model presented shows some qualitative agreement with the experimental results. Magnetic field pile-up and compression observed in the simulation can potentially explain the cone-shaped feature found experimentally. Attempts to make direct comparisons to the experiment, such as producing synthetic proton images, are challenging due to the small scale and idealized nature of the simulation. In particular, a number of

important details of the laser-plasma interactions are not captured. Experimentally the asymmetric interaction occurs while the moderate intensity pulse is still driving Biermann battery field generation. This potentially influences field annihilation or reconnection in a manner not present in the simulation. While the plasma β of the obstacle is of similar order to long pulse produced plasmas, the temperature and field strength in used in simulation are higher than experimental measurements.

As shown in Chapter 5, the hot electron population accurately models field generation by high intensity laser pulses. However, the simulation does not capture the time-dependence of the full 10 ps drive used experimentally. Additionally, neglecting ion motion on the short time scale of this simulation is likely justified, but ion dynamics could be important during the multi-picosecond interaction.

6.6 Conclusions

Time-resolved proton imaging captured the dynamics of a highly asymmetric magnetic interaction driven by moderate and high intensity laser pulses. Despite challenges introduced by scattering and non-uniform proton signal, inversion of the proton images yielded quantitative and qualitative measurements of the magnetic fields. Quasi-static Biermann battery field structures were modulated by the impulsive interaction with relativistic electrons and the accompanying magnetic fields.

A simplified 3D PIC simulation of the experiment illuminated key aspects of the microphysics of the asymmetric interaction, including magnetic field pile-up, compression and electric field generation. The extreme thermal and magnetic pressures driven by the hot electrons are likely balanced by the generation of strong electric fields. Improvements to the simulation could be made by using a larger domain to include the full obstacle and limit impact of the boundaries.

This experimental platform developed in this chapter produces opposing magnetic fields

and strong asymmetries, with $B_h/B_o \sim 10 - 100$, $T_h/T_o \sim 1000$, $n_h/n_o \sim 0.1$, and $v_h/v_o \sim 100$. Features observed in the both experiment and simulation point to a dynamic magnetic interaction with evidence of shock formation and magnetic field annihilation. With further experimental and computational developments, this work could potentially be extended to study fundamental physics of collisionless magnetized plasma interactions, including asymmetric reconnection and magnetized bow-shock formation.

CHAPTER 7

Conclusions and Future Work

In this thesis, experiments and simulations explored the effect of pulse duration on laser-driven proton beam quality. Optimal laser conditions were identified and the laser-driven proton source was used to diagnose the generation and evolution of self-generated fields in high power laser-solid interactions. Target material was observed to affect the magnetic field topology and transport in both moderate and high intensity interactions. Finally, high and moderate intensity pulses were combined into a laser-driven reconnection geometry. Features observed in the proton images and 3D simulations suggest a dynamic magnetic interaction, possibly evidence shock-formation or asymmetric reconnection. The conclusions from each experimental chapter and potential future directions will be summarized below.

Proton beam emittance growth in multipicosecond laser-solid interactions

Experiments were conducted at the OMEGA EP laser facility to study the effect of laser pulse duration and energy laser-driven proton acceleration. Using stacks of radiochromic film, simultaneous spectral and spatial measurement were made of accelerated beams. In addition to first observations of TNSA acceleration driven by a relativistically intense, 100 ps laser pulses (much longer than typical TNSA experiments), the proton beam quality was found to degrade as the pulse duration was increased. 2D particle in cell simulations revealed

significant expansion of the target during longer pulses, resulting in enhanced filamentary field structures which deflect protons from uniform trajectories and increase the emittance.

For high energy, high power laser systems, these results demonstrate that the laser pulse duration should be minimized to limit pre-expansion of plasma from the rear target surface before the peak electron current arrives in order to ensure optimal proton beam quality. While multipicosecond interactions may enable superponderomotive electron heating and favorable ion energy scaling the non-uniformity of the accelerated proton beams make them unsuitable for proton radiography. These results can help guide future experimental designs both on OMEGA EP and other HED facilities, such as the NIF-ARC which can also produce kilojoule, multipicosecond laser pulses. Optimal laser pulse conditions identified here were used for proton radiography experiments in the subsequent chapters.

Potential extensions of this work could take advantage of the flexibility of the OMEGA EP system to design scans of laser energy or pulse duration while keeping other parameters fixed. For example, a relatively simple experiment would scan the laser energy with the pulse duration such that the focused intensity remained constant between shots. This would more fully distinguish intensity and pulse duration effects in the multipicosecond interaction regime.

Target material effects on magnetic field generation driven by high power lasers

A second set of OMEGA EP experiments examined magnetic field generation in laser-solid interactions with both moderate intensity long pulses and high intensity short pulses. Proton radiography was used to measure the strength and evolution of self-generated magnetic fields as the target material was varied between plastic, aluminum and copper.

These experiments and accompanying simulations demonstrate that target material can have a profound effect on the topology of magnetic fields generated in both intensity regimes.

At moderate intensities ($I_L \approx 10^{14}$ Wcm^{-2}), radiation transport in mid-Z targets drives double ablation front structures, initiating multiple regions of Biermann battery field generation. Because these results serve as a good benchmark for extended radiation-MHD simulation tools, future experiments could expand this on data to make additional comparisons. In particular, high resolution measurements of the magnetic field evolution in mid to high-Z plasma is made possible by using layered targets to limit proton scattering. Higher resolution measurements of the double ablation front temporal evolution in copper targets would complement the data presented in this work. Exploration of ICF relevant high Z materials, such as gold, could validate predictions of magnetic field generation in hohlraums.

With high intensity pulses ($I_L \approx 10^{19}$ Wcm^{-2}), filamentation of relativistic electron currents is enhanced in insulating, low-Z targets. Due to multipicosecond drive used in these experiments, the filamentation mechanism is likely a dynamic combination of resistive and Weibel-like instabilities. Simplified 2D simulations captured key aspects of the field generation mechanism. A theoretical prediction and scaling argument for the peak magnetic field strength was validated by a simple, cylindrically symmetric model which illustrated the link between the hot electron population, strong sheath field formation and magnetic field generation.

In 2D simulations of the high intensity laser-solid interaction, enhanced coupling of laser energy into hot electrons is observed as the preformed plasma scale length is increased. At scale lengths beyond $1\lambda_0$, laser channeling begins to dominate and strong channel fields form. In addition, preformed plasma expansion enhances filamentary field formation that likely contributes to the spoke-like features observed in the proton images.

One of the key challenges of these measurements is proton trajectory crossing due to the strong fields. This limits the ability to make direct quantitative analysis of the field structures. Future experiments could potentially overcome this by instead probing with ultra-relativistic electron beams [9]. Laser-wakefield accelerators can produce low-emittance GeV electron beams which could experience smaller deflections within the magnetic fields. In

addition, the electron beams have ultrashort durations resulting in extremely high temporal resolution (∼few femtoseconds).

While full 3D simulations of the laser-solid interaction are prohibitively expensive, new quasi-3D algorithms have been developed based on a Fourier decomposition of the azimuthal ($\hat{\theta}$) direction [125]. This significantly reduces the computational load, and could enable studies of key 3D effects on the magnetic field generation.

Proton radiography of a highly asymmetric laser-driven magnetic interaction

Magnetic fields driven by a high intensity, short pulse and a moderate intensity, long pulse were brought together form a magnetic interaction with strong asymmetries, with $B_h/B_o \sim 10 - 100$, $T_h/T_o \sim 1000$, $n_h/n_o \sim 0.1$, and $v_h/v_o \sim 100$. Time-resolved proton radiography captured the dynamics as the impulsive fields produced by the high intensity laser was driven into the slowly evolving long pulse plasma and associated Biermann battery fields. Inversion of the proton images yielded quantitative and qualitative measurements of modulations to the Biermann battery fields during the interaction.

A simplified 3D PIC simulation of the experiment was developed which illuminated key aspects of the asymmetric interaction, including magnetic field pile-up, plasma compression and electric field generation. The extreme thermal and magnetic pressures driven by the hot electrons are likely balanced by the generation of strong electric fields. Features observed in the both experiment and simulation point to a dynamic magnetic interaction with evidence of shock formation and magnetic field annihilation.

Further experimental and computational developments could extended this work to study fundamental physics of collisionless magnetized plasma interactions, including asymmetric reconnection and magnetized bow-shock formation. In particular, future experiments could couple proton radiography measurements with transverse optical probing to look for evidence of compression and shock formation in the plasma density profile. Simulations with a larger

domain would enable more accurate comparisons with the experiments, including synthetic radiography. In particular, future simulation work should endeavor to include the full plasma obstacle in order to observe how the flow of relativistic electrons and magnetic field is altered downstream of the interaction region. While likely prohibitively computationally expensive, a full 3D simulation including the high intensity laser-plasma interaction and more realistic density and magnetic field profiles for the long pulse plasma (taken from MHD simulations) would enable more straightforward comparison with the experiment.

APPENDIX A

Plasma Expansion Model

Following the approach presented by Mora [78], the sheath electric field, ion energy spectrum and maximum ion energy can be estimated. The electron density is given by

$$n_e(x) = n_{e0} \exp\big(e\phi(x)/k_B T_e\big) \tag{A.1}$$

where ϕ is the electrostatic potential and $k_B T_e$ is the hot electron temperature. Ions are initially at rest, and the sharp target interface is at $x = 0$ with $n_i = 0$ for $x > 0$. The Poisson equation can be used to relate the potential th the electron density

$$\frac{\partial^2 \phi(x)}{\partial x^2} = -\rho/\epsilon_0 = e(n_e - Z n_i)/\epsilon_0 \tag{A.2}$$

where ϵ_0 is the vacuum permittivity and Z is the ion charge. Integration leads to an estimate for the electric field. Assuming charge neutrality for $x < 0$ ($n_e = Z n_i$) and recalling $n_i = 0$ for $x > 0$, the Poisson equation can be broken into two parts,

$$\begin{aligned} \frac{\partial^2 \phi(x)}{\partial x^2} &= \frac{e}{\epsilon_0} n_{e0} \Big[\exp\big(e\phi(x)/k_B T_e\big) - 1 \Big] \quad \text{for} \quad x < 0 \\ &= \frac{e}{\epsilon_0} n_{e0} \exp\big(e\phi(x)/k_B T_e\big) \quad \text{for} \quad x > 0. \end{aligned} \tag{A.3}$$

The electric field is given by $E = -\partial\phi(x)/\partial x$. Integration of equation (A.3) assuming $E = 0$ and $\phi = 0$ at $x = -\infty$, and $E = 0$ and $\phi = -\infty$ at $x = \infty$ yields

$$\begin{aligned} \frac{1}{2}E^2 &= \frac{n_{e0}k_BT_e}{\epsilon_0}\left[\exp\left(e\phi(x)/k_BT_e\right) - 1 - e\phi/k_BT_e\right] \quad \text{for} \quad x < 0 \\ &= \frac{n_{e0}k_BT_e}{\epsilon_0}\exp\left(e\phi(x)/k_BT_e\right) \quad \text{for} \quad x > 0. \end{aligned} \tag{A.4}$$

(Note: integration accomplished by first multiplying both sides of the equation by $\partial\phi(x)/\partial x$.) The electric field is continuous at $x = 0$, so the initial electrostatic potential at the interface must be

$$\phi(x = 0) = -k_BT_e/e. \tag{A.5}$$

Plugging this into the expression for the electric field, the initial electric field is given

$$E = \sqrt{\frac{2}{e_N}}\sqrt{\frac{n_{e0}k_BT_e}{\epsilon_0}} = \sqrt{\frac{2}{e_N}}\frac{k_BT_e}{e\lambda_{D0}} = \sqrt{\frac{2}{e_N}}E_0. \tag{A.6}$$

where e_N is the numerical constant (i.e., $\exp(1)$), and λ_{D0} is the Debye length for $n_e = n_{e0}$,

$$\lambda_{D0} = \sqrt{\frac{\epsilon_0 k_BT_e}{n_{e0}e^2}}$$

As the plasma expands, the electric field will be modified. The electric field at the expansion front (x_f) can be found by integrating the second part of equation (A.3) from x_f to ∞,

$$E = \sqrt{\frac{n_{e0}k_BT_e}{\epsilon_0}}\sqrt{2\exp\left(e\phi(x_f)/k_BT_e\right)} = \sqrt{\frac{n_{e0}k_BT_e}{\epsilon_0}}\sqrt{\frac{2n_e(x_f)}{n_{e0}}} = \sqrt{2}\,\frac{k_BT_e}{e\lambda_D^*}, \tag{A.7}$$

where λ_D^* is the local Debye length ($\lambda_D^* = \lambda_{D0}(n_{e0}/n_e)^{1/2}$). Based a 1D simulation, the time

dependence of the electric field at the front is found to be well modeled by

$$E_f(t) \approx \frac{2E_0}{(2e_N + \omega_{pi}^2 t^2)^{1/2}}, \tag{A.8}$$

where $\omega_{pi} = (n_{e0}Ze^2/m_i\epsilon_0)^{1/2}$ is the ion plasma frequency. The velocity of the expansion can be obtained by integrating $\mathrm{d}v/\mathrm{d}t = ZeE(t)/m_i$, which yields

$$v_f \approx 2c_s \ln(\tau + \sqrt{\tau^2 + 1}), \tag{A.9}$$

where $c_s = (Zk_BT_e/m_i)^{1/2}$ is the ion-acoustic sound speed and $\tau = \omega_{pi}t/\sqrt{2e_N}$.

The Mora model predicts an energy spectrum for ions per unit surface given by

$$\mathrm{d}N/\mathrm{d}\mathcal{E}_i = \frac{n_{i0}c_s t}{\sqrt{2\mathcal{E}_i\mathcal{E}_0}} \exp\big(-\sqrt{2\mathcal{E}_i/\mathcal{E}_0}\big) \tag{A.10}$$

where $\mathcal{E}_i$ is the ion kinetic energy and $\mathcal{E}_0 = Zk_BT_e$. The spectrum exhibits a well defined cutoff energy at

$$\mathcal{E}_{max} = 1/2 m_i v_f^2 = 2\mathcal{E}_0[\ln(\tau + \sqrt{\tau^2 + 1})]^2. \tag{A.11}$$

APPENDIX B

Proton Image Inversion Algorithms

The following sections of pseudo-code describe the basic implementation of proton image inversion techniques described in section 3.4.

Algorithm 1: Jacobian inversion method

input : I, $\tilde{I}_0$
output: deflection potential, $\tilde{\Phi}$, and $(\tilde{x}, \tilde{y})$

initialize normalized spatial coordinates $(\tilde{x}, \tilde{y})$
% Solve for $\tilde{\Phi}_1$*:*
$\tilde{\nabla}^2\tilde{\Phi}_1 = \frac{\tilde{I}_0+\epsilon}{I+\epsilon} - 1$

% Begin iterative solution including nonlinear terms
while *difference(*I_{interp}*,*I_i*) or difference(*$\tilde{\Phi}_i$*,*$\tilde{\Phi}_{i-1}$*) > tolerance* **do**
    Use $\tilde{\Phi}_i$ and $\tilde{I}_0$ to calculate (x_i, y_i) and I_i
    calculate I_{interp} by interpolating I onto (x_i, y_i)
    $I^* = \text{average}(I_{interp}, I_i)$
    % use full expression (equation (3.19)) to solve for $\tilde{\Phi}_{i+1}$
    $\tilde{\nabla}^2\tilde{\Phi}_{i+1} = \frac{\tilde{I}_0+\epsilon}{I^*+\epsilon} - 1 - \frac{\partial^2\tilde{\Phi}_i}{\partial\tilde{x}^2}\frac{\partial^2\tilde{\Phi}_i}{\partial\tilde{y}^2} + \left(\frac{\partial^2\tilde{\Phi}_i}{\partial\tilde{x}\partial\tilde{y}}\right)^2$
end

Algorithm 2: Polar Runge-Kutta integration method

input : r_0, J, J_0, ν_B
output: $\mathcal{B}_\theta$

$J^* = J/J_0$
$\mathcal{B}_\theta(1) = 0$
$\tilde{r}_1 = r_0(1)$
% calculate $\Delta\mathcal{B}_{\theta 1}$,
$\Delta\mathcal{B}_{\theta 1} = \frac{1}{\nu_B}\left[\frac{1}{J^*(1)} - 1\right]$

% Begin iterative solution
for $i = 2$ *: length(*J^**)* **do**
    $k_1 = \Delta\mathcal{B}_{\theta i-1}$
    $b_1 = \mathcal{B}_\theta(i-1) + k_1\Delta r_0/2$
    $r_1 = r_0 + \Delta r_0/2$
    $\tilde{r}_1 = r_1 + \nu_B b_1$
    $\mathcal{J}_1 =$ interpolate J^* on to $\tilde{r}_1$

    $k_2 = \frac{1}{\nu_B}\left[\frac{r_1}{\tilde{r}_1\mathcal{J}_1} - 1\right]$
    $b_2 = \mathcal{B}_\theta(i-1) + k_1\Delta r_0/2$
    $r_2 = r_0 + \Delta r_0/2$
    $\tilde{r}_2 = r_2 + \nu_B b_2$
    $\mathcal{J}_2 =$ interpolate J^* on to $\tilde{r}_2$

    $k_3 = \frac{1}{\nu_B}\left[\frac{r_2}{\tilde{r}_2\mathcal{J}_2} - 1\right]$
    $b_3 = \mathcal{B}_\theta(i-1) + k_1\Delta r_0$
    $r_3 = r_0 + \Delta r_0$
    $\tilde{r}_3 = r_3 + \nu_B b_3$
    $\mathcal{J}_3 =$ interpolate J^* on to $\tilde{r}_3$

    $k_4 = \frac{1}{\nu_B}\left[\frac{r_3}{\tilde{r}_3\mathcal{J}_3} - 1\right]$

    $\Delta\mathcal{B}_{\theta i} = (k_1 + 2k_2 + 2k_3 + k + 4)/6$
    $\mathcal{B}_\theta(i) = \mathcal{B}_\theta(i-1) + \Delta\mathcal{B}_{\theta i}\Delta r_0$
end

APPENDIX C

Radiochromic film stack designs

Table C.1: **60 MeV** stack design and corresponding proton energies used in Chapter 4

Layer	Material	E_p (± 0.1 MeV)
1	100 μm Al	—
2	HD-V2	3.5
3	100 μm Al	—
4	HD-V2	6.2
5	100 μm Al	—
6	HD-V2	8.2
7	100 μm Al	—
8	HD-V2	9.9
9	500 μm Al	—
10	HD-V2	14.4
11	500 μm Al	—
12	HD-V2	18.0
13	1000 μm Al	—
14	HD-V2	23.5
15	1000 μm Al	—
16	HD-V2	28.2
17	2000 μm Al	—
18	HD-V2	35.8
19	2000 μm Al	—
20	HD-V2	42.3
21	3000 μm Al	—
22	MD-V3	51.0
23	4000 μm Al	—
24	MD-V3	60.9

Table C.2: **Spec-60 MeV** stack design used for 100 ps shots in Chapter 4

Layer	Material	E_p (± 0.1 MeV)	Layer	Material	E_p (± 0.1 MeV)
1	100 μm Al	—	24	MD-V3	25.0
2	HD-V2	3.5	25	1000 μm Al	—
3	100 μm Al	—	26	MD-V3	29.8
4	HD-V2	6.2	27	1000 μm Al	—
5	100 μm Al	—	28	MD-V3	34.1
6	HD-V2	8.2	29	2000 μm Al	—
7	100 μm Al	—	30	MD-V3	41.1
8	HD-V2	9.9	31	2000 μm Al	—
9	100 μm Al	—	32	MD-V3	47.3
10	HD-V2	11.4	33	3000 μm Al	—
11	100 μm Al	—	34	MD-V3	55.4
12	HD-V2	12.7	35	3000 μm Al	—
13	200 μm Al	—	36	MD-V3	62.6
14	HD-V2	14.6			
15	200 μm Al	—			
16	HD-V2	16.4			
17	200 μm Al	—			
18	HD-V2	18.0			
19	300 μm Al	—			
20	HD-V2	20.0			
21	300 μm Al	—			
22	HD-V2	21.9			
23	500 μm Al	—			

Table C.3: **HR60 MeV** stack design used in Chapters 5 and 6

Layer	Material	E_p (± 0.1 MeV)	Layer	Material	E_p (± 0.1 MeV)
1	500 μm Al	—	24	HD-V2	33.4
2	HD-V2	8.9	25	2000 μm Al	—
3	100 μm Al	—	26	HD-V2	40.2
4	HD-V2	10.5	27	2000 μm Al	—
5	100 μm Al	—	28	HD-V2	46.2
6	HD-V2	11.9	29	3000 μm Al	—
7	100 μm Al	—	30	MD-V3	54.4
8	HD-V2	13.2	31	3000 μm Al	—
9	200 μm Al	—	32	MD-V3	61.7
10	HD-V2	15.1			
11	200 μm Al	—			
12	HD-V2	16.8			
13	200 μm Al	—			
14	HD-V2	18.4			
15	300 μm Al	—			
16	HD-V2	20.4			
17	300 μm Al	—			
18	HD-V2	22.2			
19	500 μm Al	—			
20	HD-V2	24.9			
21	1000 μm Al	—			
22	HD-V2	29.4			
23	1000 μm Al	—			

Table C.4: **VHTR** stack design used for very high temporal resolution in Chapters 5 and 6

Layer	Material	E_p (± 0.1 MeV)	Layer	Material	E_p (± 0.1 MeV)
1	500 μm Al	—	24	HD-V2	24.8
2	HD-V2	8.9	25	200 μm Al	—
3	300 μm Al	—	26	HD-V2	26.0
4	HD-V2	12.1	27	200 μm Al	—
5	500 μm Al	—	28	HD-V2	27.1
6	HD-V2	16.1	29	300 μm Al	—
7	HD-V2	16.6	30	HD-V2	28.6
8	HD-V2	17.0	31	400 μm Al	—
9	HD-V2	17.4	32	HD-V2	30.4
10	HD-V2	17.8	33	500 μm Al	—
11	100 μm Al	—	34	HD-V2	32.5
12	HD-V2	18.8	35	500 μm Al	—
13	100 μm Al	—	36	HD-V2	34.5
14	HD-V2	19.7	37	700 μm Al	—
15	100 μm Al	—	38	HD-V2	37.1
16	HD-V2	20.6	39	800 μm Al	—
17	100 μm Al	—	40	HD-V2	39.9
18	HD-V2	21.5	41	900 μm Al	—
19	100 μm Al	—	42	HD-V2	42.8
20	HD-V2	22.3	43	3000 μm Al	—
21	200 μm Al	—	44	MD-V3	51.4
22	HD-V2	23.6	45	3000 μm Al	—
23	200 μm Al	—	46	MD-V3	59.0

APPENDIX D

SRIM proton scattering estimates

SRIM [113,114] was used to estimate the scattering angle for protons passing through targets of various materials and thickness. This analysis was conducted by Charlotte Palmer and shared through personal communication. To generate the scattering angle information, a number of particles are tracked through a thick target in SRIM and the EXYZ output is recorded. Then, a MATLAB script is used to calculate changes to the trajectory accumulated as particles propagate the thickness of interest. Figure D.1 shows the results for 30 MeV protons passing through 25 μm of copper, 50 μm of aluminum, and 50 μm of CH. Note that the axes have changed for the CH case due to the relatively small amount of scattering. When estimating the impact of such scattering on proton imaging (as in Chpater 6), the peak of the probability density function (PDF) is used.

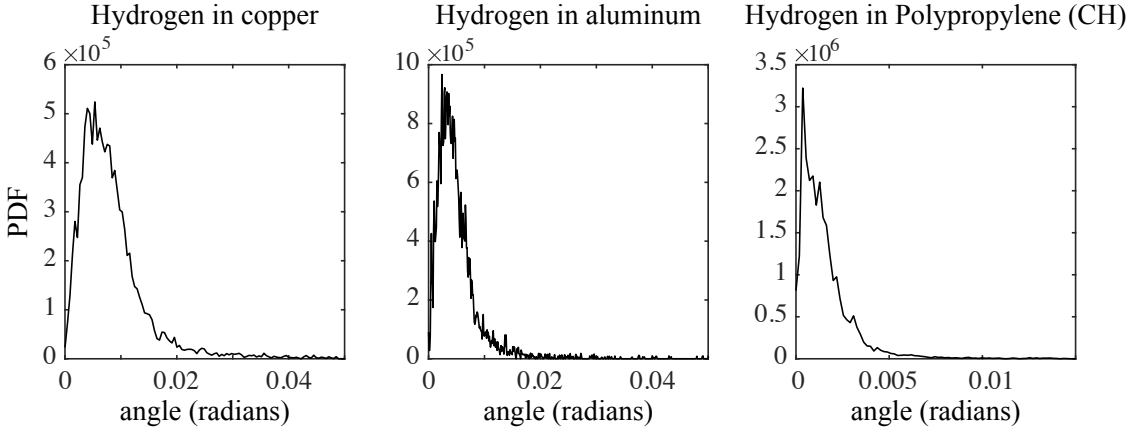

Figure D.1: Estimates of scattering of 30 MeV protons in 25 μm Cu, 50 μm Al, or 50 μm CH targets made with SRIM

BIBLIOGRAPHY

[1] J. L. Burch, T. E. Moore, R. B. Torbert, and B. L. Giles, *Magnetospheric Multiscale Overview and Science Objectives*, Space Science Reviews **199**, 5–21 (2016).

[2] http://creativecommons.org/licenses/by/4.0/.

[3] H. Ji and W. Daughton, *Phase diagram for magnetic reconnection in heliophysical, astrophysical, and laboratory plasmas*, Physics of Plasmas **18**, 111207 (2011).

[4] J. Schreiber, F. Bell, F. Grüner, U. Schramm, M. Geissler, M. Schnürer, S. Ter-Avetisyan, B. M. Hegelich, J. Cobble, E. Brambrink, J. Fuchs, P. Audebert, and D. Habs, *Analytical Model for Ion Acceleration by High-Intensity Laser Pulses*, Physical Review Letters **97**, 045005 (2006).

[5] R. P. Drake, *High Energy Density Physics: Fundamentals, Inertial Fusion and Experimental Astrophysics*, Springer International Publishing, Berlin, 2nd edition (2018).

[6] B. A. Remington, R. P. Drake, and D. D. Ryutov, *Experimental astrophysics with high power lasers and Z pinches*, Reviews of Modern Physics **78**, 755–807 (2006).

[7] J. A. Stamper, K. Papadopoulos, R. N. Sudan, S. O. Dean, E. A. McLean, and J. M. Dawson, *Spontaneous Magnetic Fields in Laser-Produced Plasmas*, Physical Review Letters **26**, 1012–1015 (1971).

[8] L. Gao, P. M. Nilson, I. V. Igumenshchev, M. G. Haines, D. H. Froula, R. Betti, and D. D. Meyerhofer, *Precision Mapping of Laser-Driven Magnetic Fields and Their Evolution in High-Energy-Density Plasmas*, Physical Review Letters **114**, 215003 (2015).

[9] W. Schumaker, N. Nakanii, C. McGuffey, C. Zulick, V. Chyvkov, F. Dollar, H. Habara, G. Kalintchenko, A. Maksimchuk, K. A. Tanaka, A. G. R. Thomas, V. Yanovsky, and K. Krushelnick, *Ultrafast Electron Radiography of Magnetic Fields in High-Intensity Laser-Solid Interactions*, Physical Review Letters **110**, 015003 (2013).

[10] G. Sarri, A. Macchi, C. A. Cecchetti, S. Kar, T. V. Liseykina, X. H. Yang, M. E. Dieckmann, J. Fuchs, M. Galimberti, L. A. Gizzi, R. Jung, I. Kourakis, J. Osterholz, F. Pegoraro, A. P. L. Robinson, L. Romagnani, O. Willi, and M. Borghesi, *Dynamics of Self-Generated, Large Amplitude Magnetic Fields Following High-Intensity Laser Matter Interaction*, Physical Review Letters **109**, 205002 (2012).

[11] S. E. Bodner, *Time-dependent asymmetries in laser-fusion hohlraums*, Comments on Plasma Physics and Controlled Fusion **16**, 351–374 (1995).

[12] T. H. Kho and M. G. Haines, *Nonlinear Kinetic Transport of Electrons and Magnetic Field in Laser-Produced Plasmas*, Physical Review Letters **55**, 825–828 (1985).

[13] S. H. Glenzer, W. E. Alley, K. G. Estabrook, J. S. De Groot, M. G. Haines, J. H. Hammer, J.-P. Jadaud, B. J. MacGowan, J. D. Moody, W. Rozmus, L. J. Suter, T. L. Weiland, and E. A. Williams, *Thomson scattering from laser plasmas*, Physics of Plasmas **6**, 2117–2128 (1999).

[14] D. H. Froula, J. S. Ross, B. B. Pollock, P. Davis, A. N. James, L. Divol, M. J. Edwards, A. A. Offenberger, D. Price, R. P. J. Town, G. R. Tynan, and S. H. Glenzer, *Quenching of the Nonlocal Electron Heat Transport by Large External Magnetic Fields in a Laser-Produced Plasma Measured with Imaging Thomson Scattering*, Physical Review Letters **98**, 135001 (2007).

[15] C. P. Ridgers, R. J. Kingham, and A. G. R. Thomas, *Magnetic Cavitation and the Reemergence of Nonlocal Transport in Laser Plasmas*, Physical Review Letters **100**, 075003 (2008).

[16] L. Willingale, A. G. R. Thomas, P. M. Nilson, M. C. Kaluza, S. Bandyopadhyay, A. E. Dangor, R. G. Evans, P. Fernandes, M. G. Haines, C. Kamperidis, R. J. Kingham, S. Minardi, M. Notley, C. P. Ridgers, W. Rozmus, M. Sherlock, M. Tatarakis, M. S. Wei, Z. Najmudin, and K. Krushelnick, *Fast Advection of Magnetic Fields by Hot Electrons*, Physical Review Letters **105**, 095001 (2010).

[17] J. Nuckolls, L. Wood, A. Thiessen, and G. Zimmerman, *Laser compression of matter to super-high densities: Thermonuclear (CTR) applications*, Nature **239**, 139 (1972).

[18] R. S. Craxton, K. S. Anderson, T. R. Boehly, V. N. Goncharov, D. R. Harding, J. P. Knauer, R. L. McCrory, P. W. McKenty, D. D. Meyerhofer, J. F. Myatt, A. J. Schmitt, J. D. Sethian, R. W. Short, S. Skupsky, W. Theobald, W. L. Kruer, K. Tanaka, R. Betti, T. J. B. Collins, J. A. Delettrez, S. X. Hu, J. A. Marozas, A. V. Maximov, D. T. Michel, P. B. Radha, S. P. Regan, T. C. Sangster, W. Seka, A. A. Solodov, J. M. Soures, C. Stoeckl, and J. D. Zuegel, *Direct-drive inertial confinement fusion: A review*, Physics of Plasmas **22**, 110501 (2015).

[19] J. Lindl, *Development of the indirectdrive approach to inertial confinement fusion and the target physics basis for ignition and gain*, Physics of Plasmas **2**, 3933–4024 (1995).

[20] P. Y. Chang, G. Fiksel, M. Hohenberger, J. P. Knauer, R. Betti, F. J. Marshall, D. D. Meyerhofer, F. H. Séguin, and R. D. Petrasso, *Fusion Yield Enhancement in Magnetized Laser-Driven Implosions*, Physical Review Letters **107**, 035006 (2011).

[21] A. S. Joglekar, C. P. Ridgers, R. J. Kingham, and A. G. R. Thomas, *Kinetic modeling of Nernst effect in magnetized hohlraums*, Physical Review E **93**, 043206 (2016).

[22] W. A. Farmer, J. M. Koning, D. J. Strozzi, D. E. Hinkel, L. F. Berzak Hopkins, O. S. Jones, and M. D. Rosen, *Simulation of self-generated magnetic fields in an inertial fusion hohlraum environment*, Physics of Plasmas **24**, 052703 (2017).

[23] R. G. Evans, *The influence of self-generated magnetic fields on the Rayleigh-Taylor instability*, Plasma Physics and Controlled Fusion **28**, 1021–1024 (1986).

[24] C. A. Walsh, J. P. Chittenden, K. McGlinchey, N. P. L. Niasse, and B. D. Appelbe, *Self-Generated Magnetic Fields in the Stagnation Phase of Indirect-Drive Implosions on the National Ignition Facility*, Physical Review Letters **118**, 155001 (2017).

[25] P. M. Nilson, L. Willingale, M. C. Kaluza, C. Kamperidis, S. Minardi, M. S. Wei, P. Fernandes, M. Notley, S. Bandyopadhyay, M. Sherlock, R. J. Kingham, M. Tatarakis, Z. Najmudin, W. Rozmus, R. G. Evans, M. G. Haines, A. E. Dangor, and K. Krushelnick, *Magnetic Reconnection and Plasma Dynamics in Two-Beam Laser-Solid Interactions*, Physical Review Letters **97**, 255001 (2006).

[26] E. G. Zweibel and M. Yamada, *Magnetic Reconnection in Astrphysical and Laboratory Plasmas*, Annual Review of Astronomy and Astrophysics **47**, 291–332 (2009).

[27] M. Yamada, R. Kulsrud, and H. Ji, *Magnetic reconnection*, Reviews of Modern Physics **82**, 603–664 (2010).

[28] C. Thompson, *A model of gamma-ray bursts*, Monthly Notices of the Royal Astronomical Society **270**, 480–498 (1994).

[29] Y. Lyubarsky and J. G. Kirk, *Reconnection in a striped pulsar wind*, The Astrophysical Journal **547**, 437–448 (2001).

[30] D. Giannios, D. A. Uzdensky, and M. C. Begelman, *Fast TeV variability in blazars: jets in a jet*, Monthly Notices of the Royal Astronomical Society: Letters **395**, L29–L33 (2009).

[31] D. Kagan, L. Sironi, B. Cerutti, and D. Giannios, *Relativistic magnetic reconnection in pair plasmas and its astrophysical applications*, Space Science Reviews **191**, 545–573 (2015).

[32] M. Yamada, H. Ji, S. Hsu, T. Carter, R. Kulsrud, N. Bretz, F. Jobes, Y. Ono, and F. Perkins, *Study of driven magnetic reconnection in a laboratory plasma*, Physics of Plasmas **4**, 1936–1944 (1997).

[33] W. Fox, A. Bhattacharjee, and K. Germaschewski, *Magnetic reconnection in high-energy-density laser-produced plasmas*, Physics of Plasmas **19**, 056309 (2012).

[34] C. K. Li, F. H. Séguin, J. A. Frenje, J. R. Rygg, R. D. Petrasso, R. P. J. Town, O. L. Landen, J. P. Knauer, and V. A. Smalyuk, *Observation of Megagauss-Field Topology Changes due to Magnetic Reconnection in Laser-Produced Plasmas*, Physical Review Letters **99**, 055001 (2007).

[35] P. M. Nilson, L. Willingale, M. C. Kaluza, C. Kamperidis, S. Minardi, M. S. Wei, P. Fernandes, M. Notley, S. Bandyopadhyay, M. Sherlock, R. J. Kingham, M. Tatarakis, Z. Najmudin, W. Rozmus, R. G. Evans, M. G. Haines, A. E. Dangor, and K. Krushelnick, *Bidirectional jet formation during driven magnetic reconnection in two-beam laser-plasma interactions*, Physics of Plasmas **15** (2008).

[36] L. Willingale, P. M. Nilson, M. C. Kaluza, A. E. Dangor, R. G. Evans, P. Fernandes, M. G. Haines, C. Kamperidis, R. J. Kingham, C. P. Ridgers, M. Sherlock, A. G. R. Thomas, M. S. Wei, Z. Najmudin, K. Krushelnick, S. Bandyopadhyay, M. Notley, S. Minardi, M. Tatarakis, and W. Rozmus, *Proton deflectometry of a magnetic reconnection geometry*, Physics of Plasmas **17**, 043104 (2010).

[37] J. Zhong, Y. Li, X. Wang, J. Wang, Q. Dong, C. Xiao, S. Wang, X. Liu, L. Zhang, L. An, F. Wang, J. Zhu, Y. Gu, X. He, G. Zhao, and J. Zhang, *Modelling loop-top x-ray source and reconnection outflows in solar flares with intense lasers*, Nature Physics **6**, 984–987 (2010).

[38] Q.-L. Dong, S.-J. Wang, Q.-M. Lu, C. Huang, D.-W. Yuan, X. Liu, X.-X. Lin, Y.-T. Li, H.-G. Wei, J.-Y. Zhong, J.-R. Shi, S.-E. Jiang, Y.-K. Ding, B.-B. Jiang, K. Du, X.-T. He, M. Y. Yu, C. S. Liu, S. Wang, Y.-J. Tang, J.-Q. Zhu, G. Zhao, Z.-M. Sheng, and J. Zhang, *Plasmoid Ejection and Secondary Current Sheet Generation from Magnetic Reconnection in Laser-Plasma Interaction*, Physical Review Letters **108**, 215001 (2012).

[39] M. J. Rosenberg, C. K. Li, W. Fox, A. B. Zylstra, C. Stoeckl, F. H. Séguin, J. A. Frenje, and R. D. Petraso, *Magnetic Reconnection between Colliding Magnetized Laser-Produced Plasma Plumes*, Physical Review Letters **114**, 205004 (2015).

[40] M. J. Rosenberg, C. K. Li, W. Fox, I. Igumenshchev, F. H. Séguin, R. P. J. Town, J. A. Frenje, C. Stoeckl, V. Glebov, and R. D. Petraso, *A Laboratory study of asymmetric magnetic reconnection in strongly driven plasmas*, Nature Communications **6**, 6190 (2015).

[41] A. S. Joglekar, A. G. R. Thomas, W. Fox, and A. Bhattacharjee, *Magnetic Reconnection in Plasma under Inertial Confinement Fusion Conditions Driven by Heat Flux Effects in Ohm's Law*, Physical Review Letters **112**, 105004 (2014).

[42] S. R. Totorica, T. Abel, and F. Fiuza, *Nonthermal Electron Energization from Magnetic Reconnection in Laser-Driven Plasmas*, Physical Review Letters **116**, 095003 (2016).

[43] A. Chien, L. Gao, H. Ji, X. Yuan, E. G. Blackman, H. Chen, P. C. Efthimion, G. Fiksel, D. H. Froula, K. W. Hill, K. Huang, Q. Lu, J. D. Moody, and P. M. Nilson, *Study of a magnetically driven reconnection platform using ultrafast proton radiography*, Physics of Plasmas **26**, 062113 (2019).

[44] A. E. Raymond, C. F. Dong, A. McKelvey, C. Zulick, N. Alexander, A. Bhattacharjee, P. T. Campbell, H. Chen, V. Chvykov, E. Del Rio, P. Fitzsimmons, W. Fox, B. Hou, A. Maksimchuk, C. Mileham, J. Nees, P. M. Nilson, C. Stoeckl, A. G. R. Thomas,

M. S. Wei, V. Yanovsky, K. Krushelnick, and L. Willingale, *Relativistic-electron-driven magnetic reconnection in the laboratory*, Physical Review E **98**, 043207 (2018).

[45] C. A. J. Palmer, P. T. Campbell, Y. Ma, L. Antonelli, A. F. A. Bott, G. Gregori, J. Halliday, Y. Katzir, P. Kordell, K. Krushelnick, S. V. Lebedev, E. Montgomery, M. Notley, D. C. Carroll, C. P. Ridgers, A. A. Schekochihin, M. J. V. Streeter, A. G. R. Thomas, E. R. Tubman, N. Woolsey, and L. Willingale, *Field reconstruction from proton radiography of intense laser driven magnetic reconnection*, Physics of Plasmas **26**, 083109 (2019).

[46] M. Borghesi, A. J. MacKinnon, A. R. Bell, R. Gaillard, and O. Willi, *Megagauss Magnetic Field Generation and Plasma Jet Formation on Solid Targets Irradiated by an Ultraintense Picosecond Laser Pulse*, Physical Review Letters **81**, 112–115 (1998).

[47] L. Lancia, B. Albertazzi, C. Boniface, A. Grisollet, R. Riquier, F. Chaland, K.-C. Le Thanh, P. Mellor, P. Antici, S. Buffechoux, S. N. Chen, D. Doria, M. Nakatsutsumi, C. Peth, M. Swantusch, M. Stardubtsev, L. Palumbo, M. Borghesi, O. Willi, H. Pépin, and J. Fuchs, *Topology of Megagauss Magnetic Fields and of Heat-Carrying Electrons Produced in a High-Power Laser-Solid Interaction*, Physical Review Letters **113**, 235001 (2014).

[48] M. Borghesi, A. Schiavi, D. H. Campbell, M. G. Haines, O. Willi, A. J. MacKinnon, L. A. Gizzi, M. Galimberti, R. J. Clarke, and H. Ruhl, *Proton imaging: a diagnostic for inertial confinement fusion/fast ignitor studies*, Plasma Physics and Controlled Fusion **43**, A267 (2001).

[49] C. J. Zhang, J. F. Hua, Y. Wan, C.-H. Pai, B. Guo, J. Zhang, Y. Ma, F. Li, Y. P. Wu, H.-H. Chu, Y. Q. Gu, X. L. Xu, W. B. Mori, C. Joshi, J. Wang, and W. Lu, *Femtosecond Probing of Plasma Wakefields and Observation of the Plasma Wake Reversal Using a Relativistic Electron Bunch*, Physical Review Letters **119**, 064801 (2017).

[50] A. Maksimchuk, S. Gu, K. Flippo, D. Umstadter, and V. Y. Bychenkov, *Forward Ion acceleration in thin films driven by a high-intensity laser*, Physical Review Letters **84** (2000).

[51] E. L. Clark, K. Krushelnick, J. R. Davies, M. Zepf, F. N. Beg, M. Tatarikis, A. Machacek, P. A. Norreys, M. I. K. Santala, I. Watts, and A. E. Dangor, *Measurment of Energetic Proton Transport through Magnetized Plasma from Intense Laser Interactions with Solids*, Physical Review Letters **84**, 670 (2000).

[52] R. A. Snavely, M. H. Key, S. P. Hatchett, T. E. Cowan, M. Roth, T. W. Phillips, M. A. Stoyer, E. A. Henry, T. C. Sangster, M. S. Singh, S. C. Wilks, A. MacKinnon, A. Offenberger, D. M. Pennington, K. Yasuike, A. B. Langdon, B. F. Lasinski, J. Johnson, M. D. Perry, and E. M. Campbell, *Intense High-Energy Proton Beams from Petawatt-Laser Irradiation of Solids*, Physical Review Letters **85**, 2945 (2000).

[53] S. P. Hatchett, C. G. Brown, T. E. Cowan, E. A. Henry, J. S. Johnson, M. H. Key, J. A. Koch, A. B. Langdon, B. F. Lasinski, R. W. Lee, A. J. Mackinnon, D. M. Pennington,

M. D. Perry, T. W. Phillips, M. Roth, T. C. Sangster, M. S. Singh, R. A. Snavely, M. A. Stoyer, S. C. Wilks, and K. Yasuike, *Electron, photon and ion beams from the relativisit interaction of Petawatt laser pulses with solid targets*, Physics of Plasmas **7** (2000).

[54] F. Wagner, O. Deppert, C. Brabetz, P. Fiala, A. Kleinschmidt, P. Poth, V. A. Schanz, A. Tebartz, B. Zielbauer, M. Roth, T. Stöhlker, and V. Bagnoud, *Maximum Proton Energy above 85 MeV from the Relativistic Interaction of Laser Pulses with Micrometer Thick* CH_2 *Targets*, Physical Review Letters **116**, 205002 (2016).

[55] T. E. Cowan, J. Fuchs, H. Ruhl, A. Kemp, P. Audebert, M. Roth, R. Stephens, I. Barton, A. Blazevic, W. Brambrink, J. Cobble, J. Fernández, J.-C. Gauthier, M. Geissel, M. Hegelich, J. Kaae, S. Karsch, G. P. Le Sage, S. Letzring, M. Manclossi, S. Meyroneinc, A. Newkirk, H. Pépin, and N. Renard-LeGalloudec, *Ultralow Emittance, Multi-MeV proton beams from laser vertual-cathode plasma accelerator*, Physical Review Letters **92**, 204801 (2004).

[56] A. J. Kemp, J. Fuchs, Y. Sentoku, V. Sotnikov, M. Bakeman, P. Antici, and T. E. Cowan, *Emittance grownth mechanisms for laser-accelerated proton beams*, Physical Review E **75**, 056401 (2007).

[57] M. Borghesi, A. J. Mackinnon, D. H. Campbell, D. G. Hicks, S. Kar, P. K. Patel, D. Price, L. Romagnani, A. Schiavi, and O. Willi, *Multi-MeV proton source investigations in Ultraintense laser-foil iteractions*, Physical Review Letters **92**, 055003 (2004).

[58] C. K. Li, F. H. Séguin, J. A. Frenje, J. R. Rygg, R. D. Petrasso, R. P. J. Town, P. A. Amendt, S. P. Hatchett, O. L. Landen, A. J. Mackinnon, P. K. Patel, V. A. Smalyuk, T. C. Sangster, and J. P. Knauer, *Measuring E and B Fields in Laser-Produced Plasmas with Monoenergetic Proton Radiography*, Physical Review Letters **97**, 135003 (2006).

[59] A. B. Zylstra, C. K. Li, H. G. Rinderknecht, F. H. Séguin, R. D. Petrasso, C. Stoeckl, D. D. Meyerhofer, P. Nilson, T. C. Sangster, S. L. Pape, A. Mackinnon, and P. Patel, *Using high-intensity laser-generated energetic protons to radiograph directly driven implosions*, Review of Scientific Instruments **83**, 013511 (2012).

[60] L. Willingale, P. M. Nilson, A. G. R. Thomas, J. Cobble, R. S. Craxton, A. Maksimchuck, P. A. Norreys, T. C. Sangster, R. H. H. Scott, C. Stoeckl, C. Zulick, and K. Krushelnick, *High-Power, Kilojoule Class laser Channeling in Millimeter-Scale Underdense Plasma*, Physical Review Letters **106** (2011).

[61] W. Fox, G. Fiksel, A. Bhattacharjee, P.-Y. Chang, K. Germaschewski, S. X. Hu, and P. M. Nilson, *Filamentation Instability of Counterstreaming Laser-Driven Plasmas*, Physical Review Letters **111**, 225002 (2013).

[62] N. L. Kugland, D. D. Ryutov, P.-Y. Chang, R. P. Drake, G. Fiksel, D. H. Froula, S. H. Glenzer, G. Gregori, M. Grosskopf, M. Koenig, Y. Kuramitsu, C. Kuranz, M. C. Levy, E. Liang, J. Meinecke, F. Miniati, T. Morita, A. Pelka, C. Plechaty, R. Presura,

A. Ravasio, B. A. Remington, B. Reville, J. S. Ross, Y. Sakawa, A. Spitkovsky, H. Takabe, and H.-S. Park, *Self-organized electromagnetic field structures in laser-produced counter-streaming plasma*, Nature Physics **8**, 809–812 (2012).

[63] G. Fiksel, W. Fox, A. Bhattacharjee, D. H. Barnak, P. Y. Chang, K. Germaschewski, S. X. Hu, and P. M. Nilson, *Magnetic Reconnection between Colliding Magnetized Laser-Produced Plasma Plumes*, Physical Review Letters **113**, 105003 (2014).

[64] N. Iwata, K. Mima, Y. Sentoku, A. Yogo, H. Nagatomo, H. Nishimura, and H. Azechi, *Fast ion acceleration in a foil plasma heated by a multi-picosecond high intensity laser*, Physics of Plasmas **24**, 073111 (2017).

[65] J. Kim, A. J. Kemp, S. C. Wilks, D. H. Kalantar, S. Kerr, D. Mariscal, F. N. Beg, C. McGuffey, and T. Ma, *Computational modeling of proton acceleration with multi-picosecond and high energy, kilojoule, lasers*, Physics of Plasmas **25**, 083109 (2018).

[66] D. T. Offermann, K. A. Flippo, J. Cobble, M. J. Schmitt, S. A. Gaillard, T. Bartal, D. V. Rose, D. R. Welch, M. Geissel, and M. Schollmeier, *Characterization and focusiong of light ion beams generated by ultra-intensely irradiated thin foils at the kilojoule scale*, Physics of Plasmas **18**, 056713 (2011).

[67] A. Yogo, K. Mima, N. Iwata, S. Tosaki, A. Morace, Y. Arikawa, S. Fujioka, T. Johzaki, Y. Sentoku, H. Nishimura, A. Sagisaka, K. Matsuo, N. Kamitsukasa, S. Kojima, H. Nagatomo, M. Nakai, H. Shiraga, M. Murakami, S. Tokita, J. Kawanaka, N. Miyanaga, K. Yamonoi, T. Norimatsu, H. Sakagami, S. V. Bulanov, K. Kondo, and H. Azechi, *Boosting Laser-Ion Acceleration with Multi-picosecond pulses*, Scientific Reports **7**, 42451 (2017).

[68] D. Mariscal, T. Ma, S. C. Wilks, A. J. Kemp, G. J. Williams, P. Michel, H. Chen, P. K. Patel, B. A. Remington, M. Bowers, L. Pelz, M. R. Hermann, W. Hsing, D. Martinez, R. Sigurdsson, M. Prantil, A. Conder, J. Lawson, M. Hamamoto, P. Di Nicola, C. Widmayer, D. Homoelle, R. Lowe-Webb, S. Herriot, W. Williams, D. Alessi, D. Kalantar, R. Zacharias, C. Haefner, N. Thompson, T. Zobrist, D. Lord, N. Hash, A. Pak, N. Lemos, M. Tabak, C. McGuffey, J. Kim, F. N. Beg, M. S. Wei, P. Norreys, A. Morace, N. Iwata, Y. Sentoku, D. Neely, G. G. Scott, and K. Flippo, *First demonstration of ARC-accelerated proton beams at the National Ignition Facility*, Physics of Plasmas **26**, 043110 (2019).

[69] B. Albertazzi, S. N. Chen, P. Antici, J. Bker, M. Borghesi, J. Breil, V. Dervieux, J. L. Feugeas, L. Lancia, M. Nakatsutsumi, P. Nicola, L. Romagnagni, R. Shepherd, Y. Sentoku, M. Starodubtsev, M. Swantusch, V. T. Tikhonchuk, O. Willi, E. d'Humires, H. Ppin, and J. Fuchs, *Dynamics and structure of self-generated magnetics fields on solids following high contrast, high intensity laser irradiation*, Physics of Plasmas **22**, 123108 (2015).

[70] P. T. Campbell, D. Canning, A. E. Hussein, K. D. W. Ratnayaka, A. G. R. Thomas, K. Krushelnick, and L. Willingale, *Proton beam emittance growth in multipicosecond laser-solid interactions*, New Journal of Physics **21**, 103021 (2019).

[71] W. L. Kruer, *The Physics of Laser Plasma Interactions*, number 73 in Frontiers in physics, Addison-Wesley Publishing Company, New York (1988).

[72] P. Gibbon, *Short Pulse Laser Interactions with Matter: An Introduction*, Imperial College Press, London (2005).

[73] L. Willingale, *Ion Acceleration from High Intensity Laser Plasma Interactions: Measurements and Applications*, Ph.D. thesis, Imperial College London (2007).

[74] S. C. Wilks and W. L. Kruer, *Absorption of ultrashort, ultra-intense laser light by solids and overdense plasmas*, IEEE Journal of Quantum Electronics **33**, 1954–1968 (1997).

[75] J. E. Crow, P. L. Auer, and J. E. Allen, *The expansion of a plasma into a vacuum*, Journal of Plasma Physics **14**, 6576 (1975).

[76] J. Denavit, *Collisionless plasma expansion into a vacuum*, The Physics of Fluids **22**, 1384–1392 (1979).

[77] S. C. Wilks, A. B. Langdon, T. E. Cowan, M. Roth, M. Singh, S. Hatchett, M. H. Key, D. Pennington, A. MacKinnon, and R. A. Snavely, *Energetic proton generation in ultra-intense lasersolid interactions*, Physics of Plasmas **8**, 542–549 (2001).

[78] P. Mora, *Plasma Expansion into a Vacuum*, Physical Review Letters **90**, 185002 (2003).

[79] J. Fuchs, P. Antici, E. d'Humieres, E. Lefebvre, M. Borghesi, E. Brambrink, C. A. Cecchetti, M. Kaluza, V. Malka, M. Manclossi, S. Meyroneinc, P. Mora, J. Schreiber, T. Toncian, H. Pépin, and P. Audebert, *Laser-driven proton scaling laws and new paths towards energy increase*, Nature Physics **2**, 48–54 (2006).

[80] A. Macchi, M. Borghesi, and M. Passoni, *Ion acceleration by superintense laser-plasma interaction*, Reviews of Modern Physics **85**, 751 (2013).

[81] H. Daido, M. Nishiuchi, and A. S. Pirozhkov, *Review of laser-driven ion sources and their applications*, Reports on Progress in Physics **75**, 056401 (2012).

[82] C. A. J. Palmer, N. P. Dover, I. Pogorelsky, M. Babzien, G. I. Dudnikova, M. Ispiriyan, M. N. Polyanskiy, J. Schreiber, P. Shkolnikov, V. Yakimenko, and Z. Najmudin, *Monoenergetic Proton Beams Accelerated by a Radiation Pressure Driven Shock*, Physical Review Letters **106**, 014801 (2011).

[83] D. Haberberger, S. Tochitsky, F. Fiuza, C. Gong, R. A. Fonseca, L. O. Silva, W. B. Mori, and C. Joshi, *Collisionless shocks in laser-produced plasma generate monoenergetic high-energy proton beams*, Nature Physics **8**, 95 – 99 (2011).

[84] F. Fiuza, A. Stockem, E. Boella, R. A. Fonseca, L. O. Silva, D. Haberberger, S. Tochitsky, C. Gong, W. B. Mori, and C. Joshi, *Laser-Driven Shock Acceleration of Monoenergetic Ion Beams*, Physical Review Letters **109**, 215001 (2012).

[85] L. Biermann and A. Schlüter, *Cosmic Radiation and Cosmic Magnetic Fields. II. Origin of Cosmic Magnetic Fields*, Physical Review **82**, 863–868 (1951).

[86] J. A. Stamper and B. H. Ripin, *Faraday-Rotation Measurements of Megagauss Magnetic Fields in Laser-Produced Plasmas*, Physical Review Letters **34**, 138–141 (1975).

[87] A. Raven, O. Willi, and P. T. Rumsby, *Megagauss Magnetic Field Profiles in Laser-Produced Plasmas*, Physical Review Letters **41**, 554–557 (1978).

[88] C. A. Cecchetti, M. Borghesi, J. Fuchs, G. Schurtz, S. Kar, A. Macchi, L. Romagnani, P. A. Wilson, P. Antici, R. Jung, J. Osterholtz, C. A. Pipahl, O. Willi, A. Schiavi, M. Notley, and D. Neely, *Magnetic field measurements in laser-produced plasmas via proton deflectometry*, Physics of Plasmas **16**, 043102 (2009).

[89] C. P. Ridgers, M. Sherlock, R. G. Evans, A. P. L. Robinson, and R. J. Kingham, *Superluminal sheath-field expansion and fast-electron-beam divergence measurements in laser-solid interactions*, Physical Review E **83**, 036404 (2011).

[90] E. Priest and T. Forbes, *The magnetic nature of solar flares*, The Astronomy and Astrophysics Review **10**, 313–377 (2002).

[91] J. B. Taylor, *Relaxation of Toroidal Plasma and Generation of Reverse Magnetic Fields*, Physical Review Letters **33**, 1139–1141 (1974).

[92] J. B. Taylor, *Relaxation and magnetic reconnection in plasmas*, Reviews of Modern Physics **58**, 741–763 (1986).

[93] P. Sweet, in B. Lehnrt (editor), *Electromagnetic Phenomena in Cosmic Physics*, page 123, Cambridge University Press, London (1958).

[94] E. N. Parker, *Sweet's mechanism for merging magnetic fields in conducting fluids*, Journal of Geophysical Research **62**, 509–520 (1957).

[95] H. E. Petschek, *Magnetic field annihilation*, NASA Special Publication **50**, 425 (1964).

[96] L. Sironi and A. Spitkovsky, *Relativistic reconnection: An efficient source of non-thermal electrons*, The Astrphysiscal Journal Letters **783:L21 (6pp)** (2014).

[97] M. Melzani, R. Walder, D. Folini, C. Winisdoerffer, and J. M. Favre, *Relativistic magnetic reconnection in collisionless ion-electron plasmas explored with particle-in-cell simulations*, Astronomy & Astrophysics **570**, A111 (2014).

[98] A. E. Siegman, *Lasers*, University Science Books, Sausalito, California (1986).

[99] D. Strickland and G. Mourou, *Compression of amplified chirped optical pulses*, Optics Communications **56**, 219 – 221 (1985).

[100] A. Dubietis, G. Jonušauskas, and A. Piskarskas, *Powerful femtosecond pulse generation by chirped and stretched pulse parametric amplification in BBO crystal*, Optics Communications **88**, 437 – 440 (1992).

[101] I. Ross, P. Matousek, M. Towrie, A. Langley, and J. Collier, *The prospects for ultrashort pulse duration and ultrahigh intensity using optical parametric chirped pulse amplifiers*, Optics Communications **144**, 125 – 133 (1997).

[102] G. Cerullo and S. De Silvestri, *Ultrafast optical parametric amplifiers*, Review of Scientific Instruments **74**, 1–18 (2003).

[103] C. Dorrer, A. Consentino, D. Irwin, J. Qiao, and J. D. Zuegel, *OPCPA front end and contrast optimization for the OMEGA EP kilojoule, picosecond laser*, Journal of Optics **17**, 094007 (2015).

[104] L. Waxer, D. Maywar, J. Kelly, T. Kessler, B. Kruschwitz, S. Loucks, R. McCrory, D. Meyerhofer, S. Morse, C. Stoeckl, and J. Zuegel, *High-Energy Petawatt Capability for the Omega Laser*, Opt. Photon. News **16**, 30–36 (2005).

[105] M. Tabak, J. Hammer, M. E. Glinsky, W. L. Kruer, S. C. WIlks, J. Woodworth, E. M. Campbell, and M. D. Perry, *Ignition and high gain with ultrapowerful lasers*, Physics of Plasmas **1**, 1626 (1994).

[106] *About OMEGA EP*, http://www.lle.rochester.edu/omega_facility/omega_ep/index.php.

[107] S. Devic, N. Tomic, and D. Lewis, *Reference radiochromic film dosimetry: Review of technical aspects*, Physica Medica **32**, 541556 (2016).

[108] J. H. Bin, Q. Ji, P. A. Seidl, D. Raftrey, S. Steinke, A. Persaud, K. Nakamura, A. Gonsalves, W. P. Leemans, and T. Schenkel, *Absolute calibration of GafChromic film for very high flux laser driven ion beams*, Review of Scientific Instruments **90**, 053301 (2019).

[109] B. Arjomandy, R. Tailor, A. Anand, N. Sahoo, M. Gillin, K. Prado, and M. Vicic, *Energy dependence and dose response of Gafchromic EBT2 film over a wide range of photon, electron, and proton beam energies*, Medical Physics **37**, 1942–1947 (2010).

[110] S. N. Chen, M. Gauthier, M. Bazalova-Carter, S. Bolanos, S. Glenzer, R. Riquier, G. Revet, P. Antici, A. Morabito, A. Propp, M. Starodubtsev, and J. Fuchs, *Absolute dosimetric characterization of Gafchromic EBT3 and HDV2 films using commercial flat-bed scanners and evaluation of the scanner response function variability*, Review of Scientific Instruments **87**, 073301 (2016).

[111] D. Hey, M. Key, A. Mackinnon, A. MacPhee, P. Patel, R. Freeman, L. Van Woerkom, and C. Castaneda, *Use of GafChromic film to diagnose laser generated proton beams*, Review of Scientific Instruments **79**, 053501 (2008).

[112] R. Weber, J. E. Balmer, and P. Lädrach, *Thomson parabola time-of-flight ion spectrometer*, Review of Scientific Instruments **57**, 1251–1253 (1986).

[113] J. F. Ziegler, www.srim.org.

[114] J. F. Ziegler, M. Ziegler, and J. Biersack, *SRIM The stopping and range of ions in matter (2010)*, Nuclear Instruments and Methods in Physics Research Section B: Beam Interactions with Materials and Atoms **268**, 1818 – 1823 (2010), 19th International Conference on Ion Beam Analysis.

[115] V. Grilj and D. J. Brenner, *LET dependent response of GafChromic films investigated with MeV ion beams*, Physics in Medicine & Biology **63**, 245021 (2018).

[116] M. Schollmeier, M. Geissel, A. B. Sefkow, and K. A. Flippo, *Improved spectral data unfolding for radiochromic film imaging spectroscopy of laser-accelerated proton beams*, Review of Scientific Instruments **85**, 043305 (2014).

[117] M. Zepf, E. L. Clark, K. Krushelnick, F. N. Beg, C. Escoda, A. E. Dangor, M. I. K. Santala, M. Tatarakis, I. F. Watts, P. A. Norreys, R. J. Clarke, J. R. Davies, M. A. Sinclair, R. D. Edwards, T. J. Goldsack, I. Spencer, and K. W. D. Ledingham, *Fast particle generation and energy transport in laser-solid interactions*, Physics of Plasmas **8** (2001).

[118] N. L. Kugland, D. D. Ryutov, C. Plechaty, J. S. Ross, and H.-S. Park, *Invited Article: Relation between electric and magnetic field structures and their proton-beam images*, Review of Scientific Instruments **83**, 101301 (2012).

[119] C. Graziani, P. Tzeferacos, D. Q. Lamb, and C. Li, *Inferring morphology and strength of magnetic fields from proton radiographs*, Review of Scientific Instruments **88**, 123507 (2017).

[120] M. F. Kasim, L. Ceurvorst, N. Ratan, J. Sadler, N. Chen, A. Sävert, R. Trines, R. Bingham, P. N. Burrows, M. C. Kaluza, and P. Norreys, *Quantitative shadowgraphy and proton radiography for large intensity modulations*, Physical Review E **95**, 023306 (2017).

[121] A. F. A. Bott, C. Graziani, P. Tzeferacos, T. G. White, D. Q. Lamb, G. Gregori, and A. A. Schekochihin, *Proton imaging of stochastic magnetic fields*, Journal of Plasma Physics **83**, 905830614 (2017).

[122] J. M. Dawson, *Particle simulation of plasmas*, Reviews of Modern Physics **55**, 403–447 (1983).

[123] R. A. Fonseca, L. O. Silva, F. S. Tsung, V. K. Decyk, W. Lu, C. Ren, W. B. Mori, S. Deng, S. Lee, T. Katsouleas, and J. C. Adam, *OSIRIS: A Three-Dimensional, Fully Relativistic Particle in Cell Code for Modeling Plasma Based Accelerators*, in P. M. A. Sloot, A. G. Hoekstra, C. J. K. Tan, and J. J. Dongarra (editors), *Computational Science — ICCS 2002*, pages 342–351, Springer Berlin Heidelberg, Berlin, Heidelberg (2002).

[124] R. G. Hemker, *Particle-in-cell modeling of plasma-based accelerators in two and three dimensions*, arXiv preprint arXiv:1503.00276 (2015).

[125] A. Davidson, A. Tableman, W. An, F. Tsung, W. Lu, J. Vieira, R. Fonseca, L. Silva, and W. Mori, *Implementation of a hybrid particle code with a PIC description in rz and a gridless description in ϕ into OSIRIS*, Journal of Computational Physics **281**, 1063 – 1077 (2015).

[126] A. J. Mackinnon, P. K. Patel, R. P. Town, M. J. Edwards, T. Phillips, S. C. Lerner, D. W. Prices, D. Hicks, M. H. Key, S. Hatchett, S. C. Wilks, M. Borghesi, L. Romagnani, S. Kar, T. Toncian, G. Pretzler, O. Willi, M. Koenig, E. Martinolli, S. Lepape, A. Benuzzi-Mounaix, P. Audebert, J. C. Gauthier, J. King, R. Snavely, R. R. Freeman, and T. Boehlly, *Proton radiography as an electromagnetic field and density perturbation diagnostic*, Review of Scientific Instruments **83**, 3531 (2004).

[127] M. Roth, T. E. Cowan, M. H. Key, S. P. Hatchett, C. Brown, W. Fountain, J. Johnson, D. M. Pennington, R. A. Snavely, S. C. Wilks, K. Yasuike, H. Ruhl, F. Pegoraro, S. V. Bulanov, E. M. Campbell, M. D. Perry, and H. Powell, *Fast Ignition by Intense Laser-Accelerated Proton Beams*, Physical Review Letters **86**, 436–439 (2001).

[128] S. Bulanov, T. Z. Esirkepov, V. Khoroshkov, A. Kuznetsov, and F. Pegoraro, *Oncological hadrontherapy with laser ion accelerators*, Physics Letters A **299**, 240–247 (2002).

[129] K. Krushelnick, E. Clark, R. Allott, F. Beg, C. Danson, A. Machacek, V. Malka, Z. Najmudin, D. Neely, P. Norreys *et al.*, *Ultrahigh-intensity laser-produced plasmas as a compact heavy ion injection source*, IEEE Transactions on Plasma Science **28**, 1110–1155 (2000).

[130] A. J. Kemp and L. Divol, *Interaction Physics of Multipicosecond Petawatt Laser Pulses with Overdense Plasma*, Physical Review Letters **109**, 195005 (2012).

[131] A. Sorokovikova, A. V. Arefiev, C. McGuffey, B. Qiao, A. P. L. Robinson, M. S. Wei, H. S. McLean, and F. N. Beg, *Generation of Superpondermotive electrons in multipicosecond interactions of kilojoule laser beams with solid-density plasmas*, Physical Review Letters **116**, 155001 (2016).

[132] J. Fuchs, C. A. Cecchetti, M. Borghesi, T. Grismayer, E. d'Humières, P. Antici, S. Atzeni, P. Mora, A. Pipahl, L. Romagnani, A. Schiavi, Y. Sentoku, T. Toncian, P. Audebert, and O. Willi, *Laser-Foil Acceleration of High-Energy Protons in Small-Scale Plasma Gradients*, Physical Review Letters **99**, 015002 (2007).

[133] A. J. Mackinnon, M. Borghesi, S. Hatchett, M. H. Key, P. K. Patel, H. Campbell, A. Schiavi, R. Snavely, S. C. Wilks, and O. Willi, *Effect of Plasma Scale Length on Multi-MeV Proton Production by Intense Laser Pulses*, Physical Review Letters **86**, 1769–1772 (2001).

[134] M. Kaluza, J. Schreiber, M. I. K. Santala, G. D. Tsakiris, K. Eidmann, J. Meyer-ter Vehn, and K. J. Witte, *Influence of the Laser Prepulse on Proton Acceleration in Thin-Foil Experiments*, Physical Review Letters **93**, 045003 (2004).

[135] T. Grismayer and P. Mora, *Influence of a finite initial ion density gradient on plasma expansion into a vacuum*, Physics of Plasmas **13**, 032103 (2006).

[136] A. Flacco, F. Sylla, M. Veltcheva, M. Carrié, R. Nuter, E. Lefebvre, D. Batani, and V. Malka, *Dependence on pulse duration and foil thickness in high-contrast-laser proton acceleration*, Physical Review E **81**, 036405 (2010).

[137] F. Lindau, O. Lundh, A. Persson, P. McKenna, K. Osvay, D. Batani, and C.-G. Wahlström, *Laser-Accelerated Protons with Energy-Dependent Beam Direction*, Physical Review Letters **95**, 175002 (2005).

[138] M. H. Xu, Y. T. Li, X. H. Yuan, Q. Z. Yu, S. J. Wang, W. Zhao, X. L. Wen, G. C. Wang, C. Y. Jiao, Y. L. He, S. G. Zhang, X. X. Wang, W. Z. Huang, Y. Q. Gu, and J. Zhang, *Effects of shock waves on spatial distribution of proton beams in ultrashort laser-foil interactions*, Physics of Plasmas **13**, 104507 (2006).

[139] C. Dorrer, L. J. Waxer, A. Kalb, E. M. Hill, and J. Bromage, *Single-shot high-resolution characterization of optical pulses by spectral phase diversity*, Opt. Express **23**, 33116–33129 (2015).

[140] C. Dorrer, A. Consentino, and D. Irwin, *Direct optical measurement of the on-shot incoherent focal spot and intensity contrast on the OMEGA EP laser*, Applied Physics B **122**, 156 (2016).

[141] S. Göde, C. Rödel, K. Zeil, R. Mishra, M. Gauthier, F.-E. Brack, T. Kluge, M. J. MacDonald, J. Metzkes, L. Obst, M. Rehwald, C. Ruyer, H.-P. Schlenvoigt, W. Schumaker, P. Sommer, T. E. Cowan, U. Schramm, S. Glenzer, and F. Fiuza, *Relativistic Electron Streaming Instabilities Modulate Proton Beams Accelerated in Laser-Plasma Interactions*, Physical Review Letters **118**, 194801 (2017).

[142] G. Scott, C. Brenner, V. Bagnoud, R. Clarke, B. Gonzalez-Izquierdo, J. Green, R. Heathcote, H. Powell, D. Rusby, B. Zielbauer *et al.*, *Diagnosis of Weibel instability evolution in the rear surface density scale lengths of laser solid interactions via proton acceleration*, New Journal of Physics **19**, 043010 (2017).

[143] M. Nakatsutsumi, Y. Sentoku, A. Korzhimanov, S. N. Chen, S. Buffechoux, A. Kon, B. Atherton, P. Audebert, M. Geissel, L. Hurd, M. Kimmel, P. Rambo, M. Schollmeier, J. Schwarz, M. Starodubtsev, L. Gremillet, R. Kodama, and J. Fuchs, *Self-generated surface magnetic fields inhibit laser-driven sheath acceleration of high-energy protons*, Nature Communications **9**, 280 (2018).

[144] S. C. Wilks *et al.*, *Absorption of ultra-intense laser pulses*, Physical Review Letters **69** (1992).

[145] D. Margarone, A. Velyhan, J. Dostal, J. Ullschmied, J. P. Perin, D. Chatain, S. Garcia, P. Bonnay, T. Pisarczyk, R. Dudzak, M. Rosinski, J. Krasa, L. Giuffrida, J. Prokupek, V. Scuderi, J. Psikal, M. Kucharik, M. De Marco, J. Cikhardt, E. Krousky, Z. Kalinowska, T. Chodukowski, G. A. P. Cirrone, and G. Korn, *Proton Acceleration Driven*

by a Nanosecond Laser from a Cryogenic Thin Solid-Hydrogen Ribbon, Physical Review X **6**, 041030 (2016).

[146] J. Krása, D. Klír, K. Řezáč, J. Cikhardt, M. Krůs, A. Velyhan, M. Pfeifer, S. Buryšková, J. Dostál, T. Burian, R. Dudžák, K. Turek, T. Pisarczyk, Z. Kalinowska, T. Chodukowski, and J. Kaufman, *Production of relativistic electrons, MeV deuterons and protons by sub-nanosecond terawatt laser*, Physics of Plasmas **25**, 113112 (2018).

[147] S. Fritzler, Z. Najmudin, V. Malka, K. Krushelnick, C. Marle, B. Walton, M. S. Wei, R. J. Clarke, and A. E. Dangor, *Ion Heating and Thermonuclear Neutron Production from High-Intensity Subpicosecond Laser Pulses Interacting with Underdense Plasmas*, Physical Review Letters **89**, 165004 (2002).

[148] K. L. Lancaster, S. Karsch, H. Habara, F. N. Beg, E. L. Clark, R. Freeman, M. H. Key, J. A. King, R. Kodama, K. Krushelnick, K. W. D. Ledingham, P. McKenna, C. D. Murphy, P. A. Norreys, R. Stephens, C. Steckl, Y. Toyama, M. S. Wei, and M. Zepf, *Characterization of 7Li(p,n)7Be neutron yields from laser produced ion beams for fast neutron radiography*, Physics of Plasmas **11**, 3404–3408 (2004).

[149] M. G. Haines, *Magnetic-field generation in laser fusion and hot-electron transport*, Canadian Journal of Physics **64**, 912–919 (1986).

[150] W. Fox, A. Bhattacharjee, and K. Germaschewski, *Fast Magnetic Reconnection in Laser-Produced Plasma Bubbles*, Physical Review Letters **106**, 215003 (2011).

[151] S. Bulanov, T. Esirkepov, D. Habs, F. Pegoraro, and T. Tajima, *Relativistic laser-matter interaction and relativistic laboratory astrophysics*, The European Physical Journal D **55**, 483 (2009).

[152] Y. L. Ping, J. Y. Zhong, Z. M. Sheng, X. G. Wang, B. Liu, Y. T. Li, X. Q. Yan, X. T. He, J. Zhang, and G. Zhao, *Three-dimensional fast magnetic reconnection driven by relativistic ultraintense femtosecond lasers*, Physical Review E **89**, 031101 (2014).

[153] Y. J. Gu, O. Klimo, D. Kumar, Y. Liu, S. K. Singh, T. Z. Esirkepov, S. V. Bulanov, S. Weber, and G. Korn, *Fast magnetic-field annihilation in the relativistic collisionless regime driven by two ultrashort high-intensity laser pulses*, Physical Review E **93**, 013203 (2016).

[154] L. Yi, B. Shen, A. Pukhov, and T. Fülöp, *Relativistic magnetic reconnection driven by a laser interacting with a micro-scale plasma slab*, Nature Communications **9**, 1601 (2018).

[155] A. Nishiguchi, T. Yabe, M. G. Haines, M. Psimopoulos, and H. Takewaki, *Convective Amplification of Magnetic Fields in Laser-Produced Plasmas by the Nernst Effect*, Physical Review Letters **53**, 262–265 (1984).

[156] S. Fujioka, A. Sunahara, K. Nishihara, N. Ohnishi, T. Johzaki, H. Shiraga, K. Shigemori, M. Nakai, T. Ikegawa, M. Murakami, K. Nagai, T. Norimatsu, H. Azechi, and

T. Yamanaka, *Suppression of the Rayleigh-Taylor Instability due to Self-Radiation in a Multiablation Target*, Physical Review Letters **92**, 195001 (2004).

[157] J. Sanz, R. Betti, V. A. Smalyuk, M. Olazabal-Loume, V. Drean, V. Tikhonchuk, X. Ribeyre, and J. Feugeas, *Radiation hydrodynamic theory of double ablation fronts in direct-drive inertial confinement fusion*, Physics of Plasmas **16**, 082704 (2009).

[158] V. Drean, M. Olazabal-Loum, J. Sanz, and V. T. Tikhonchuk, *Dynamics and stability of radiation-driven double ablation front structures*, Physics of Plasmas **17**, 122701 (2010).

[159] V. A. Smalyuk, R. Betti, J. A. Delettrez, V. Y. Glebov, D. D. Meyerhofer, P. B. Radha, S. P. Regan, T. C. Sangster, J. Sanz, W. Seka, C. Stoeckl, B. Yaakobi, J. A. Frenje, C. K. Li, R. D. Petrasso, and F. H. Séguin, *Implosion Experiments using Glass Ablators for Direct-Drive Inertial Confinement Fusion*, Physical Review Letters **104**, 165002 (2010).

[160] M. Lafon, R. Betti, K. S. Anderson, T. J. B. Collins, R. Epstein, P. W. McKenty, J. F. Myatt, A. Shvydky, and S. Skupsky, *Direct-driveignition designs with mid-Z ablators*, Physics of Plasmas **22**, 032703 (2015).

[161] A. Colaïtis, J.-E. Ducret, M. Le Pennec, X. Ribeyre, and S. Turck-Chiéze, *Towards a novel stellar opacity measurement scheme using stability properties of double ablation front structures*, Physics of Plasmas **25**, 072707 (2018).

[162] G. Chatterjee, P. K. Singh, A. P. L. Robinson, D. Blackman, N. Booth, O. Culfa, R. J. Dance, L. A. Gizzi, R. J. Gray, J. S. Green, P. Koester, G. R. Kumar, L. Labate, A. D. Lad, K. L. Lancaster, J. Pasley, N. C. Woolsey, and P. P. Rajeev, *Micron-scale mapping of megagauss magnetic fields using optical polarimetry to probe hot electron transport in petawatt-class laser-solid interactions*, Scientific Reports **7**, 8347 (2017).

[163] J. P. Chittenden, S. V. Lebedev, C. A. Jennings, S. N. Bland, and A. Ciardi, *X-ray generation mechanisms in three-dimensional simulations of wire array Z-pinches*, Plasma Physics and Controlled Fusion **46**, B457–B476 (2004).

[164] A. Ciardi, S. V. Lebedev, A. Frank, E. G. Blackman, J. P. Chittenden, C. J. Jennings, D. J. Ampleford, S. N. Bland, S. C. Bott, J. Rapley, G. N. Hall, F. A. Suzuki-Vidal, A. Marocchino, T. Lery, and C. Stehle, *The evolution of magnetic tower jets in the laboratory*, Physics of Plasmas **14**, 056501 (2007).

[165] S. Faik, A. Tauschwitz, and I. Iosilevskiy, *The equation of state package FEOS for high energy density matter*, Computer Physics Communications **227**, 117 – 125 (2018).

[166] P. M. Nilson, A. A. Solodov, J. F. Myatt, W. Theobald, P. A. Jaanimagi, L. Gao, C. Stoeckl, R. S. Craxton, J. A. Delettrez, B. Yaakobi, J. D. Zuegel, B. E. Kruschwitz, C. Dorrer, J. H. Kelly, K. U. Akli, P. K. Patel, A. J. Mackinnon, R. Betti, T. C. Sangster, and D. D. Meyerhofer, *Scaling Hot-Electron Generation to High-Power, Kilojoule-Class Laser-Solid Interactions*, Physical Review Letters **105**, 235001 (2010).

[167] J. Fuchs, T. E. Cowan, P. Audebert, H. Ruhl, L. Gremillet, A. Kemp, M. Allen, A. Blazevic, J.-C. Gauthier, M. Geissel, M. Hegelich, S. Karsch, P. Parks, M. Roth, Y. Sentoku, R. Stephens, and E. M. Campbell, *Spatial Uniformity of Laser-Accelerated Ultrahigh-Current MeV Electron Propagation in Metals and Insulators*, Physical Review Letters **91**, 255002 (2003).

[168] P. McKenna, A. P. L. Robinson, D. Neely, M. P. Desjarlais, D. C. Carroll, M. N. Quinn, X. H. Yuan, C. M. Brenner, M. Burza, M. Coury, P. Gallegos, R. J. Gray, K. L. Lancaster, Y. T. Li, X. X. Lin, O. Tresca, and C.-G. Wahlström, *Effect of Lattice Structure on Energetic Electron Transport in Solids Irradiated by Ultraintense Laser Pulses*, Physical Review Letters **106**, 185004 (2011).

[169] L. Gremillet, G. Bonnaud, and F. Amiranoff, *Filamented transport of laser-generated relativistic electrons penetrating a solid target*, Physics of Plasmas **9**, 941–948 (2002).

[170] M. Tatarakis, F. N. Beg, E. L. Clark, A. E. Dangor, R. D. Edwards, R. G. Evans, T. J. Goldsack, K. W. D. Ledingham, P. A. Norreys, M. A. Sinclair, M.-S. Wei, M. Zepf, and K. Krushelnick, *Propagation Instabilities of High-Intensity Laser-Produced Electron Beams*, Physical Review Letters **90**, 175001 (2003).

[171] M. Storm, A. A. Solodov, J. F. Myatt, D. D. Meyerhofer, C. Stoeckl, C. Mileham, R. Betti, P. M. Nilson, T. C. Sangster, W. Theobald, and C. Guo, *High-Current, Relativistic Electron-Beam Transport in Metals and the Role of Magnetic Collimation*, Physical Review Letters **102**, 235004 (2009).

[172] R. J. Dance, N. M. H. Butler, R. J. Gray, D. A. MacLellan, D. R. Rusby, G. G. Scott, B. Zielbauer, V. Bagnoud, H. Xu, A. P. L. Robinson, M. P. Desjarlais, D. Neely, and P. McKenna, *Role of lattice structure and low temperature resistivity in fast-electron-beam filamentation in carbon*, Plasma Physics and Controlled Fusion **58**, 014027 (2015).

[173] S. I. Krasheninnikov, A. V. Kim, B. K. Frolov, and R. Stephens, *Intense electron beam propagation through insulators: Ionization front structure and stability*, Physics of Plasmas **12**, 073105 (2005).

[174] M. Manclossi, J. J. Santos, D. Batani, J. Faure, A. Debayle, V. T. Tikhonchuk, and V. Malka, *Study of Ultraintense Laser-Produced Fast-Electron Propagation and Filamentation in Insulator and Metal Foil Targets by Optical Emission Diagnostics*, Physical Review Letters **96**, 125002 (2006).

[175] M. S. Wei, F. N. Beg, E. L. Clark, A. E. Dangor, R. G. Evans, A. Gopal, K. W. D. Ledingham, P. McKenna, P. A. Norreys, M. Tatarakis, M. Zepf, and K. Krushelnick, *Observations of the filamentation of high-intensity laser-produced electron beams*, Physical Review E **70**, 056412 (2004).

[176] M. N. Quinn, D. C. Carroll, X. H. Yuan, M. Borghesi, R. J. Clarke, R. G. Evans, J. Fuchs, P. Gallegos, L. Lancia, K. Quinn, A. P. L. Robinson, L. Romagnani, G. Sarri, C. Spindloe, P. A. Wilson, D. Neely, and P. McKenna, *On the investigation of fast*

electron beam filamentation in laser-irradiated solid targets using multi-MeV proton emission, Plasma Physics and Controlled Fusion **53**, 124012 (2011).

[177] J. Metzkes, T. Kluge, K. Zeil, M. Bussmann, S. D. Kraft, T. E. Cowan, and U. Schramm, *Experimental observation of transverse modulations in laser-driven proton beams*, New Journal of Physics **16**, 023008 (2014).

[178] L. G. Huang, H.-P. Schlenvoigt, H. Takabe, and T. E. Cowan, *Ionization and reflux dependence of magnetic instability generation and probing inside laser-irradiated solid thin foils*, Physics of Plasmas **24**, 103115 (2017).

[179] M. Santala, M. Zepf, I. Watts, F. N. Beg, E. Clark, M. Tatarakis, K. Krushelnick, A. E. Dangor, T. McCanny, I. Spencer, R. P. Singhal, K. W. D. Ledingham, S. C. Wilks, A. C. Machacek, J. S. Wark, R. Allott, R. J. Clarke, and P. A. Norreys, *Effect of the Plasma Density Scale Length on the Direction of Fast Electrons in Relativistic Laser-Solid Interactions*, Physical Review Letters **84** (2000).

[180] H. Habara, K. Adumi, T. Yabuuchi, T. Nakamura, Z. L. Chen, M. Kashihara, R. Kodama, K. Kondo, G. R. Kumar, L. A. Lei, T. Matsuoka, K. Mima, and K. A. Tanaka, *Surface Acceleration of Fast Electrons with Relativistic Self-Focusing in Preformed Plasma*, Physical Review Letters **97** (2006).

[181] O. Culfa, G. J. Tallents, E. Wagenaars, C. P. Ridgers, R. J. Dance, A. K. R. R. J. Gray, P. McKenna, C. D. R. Brown, S. F. James, D. J. Hoarty, N. Booth, A. P. L. Robinson, K. L. Lancaster, S. A. Pikuz, A. Y. Faenov, T. Kampfer, K. S. Shulze, I. Uschmann, and N. C. Woolsey, *Hot electron production in laser solid interactions with a controlled pre-pulse*, Physics of Plasmas **21** (2014).

[182] A. Pukhov and J. Meyer-ter Vehn, *Relativistic Magnetic Self-Channeling of Light in Near-Critical Plasma: Three-Dimensional Particle-in-Cell Simulation*, Physical Review Letters **76**, 3975–3978 (1996).

[183] K. V. Lezhnin, W. Fox, J. Matteucci, D. B. Schaeffer, A. Bhattacharjee, M. J. Rosenberg, and K. Germaschewski, *Regimes of magnetic reconnection in colliding laser-produced magnetized plasma bubbles*, Physics of Plasmas **25**, 093105 (2018).

[184] J. Matteucci, W. Fox, A. Bhattacharjee, D. B. Schaeffer, C. Moissard, K. Germaschewski, G. Fiksel, and S. X. Hu, *Biermann-Battery-Mediated Magnetic Reconnection in 3D Colliding Plasmas*, Physical Review Letters **121**, 095001 (2018).

[185] A. R. Bell, P. Choi, A. E. Dangor, O. Willi, D. A. Bassett, and C. J. Hooker, *Collisionless shock in a laser-produced ablating plasma*, Physical Review A **38**, 1363–1369 (1988).

[186] P. Brady, T. Ditmire, W. Horton, M. L. Mays, and Y. Zakharov, *Laboratory experiments simulating solar wind driven magnetospheres*, Physics of Plasmas **16**, 043112 (2009).

[187] I. F. Shaikhislamov, V. M. Antonov, Y. P. Zakharov, E. L. Boyarintsev, A. V. Melekhov, V. G. Posukh, and A. G. Ponomarenko, *Laboratory simulation of field aligned currents in an experiment on laser-produced plasma interacting with a magnetic dipole*, Plasma Physics and Controlled Fusion **51**, 105005 (2009).

[188] G. C. Burdiak, S. V. Lebedev, S. N. Bland, T. Clayson, J. Hare, L. Suttle, F. Suzuki-Vidal, D. C. Garcia, J. P. Chittenden, S. Bott-Suzuki, A. Ciardi, A. Frank, and T. S. Lane, *The structure of bow shocks formed by the interaction of pulsed-power driven magnetised plasma flows with conducting obstacles*, Physics of Plasmas **24**, 072713 (2017).

[189] A. Rigby, F. Cruz, B. Albertazzi, R. Bamford, A. R. Bell, J. E. Cross, F. Fraschetti, P. Graham, Y. Hara, P. M. Kozlowski, Y. Kuramitsu, D. Q. Lamb, S. Lebedev, J. R. Marques, F. Miniati, T. Morita, M. Oliver, B. Reville, Y. Sakawa, S. Sarkar, C. Spindloe, R. Trines, P. Tzeferacos, L. O. Silva, R. Bingham, M. Koenig, and G. Gregori, *Electron acceleration by wave turbulence in a magnetized plasma*, Nature Physics **14**, 475–479 (2018).

[190] F. Cruz, E. P. Alves, R. A. Bamford, R. Bingham, R. A. Fonseca, and L. O. Silva, *Formation of collisionless shocks in magnetized plasma interaction with kinetic-scale obstacles*, Physics of Plasmas **24**, 022901 (2017).